# Dielectrophoresis-based Spherical Particle Rotation in 3D Space for Automated High Throughput Enucleation

Prateek Benhal

A thesis submitted for the degree of

Doctor of Philosophy

In

Mechanical engineering

at the

University of Canterbury

Christchurch, New Zealand

30 November 2013

# Acknowledgments

Firstly, I would like to thank Dr. Geoff Chase for the given opportunity to work on this fascinating research and guiding me in hard times. Your constant guidance, leadership, patience and high quality of work always motivate me to be a better researcher, a leader and produce work of a good quality. Your professional direction and genuine care for my best interest have made my days as a postgraduate student both pleasant and productive.

To Dr. Paul Gaynor, I am extremely lucky to have you as part of my supervisory team. Thank you for introducing me to the world of dielectrophoresis, and teaching me ways to manipulate biological entities with non-contact means. I learned a lot from you especially when working my way around in the fabrication lab. Your ideas always fascinated me on producing a new mirco-device to rotate cells. You are always there for question and discussions. Your hard work and tenacity will always stand as a model for me.

To Dr. Björn Oback from AgResearch Ltd., Hamilton, thank you for providing valuable insight into the research and I am obliged to have you as my associate supervisor. I would thank you for the guidance provided by you on bovine oocyte handling. Working in AgResearch for a week with well renowned scientists has increased my curiosity to work with the biologists and biotechnological fields in my near future. I thoroughly enjoyed gaining experience working with you and your amiable team of researchers. Also like to thank, Zach McLean and Anne for the patience to provide bovine oocytes for experiments. Again, thank you all for your expert advice and professional guidance.

I would also like to thank Dr. Wenhui Wang for providing initial supervision on the research. He has provided me valuable lessons to pursue my research career in automation and non-contact manipulation of biological particles. I always enjoyed learning in his company and learnt a lot about basic of research.

I would like to thank Dr. Volker Nock for providing valuable guidance on microfluidics and also for technical guidance in biological applications laboratory. Special thanks to Dr. Martin Allen for providing target material to deposit special transparent metal.

I would like to thank the brilliant and genius people working in the Nanofabrication Laboratory, especially Gary Turner and Helen Devereux for their technical expertise. To Julian Murphy, thank you for your technical guidance and help in fabricating electronic aspects of this research project. Without you all, I would never manage to gain knowledge of nano/micro-fabrication.

I would also like to gratefully acknowledge my lovable country India, for taking good care and nurturing its young scientific talents and professionals all across the globe. Special thanks to MacDiarmid Institute and AgResearch for providing laboratory and material support.

To my officemates: Pavlo Kokhanenko and Natalia Kabaliuk for the friendship, Veronica (for her passion about cookies) and Milad Soltanipour Lazarjan for his funny moments fighting on cookies and friendship.

Finally, to my parents, family and close friends back home, thank you for your unconditional and unwavering support and encouragement. I look forward to seeing you all soon.

# Contents

# Nomenclature

Acronym and abbreviations

| | |
|---|---|
| 3D | Three Dimensions |
| AC | Alternating Current |
| CM | Clausius-Mossotti |
| DC | Direct Current |
| DMF | Dual Mode Fibre |
| DEP | Dielectrophoresis |
| DI | De-Ionised |
| DNA | Deoxyribonucleic Acid |
| FEA | Finite Element Analysis |
| FEM | Finite Element Method |
| ITO | Indium Tin Oxide |
| MII | Metaphase II |
| MEMS | Micro Electro Mechanical System |
| MMT | Magnetically Driven Micro-Tool |
| MW | Maxwell-Wagner |
| nDEP | Negative Dielectrophoresis |
| OAFS | Offset Arc Fusion Spice |
| OCR | Optical Cell Rotator |
| OET | Opto Electronic Tweezers |
| pDep | Positive Dielectrophoresis |
| RF | Radio Frequency |
| EROT | Electrorotation |
| ROT | Rotation |
| RSTD | Relative Standard Deviation |
| SCNT | Somatic Cell Nuclear Transfer |
| SMF | Single Mode Fibre |
| SI | Supplementary Information |

# List of Figures

# List of Tables

# Publications and Presentations

**Conference proceeding:**

- P.Benhal, J.G.Chase, W.H.Wang, P.Gaynor, and B.Oback, *Dielectrophoresis-based 3D cell rotation through integration of bottom and vertical electrodes*, MicroTAS (2013), Frieburg, Germany, October 27-31, MicroTAS-2013 conference proceedings, 2013.
- P.Benhal, J.G.Chase, W.H.Wang, P.Gaynor, and B.Oback, *Rotational electric field simulation on a spherical particle for dielectrophoresis–induced rotation*, 7th International Conference on Microtechnoilogies in medicine and biology conference proceedings, 2013.
- P.Benhal, J.G.Chase, W.H.Wang, P.Gaynor, and B.Oback, *A micro-device integrating vertical and bottom electrodes for 3D cell rotation*, Advanced materials and nano-technology conference (AMN-6) proceedings, Presented poster and paper in Feb 11-15th 2013.
- P.Benhal, J.G.Chase, W.H.Wang, P.Gaynor, and B.Oback, *Harmonic simulation study towards frequency dependent 3D cell rotation for biomedical applications*, ANZ Micro and Nano-fluidics symposium, Wellington, NZ, April 12-13, 2012.
- P.Benhal, J.G.Chase, W.H.Wang, P.Gaynor, and B.Oback, *Cell rotation in Non-uniform AC field by Orthogonal Polynomial Electrodes for enucleation applications*, Student & Postdoc MacDiarmid Symposium, 2011.

**Journal publication:**

- P.Benhal, J.G.Chase, W.H.Wang, P.Gaynor, and B.Oback, *Dielectrophoresis-based 3D cell rotation through integration of bottom and vertical electrodes*, Special issue of journal of Lab Chip, peer reviewed journal article, under print, 2013-2014.

# Preface

This thesis presents analysis and optimization of a novel micro-device or biochip along with experimental validation for the rotation of a spherical partical such as a bovine oocyte in three dimensional (3D) spaces. Biochip is suitable for dielectric particle sorting, characterization and manipulation. Finite element numerical analyses of rotational electric fields are carried out to determine the 3D electric field essential to rotate single oocyte under suspension. Further experimental validations of rotation rate of oocytes are carried out with suitable modelling and results are compared with simulation.

The specific elements of DEP based rotation that this thesis addresses are: optimization of electrodes for generating 3D rotational fields, unique fabrication process of open channel biochip, single oocyte rotation in in-plane (yaw) and out-of-plane (pitch) axes, controlled rotation of oocytes for further enucleation, and determination of dielectric spectrum. These elements have direct and substantial advantage on the recent advancement on applied biotechnology fields such as stem cell research and cloning.

**Chapter 1** reviews the background on necessity of DEP induced particle rotation in bovine cloning. Detailed literature review has been presented along with DEP working principle to manipulate bovine oocyte or a dielectric particle.

**Chapter 2:** develops a model for a rotating particle in an electrokinetic or DEP field. An understanding of previous rotation models is established along with the methodologies. A method is proposed to carry out 3D rotation.

**Chapter 3** presents the biochip design and process involved during fabrication.

**Chapter 4** consists of optimization of electric field within the biochip. Simulations are employed to characterize the biochip device dimensions to generate suitable electric field strength necessary to rotate bovine oocytes. Results are further implemented to obtain rotational fields around in-plane (yaw-axis) and out-of-plane (pitch/roll-axis) rotation.

**Chapter 5** presents experimental setup and methods used during cell rotation experiments. This chapter also discuss limitations in handling and suspending single oocyte in the biochip.

**Chapter 6** presents experimental yaw-axis rotation results of bovine oocytes. Videos of rotating oocytes are presented as a supplementary material.

**Chapter 7** presents experimental pitch-axis rotation results of bovine oocytes. Videos of rotating oocytes are presented as a supplementary material.

**Chapter 8** consists of DEP torque validation by considering the numeric simulation results and experimental results. Validated results are discussed in further detail.

**Chapter 9** consist of experimental results of bovine oocyte rotation in 3D (simultaneous rotation in yaw and pitch) are presented.

**Chapter 10** talks about the conclusions and future work involved.

# Abstract

Cloning by nuclear transfer using mammalian somatic cells has enormous potential application. However, cloning mammalian species through somatic cell nuclear transfer has been simply inefficient in all species in which live clones have been produced, such as 'Dolly' the sheep, and 'Samrupa' the buffalo. Most of the experiments resulted failure, and the success rate ranges from 0.1% to 3%. Developmental defects have been attributed to incomplete reprogramming of the somatic nuclei by the cloning process. Researchers have tried strategies to improve the efficiency of nuclear transfer. However, significant breakthroughs are yet to happen.

The enucleation procedure consisting of extracting reprogrammable genetic material during nuclear transfer has been linked to inefficiencies due to manual error, lack of repeatability and decreased high throughput. Conventional manual enucleation process requires a series of complicated cell rotation in three-dimensional (3D) spaces using a blunt or sharp tipped pipette, and can puncture the cell during genetic material extraction. Current methods frequently damage the cell via physical or chemical contact, and thus have low throughput. Therefore, there is a need for simple, readily automated, non-contact methods for controlled cell rotation.

Precise rotation of the suspended cells is one of the many fundamental manipulations in a wide range of biotechnological applications, such as cell injection and enucleation. Noticeably scarce from the existing rotation techniques is 3D rotation of cells on one single chip. To bridge this gap, this research presents a means of controlled cell rotation for bovine oocytes around both the in-plane (yaw) and out-of-plane (pitch) axes using a simple, low cost biochip fabricated using a mixture of conventional lithography and low-cost micro-milling. It uses a phase varying dielectrophoresis (DEP)-based electrorotation (EROT) biochip platform, which has an open-top sub-millimetre square chamber enclosed by four sidewall electrodes and two bottom electrodes to induce torque to rotate the cells about two axes, thus 3D cell rotation for the first time.

Before fabrication, phase varying DEP-based rotational electric field simulations were carried out in the designed rotation chamber. For this analysis, initial rotational fields are characterised

for both in-plane and out-of-plane axes using multi-physics finite element software. Electrode shape and chamber design were optimised using realistic parameters for the medium and electrode material properties. Results showed remarkable promise to rotate dielectric particles in rotational field strengths of the order of $10^4$ V/m. From simulations, a basic biochip design was optimised.

Within the fabricated biochip, controlled rotations around the in-plane and out-of-plane axes were demonstrated, and the electric field activation frequency range and electrokinetic properties of the bovine oocytes were characterised. Rotation was measured via video image processing with data included on electronic annex. Results show controllable rotation in steps of 5 degrees around both axes with the same chip. In experiments, the maximum rotation rate reached 150°/s in yaw axis and 45-50°/s during pitch axis, while a smooth, stable and controllable rotation rate was found below 30-40°/s. Optimum rotation rates are found for inputs of 10 Vp-p at 500-800 kHz AC frequency for yaw-axis rotation, and 10-20 Vp-p and 10-100 kHz for pitch-axis rotation.

In addition, zona intact and zona free oocytes are shown to have electrical equivalence and found no noticeable difference, generalising the bio-chips capability and results. Further, experimental results were used to validate the numerical solid shell model used in design and it was found that the bovine oocytes are highly polarizable than the surrounding medium. Finally, the dielectric properties of the oocytes were fully characterised enabling further design optimization in future, if desired.

The biochip was successfully designed, optimised and experimentally validated, and successful rotation of bovine oocytes in 3D spaces was demonstrated. These results create a platform tool for biologists to utilise enucleation with high throughput efficiency and ease. In summary, this simple, transparent, low-cost, open-top, and biocompatible biochip platform, allows further function modules to be integrated and is the foundation for more powerful cell manipulation systems.

In brief key novel aspects of the research were:

- Rotation of suspended spherical oocytes in multiple axes (3D rotation) was obtained by AC induced electric fields.
- An open top biochip was successfully fabricated to enable further processing of the rotated cell in 3D spaces.
- Bovine oocyte dielectric spectra were analysed in both in-plane and out-of-plane axes for the first time.
- Bovine oocytes were determined to behave as solid spherical spheres, rather than single spherical shells.

# Chapter 1. Introduction

Precise translation and rotation of biological entities, such as spherical cells, are two fundamental manipulation requirements in applied biotechnological research [1-5]. Unlike translational manipulation, for which a number of methods and devices are available to actuate three-axis displacements, rotation remains extremely challenging when it is required for more than a single axis of cell orientation in 3D spaces. Two typical case applications are cell injection and enucleation, which can be roughly thought of as two reverse manipulations in order [6-10].

As common practice in biology laboratories, cell injection uses a glass micropipette to deposit foreign materials into a desired destination of a cell [11]. In contrast, enucleation uses a glass micropipette to extract Deoxyribonucleic Acid (DNA) materials out of the recipient cell in NT cloning technology [6, 8, 12-15]. For both manipulations to achieve high performance, it is imperative to align the selected injection point or DNA material with respect to the glass micropipette. As the injection point or DNA material of a cell is initially located at an arbitrary orientation, the cell has to be rotated about more than one axis to achieve appropriate alignment.

Manual rotation using the micropipette tip to manipulate the cell is commonly used in laboratory [9, 16]. Because it is performed manually, this method has inherent disadvantages, such as low efficiency, poor precision and inconsistent performance. These disadvantages drive research to leverage a range of physical phenomena and propose corresponding more automated methods for cell rotation, such as electro-kinetics [17, 18], optical tweezers [19] and micro-fluidics [20-22]. In general, the majority of existing methods include electric torque induced by dielectrophoresis (DEP) [23-25] and optoelectronic torque induced by optical means coupled with DEP, such as optical tweezers and ODEP [26], while a few include magnetic torque and mechanical torque. All these methods have been demonstrated to be capable of rotating cells around a single axis (in 2D space) for cell size around 10 μm in diameter. However, controlled rotation of cells around two axes in 3D space in one single device has not been accomplished in a means that also allows the cell to be processed. This goal is the most important issue to be addressed in this thesis.

DEP has been widely attempted for translating and rotating cells [17, 24, 27-30]. Subjected to a non-uniform electric field, any polarizable entity, which includes cells, experiences locally-concentrated induced electric dipoles, which in turn undergo electric forces or torques in the electric field. Collectively, a net DEP force or torque is generated on the cell, leading to translation or rotation respectively. Based on this phenomenon, a classic method was reported to rotate cells in a chamber enclosed by four vertical electrodes, both theoretically and experimentally [29, 31-35]. This early implementation applying external AC potential or direct current (dc) potential alternatively to the vertical electrodes achieved in-plane (yaw) rotation about one single axis, leaving the rotation about multiple axes still a problem. Note that yaw axis rotation is defined as the rotation about Z coordinate and pitch axis rotation is defined as the rotation about X or Y coordinates in 3D spaces.

Recent research has brought a new element into DEP by introducing an optical means to induce DEP, called optical DEP (ODEP) [17, 21, 26]. Compared to conventional DEP, ODEP differs in applying the potential to electrodes by light induced electric field instead of an external potential source. However, the disadvantages of this technique, include three aspects: i) The rotation is still only about a single axis; ii) to induce the rotation, a top electrode is necessary, leading to a closed rotation chamber that forbids external access to the cell inside; and iii) the ODEP technique has not been tried on larger size cells of around 100 μm.

Another similar method is based on optical tweezers, which use the optoelectronic torque generated in the focal point of a light beam to trap and rotate particles [19, 36, 37]. Due to the limited energy of the light, the torque is normally insufficient to rotate cells larger than10 μm diameter, as with ODEP. In contrast, optical tweezers are very suitable for rotating particles of 1-10 μm level. Finally, rotation of particles about more than one axis using optical tweezers has not yet been reported.

Magnetic fields have also been used to rotate cells. Initially, housed in a chamber enclosed by vertically configured electromagnets [38, 39], magnetic beads are solely rotated in-plane. Recently, researchers embedded magnetic nanoparticles into cells, which underwent a magnetic torque in a rotating magnetic field and thus rotated [40] in-plane about the Z-axis, with axis orientation as identified in Fig. 1. However, this method involves inserting magnetic

nanoparticles into cells. As an invasive sample preparation step, it raises the risk of cell damage and may interfere with cell viability and development both of which significantly reduce its usefulness in biological applications. It thus has limited practical application.

Based on the analysis above, a method that solely uses AC electric fields for dual axis rotation is proposed. Relatively higher torques induced by a rotating AC electric field offer advantages compared to ODEP or optical tweezers, allowing rotation of larger cells, such as bovine oocytes used in cloning studies that are typically more than 100 μm in diameter [9]. Accordingly, to realize dual-axis rotation, this biochip differs from existing micro-devices in that it integrates six electrodes are arranged on the bottom substrate and sidewalls, enabling dual-axis rotation controlled by varying applied AC potential amplitude, frequency, and phase shift.

In particular, the in-plane (yaw) rotating electric field is generated by solely activating sidewall electrodes and the vertical out-of-plane (pitch) rotating electric field is generated by activating bottom electrodes and one opposite pair of vertical electrodes. Fabrication of a proof-of-concept biochip and the preliminary experimental data for bovine cell rotation was reported in MicroTAS 2013 [41]. The biochip is transparent, low-cost and open-top, enabling cell rotation in 3D space for applications such as cell injection/enucleation, cancer cell identification, cell dielectric property measurement, and 3D cell imaging. As the applied AC electric field induced DEP-based dipoles are universal in any polarizable material, the biochip could be extended and provides a general solution to rotate entities such as beads, particles, DNA, proteins, and larger organisms.

## 1.1. Background and motivation

Cloning of mammalian species was revolutionised in the 1990's through the successful creation of a cloned sheep, "Dolly", from a single sheep cell [42, 43]. This technique was later applied to other mammals, such as cows, pigs, monkeys and mice [44]. Cloning is currently carried out using a process called nuclear transfer, which involves removal of elements in the nucleus from one recipient cell and subsequently injecting the donor nucleus material into the enucleated recipient cell [15].

Enucleation is the process of extracting the nuclear body of a cell and is a necessary step in many approaches to cloning. A 3D spherical cell needs to be rotated and manipulated precisely to enable enucleation. Currently, the steps involved in cell enucleation are inefficient due to problems of contamination, low repeatability, and damage resulting from complicated manual cell manipulation using skilled manual labour [15, 45-47]. To improve cloning efficiency a lot of research has been done with the end goal of automating cell rotation. Methods include laser ablation [48], optical tweezers [19], fluidic systems [20], magnetic fields [38] and electro-kinetics [33, 49-51].

At present, cell manipulation and rotation techniques are performed using micro-electromechanical (MEMS) systems, which emerged as a technology in the 1980s and integrates mechanical and electrical systems in a micro environment [52]. In the mid-1990s, the field of MEMS evolved to give rise to many disciplines, such as radio frequency (RF) MEMS [53], depending upon the focus of the application [54]. In this line, the field of Bio-MEMS was coined with a focus on biological and bio-chemical applications. Bio-MEMS cover broad range of research including DNA diagnostics [21, 55], protein microarrays [56], micro-fluidics [57] and cell manipulation [58, 59]. All of these applications are enabled by the advantages offered through miniaturization in lab-on-chip devices [38, 60-62].

Lab-on-chip devices have been facilitating the manipulation and rotation of micron level cells with precision [60, 63-66]. Bio-chips using electro-kinetic phenomena, in particular, also provide an efficient means to rotate cells without mechanical contact removing the risk of contact damage, which is common to many manipulation techniques [49, 52]. One such electro-kinetic phenomenon is called DEP-based electrorotation, in which micron scale neutral particles are subjected to electrical forces by applying non-uniform electric fields [34, 49, 52, 64, 67], thus providing a suitable means of non-contact cell manipulation. Even though DEP and electrorotation are well known, precise rotation of spherical objects, such as the cell, remains difficult with this approach despite its other advantages, cresting the basis for this research.

## 1.2. Cloning Background

Cloning is a procedure for producing multiple replicas of genetically identical organisms or cells through nonsexual means [68, 69]. Scientists have experimented with animal cloning, but have been unable to stimulate a specialized (differentiated) cell to produce a new organism directly [69-71]. Instead, they rely on transplanting the genetic information from a specialized cell into an unfertilized egg cell whose genetic information has been destroyed or physically removed [8, 10].

A cell is a neutrally charged particle and it can grow, reproduce, process information, respond to stimuli, and carry out an amazing array of chemical reactions through chromosomes inside the cell nucleus. Cells are broadly classified into eukaryotes and prokaryotes. Mammalian cells are eukaryotic cells, which possess a certain amount of dielectric properties, such as permittivity and conductivities [72-74]. It is these properties that enable electro-kinetic manipulation.

In 1827, German physician Karl von Baer discovered that mammals grow from eggs that come from the mother's ovary [75]. A zygote is created after fertilization of an egg by a sperm cell. These zygotes develop into various distinct type of tissue in the body, after proliferation and differentiation. These tissue cells of different kinds need to be arranged and organized to produce organs and appendages. All these cell types have different kind of asymmetries, a property often called polarity [76], which in turn equips cells with distinct dielectric properties. These properties are exploited by cell manipulation techniques, such as electro-kinetics [33, 51, 67], electro-phoresis [77], and dielectrophoresis [78-80]with the aid of micro-fluidics [21, 22, 40, 59, 61, 81].

The practice of cloning took on new meaning in 1997 with the birth of Dolly the sheep, the world's first mammal cloned from an adult cell by somatic cell nuclear transfer (SCNT) technology. In SCNT, a somatic host cell consisting of genetic material is removed and then inserted into an enucleated egg cell [10]. A typical process of SCNT shown in Figure 1.1 can also be used to create clones for both reproductive and therapeutic purposes.

(a)

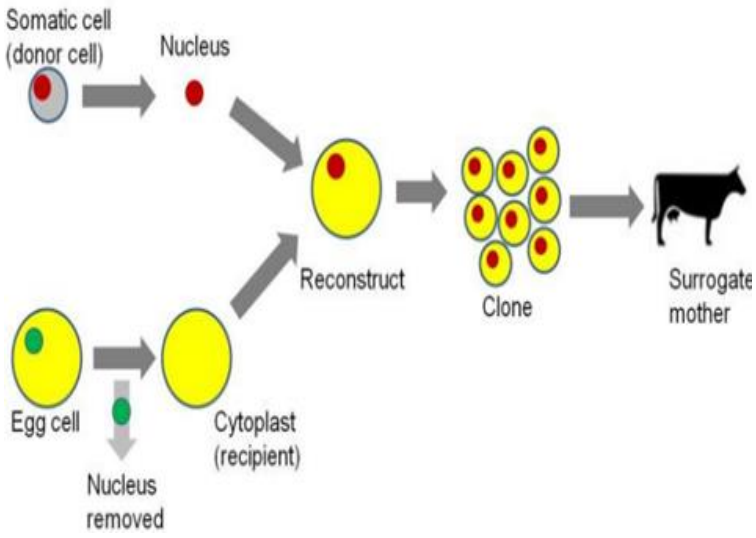


(b)

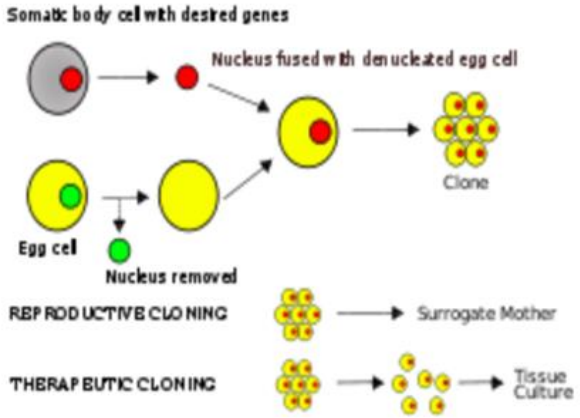


***Figure 1.1:*** *Illustration of cloning. (a) SCNT.*[10] *(b) Application of SCNT* [10].

Cloning steps generally involve *in-vitro* maturation of oocytes, cell enucleation and cell fusion. The oocyte maturation and zona removal steps have already been automated by many researchers [82, 83]. However, the most complex part of automating the cloning process is enucleation. Enucleating a cell is a challenging task and requires extra care for precise cell manipulation. Currently, it is carried out manually in most laboratories through series of manual cell manipulations [9, 10, 68]. Before being enucleated, the cell needs to be rotated. This specific aspect is time consuming and in most cases inefficient due to problems of

contamination and low repeatability. Hence, automating enucleation is the focus of this research. A typical conventional enucleation process is shown in Figure 1.2.

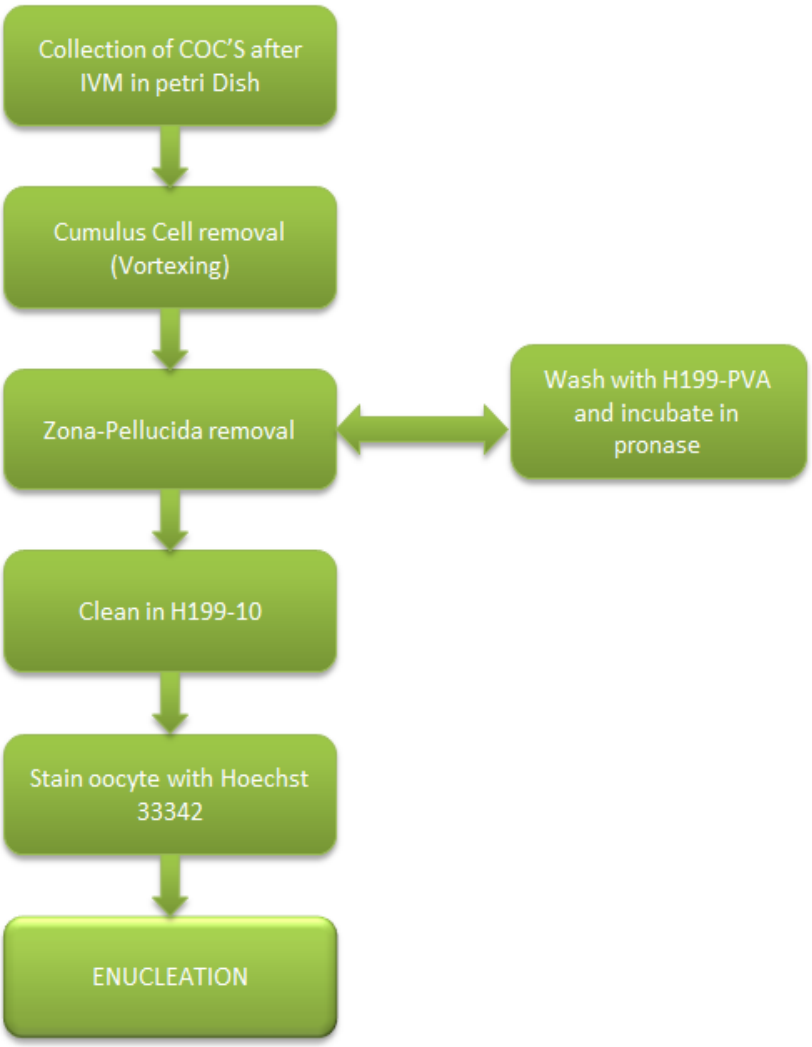


***Figure 1.2:*** *Process of cell enucleation for cloning of bovine species*[9].

Enucleation is generally performed with a blunt aspiration pipette, separation needle, as shown in Figure 1.3. In some cases the pipette is held by a micromanipulator consisting of a hydraulic three-axis joystick to control a blunt aspiration pipette and a separation needle [9, 14, 68, 84]. However, these systems do not affect rotation.

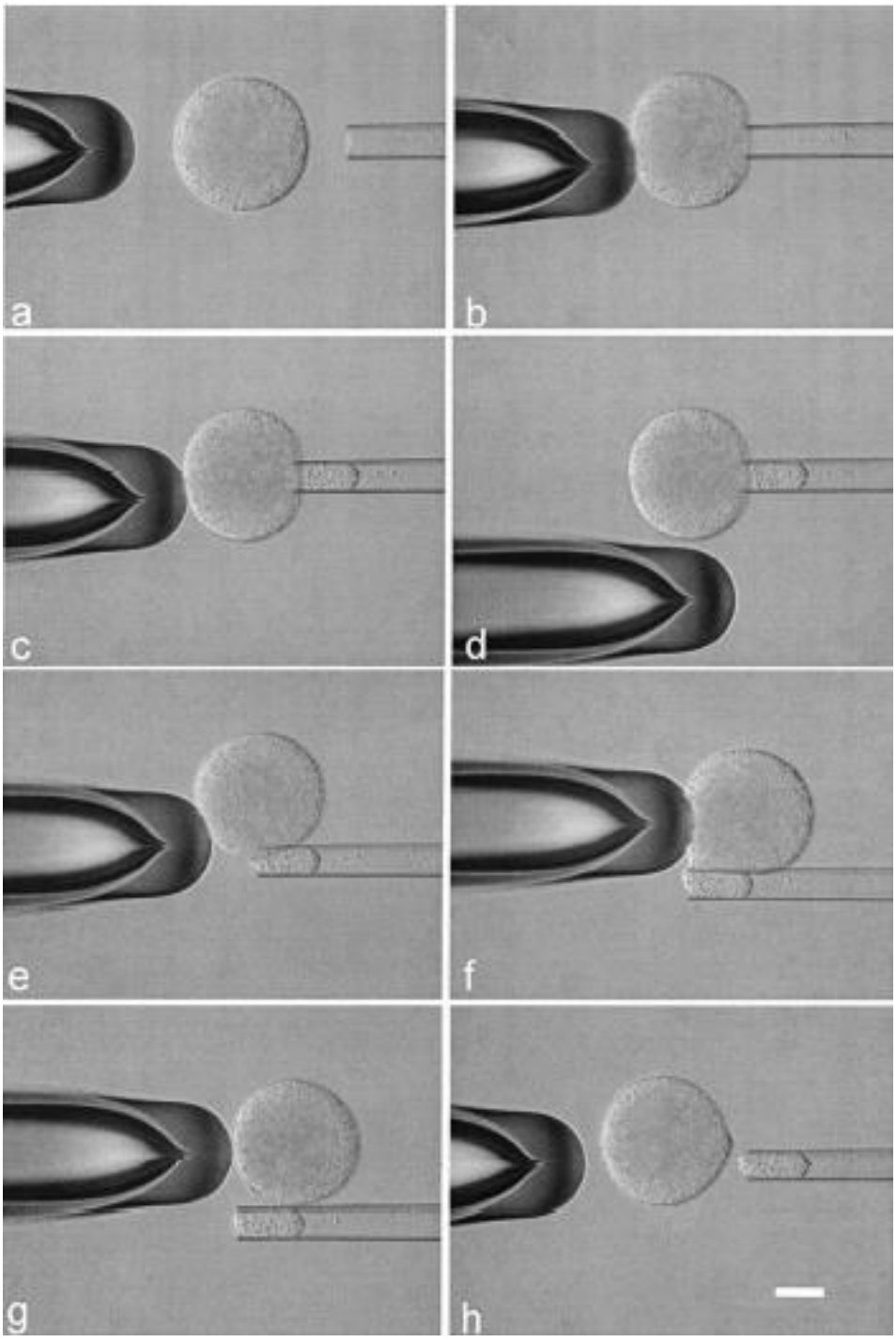


***Figure 1.3:*** *Zona-free enucleation. The metaphase plate is removed using a blunt enucleation pipette (right) and a separation needle (left). (a, b) Under constant UV-exposure (not shown), oocyte is moved until its metaphase plate is adjacent to the enucleation pipette and in the same focal plane, then (c) aspirate the metaphase plate with a small amount of cytoplasm; (d) place the separation needle beside the oocyte, (e) move it straight away from you, (f) and gently rightward (g, h) to pinch of the karyoplasm. The metaphase plate is visible as a clear zone of cytoplasm within the enucleation pipette. Bar = 40 µm* [9, 84].

## 1.3. Enucleation

Enucleation removes the nuclear body from a cell to completely deactivate the recipient genome without compromising viability and reprogramming potential of the cytoplast. The nuclear body consists of DNA molecules, proteins, and histones to form chromosomes. It can be removed during different stages of eukaryotic cell division, but mainly at a young metaphase (MII). At this stage, the chromosomes align inside the polar body, as shown in Figure 1.4, which is easier to extract from the cell. In aged MII oocytes, for example after prolonged *in-vitro* maturation, the polar body gets frequently displaced from its original position, making enucleation more difficult [15, 71, 84, 85].

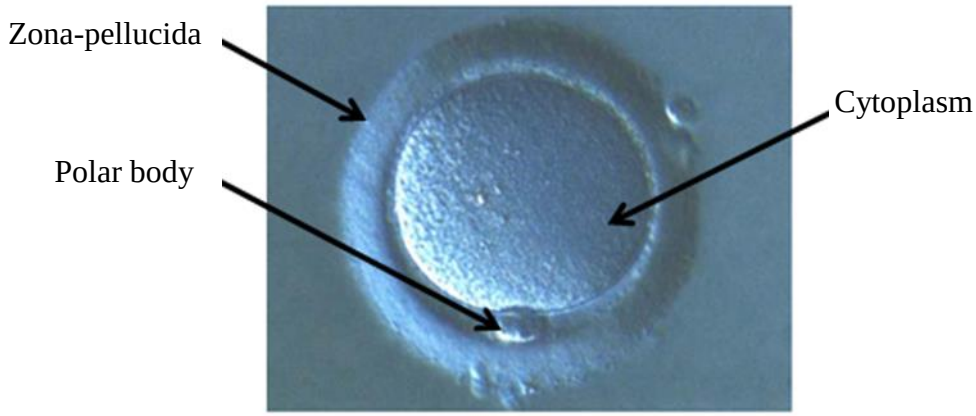


***Figure 1.4:*** *A cell at MII stage with membrane [84].*

Enucleation was originally carried out primarily by two methods. One was lifting the egg pronucleus and surrounding cytoplasm out of the egg pronucleus with a needle [10, 84, 85]. The drawback of this method is the damage of cell through sharp needles and complexity of cell manipulation tasks. The other method was exposing the cell to ultraviolet (UV) irradiation, which deactivates the egg pronucleus, apparently without otherwise damaging the egg [86]. However, in mammals, UV irradiation, alone or in combination with the fluorescent DNA stains, compromises both oocyte membrane and intracellular components [87, 88]. Therefore, it is not currently used for enucleation [13, 89].

There are also other methods including invasive methods and chemically assisted methods [90]. The invasive methods involve bisecting the oocyte into half by needle or fluidic means and discarding those halves containing maternal chromosomes [16, 91]. This approach requires fusion of two cytoplasts to restore the original volume. It thus wastes 50% of the oocyte starting material, resulting in increased mitochondrial heteroplasmy and decreased cloning efficiency.

Figure 1.5, shows the concept of enucleating a swine oocyte by magnetically driven micro tool (MMT) inside a micro-fluidic channel [92]. A two degree of freedom, dual nickel needle arm is fixed with polymer composite legs and is fabricated using photolithography on a permanent magnet fixture. The oocyte is made to flow through a shallow region, where a rigid centre axis of the MMT having the needle bisects the oocyte into half and the enucleated oocyte is later fused with another enucleated oocyte to retain the volume.

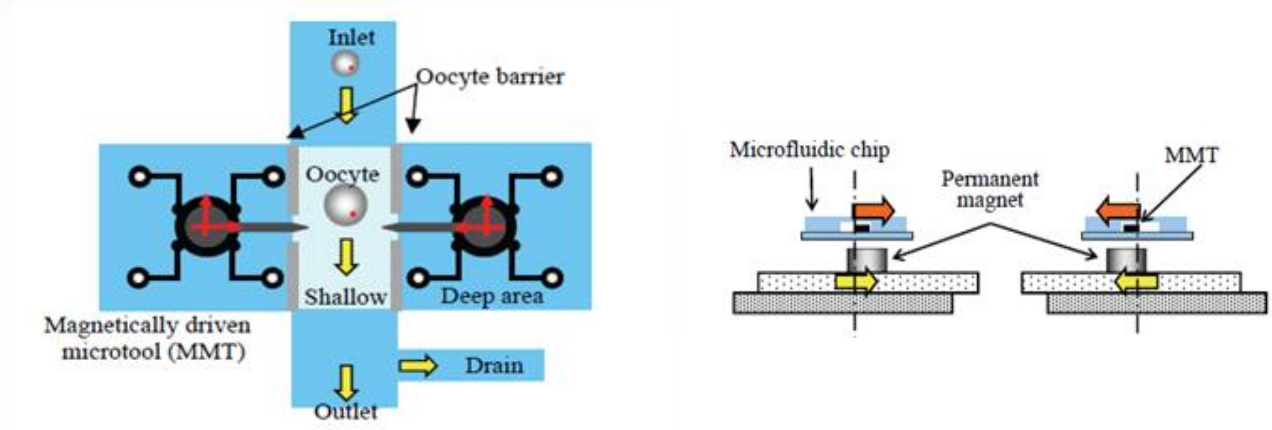


***Figure 1.5:*** *Enucleation by magnetically driven micro tool (MMT). (a).Concept of dual arm micro-robot system on a chip for enucleation of oocyte (Top view. (b). Actuation method of magnetically driven micro tool (MMT) (side view). Position of the permanent magnet is controlled by an XY stage to control magnetic field around the MMT* [92].

One similar alternative and invasive method use high velocity fluid flow generated in the wide micro channel to bisect bovine oocyte (see Figure 1.6) [93]. Due to the high fluid velocity the trapped cell can be bisected with precision in the micro channel. However, the system may be bisecting the oocyte into unbalanced mitochondria or protein into two halves, leading to low cloning efficiency [94, 95].

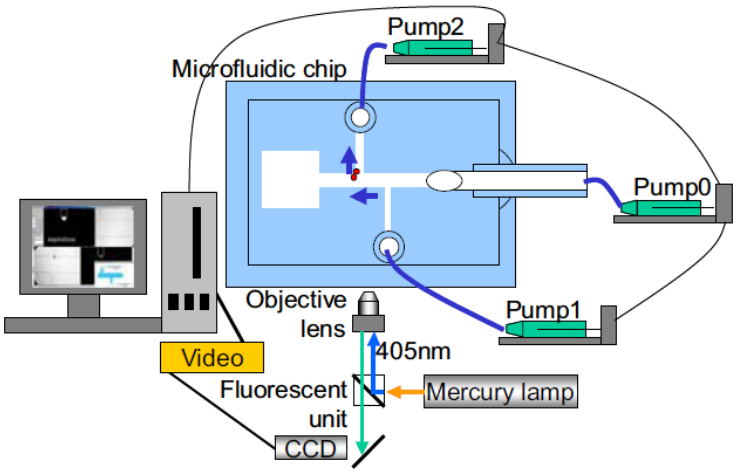


***Figure 1.6:*** *Experimental setup for high velocity fluid type enucleation* [93].

However, it is important to note that manipulation of cells using magnetic and fluidic actuators effectively contacts the cell surface, increasing the chances of cell damage. Chemically-assisted methods expulse the chromosomes off a pseudo-polar body by various combinations of microtubule-depolymerising and oocyte-activating drugs [95-97]. This method has a drawback of cell contamination and harmful chemical effects on cells [6, 12]. Hence, new mechanisms and devices for enucleation must avoid cell contamination and damage.

With automation through micro-manipulation strategies, one can avoid complicated manual cell rotation and manipulation. In recent years, on chip micromanipulation techniques driven by magnetic, electrostatic and fluidic force facilitated automated manipulation attempts [39, 98-100]. The most prevalent micro actuators that can be applied to the micron spaces of the micro channels are optical tweezers, electrostatic micro actuators and magnetic micro actuators [4, 19]. Optical tweezers can manipulate cells indirectly by non-contact actuation of micro tools, thus reducing the risk of damaging the cells [65]. However, the large forces (pN) generated by optical tweezers damage the cells and are not suitable for cell manipulation of the order of 100µm [37, 42, 101]. Electrostatic actuators have the drawback of heat generation [4, 102]. However, magnetic actuators do not damage the cells and have been used in many studies because of their low cost [39, 83, 103].

This research project proposes a DEP based micro-fluidic platform that could perform non-contact cell manipulation tasks automatically and efficiently in shorter time, without the need for highly skilled labour. Electro kinetic phenomena, such as DEP based EROT, can be applied in micro-channels to produce force and torque to control the rate of polar body alignment and the rate of levitation during cell rotation, thus enabling in easy cell manipulation and enucleation.

## 1.4. Dielectrophoresis (DEP) for cell manipulation

DEP is a phenomenon that induces particle movement using a non-uniform electric field. The most unique advantage of dielectrophoresis is that it can be applied to wide array of particle sizes, and types, such as viruses, DNA, cells, and proteins, keeping them viable for further analysis [52, 78]. Equally, it is also a non-contact approach minimizing risk of damage to the cell.

The term dielectrophoresis was first coined by Pohl (1951), who performed important early experiments with small plastic particles suspended in insulating dielectric liquids. That work found that the particles would move in response to applied non-uniform alternating current (AC) or direct current (DC) electric fields [104, 105]. From this work, the basis for the DEP phenomena includes [106-108]:

- A DEP force is experienced by a particle only when the electric field is non-uniform.
- The DEP force does not depend on the polarity of the electric field and can be observed with both AC, and DC, excitation.
- Particles are attracted and repelled to the regions of stronger or weaker electric field depending upon their permittivity with respect to the permittivity of the suspension medium.
- DEP is observed readily for particles with diameters ranging from approximately 1-1000 μm. Above 1000μm, gravity overwhelms DEP forces. Below 1μm, Brownian motion overwhelms the DEP forces.

The DEP term is now often used generally to include quadruple and higher order multi pole dielectric phenomena present in spatially inhomogeneous electric fields [52]. Researchers have studied dielectrophoresis and related electrokinetic effects in detail, and a theoretical understanding of these phenomena is well developed [52, 80, 109]. Finally, DEP has shown broad utility for micro-scale biomedical application [106, 110-112], electro kinetic forces [113-115], and wide array of other areas [3, 24, 116-123]. However, it has not been applied or attempted for precision cell rotation in 3D spaces.

## 1.5. DEP working principle

Polarization is the creation of dipoles or charges inside a neutral particle, when the particle is subjected to an electric field ($E$), as shown in Figure 1.7. In a uniform field, the net charge is zero and the DEP force is zero. Thus, no motion can be induced on the particle. However, if the field is non-uniform, a DEP force is induced on the particle, as shown in Figure 1.8a. alternatively, motion may be induced by rapid angular or linear movement of the electric field relative to the particle, as shown in Figure 1.8.

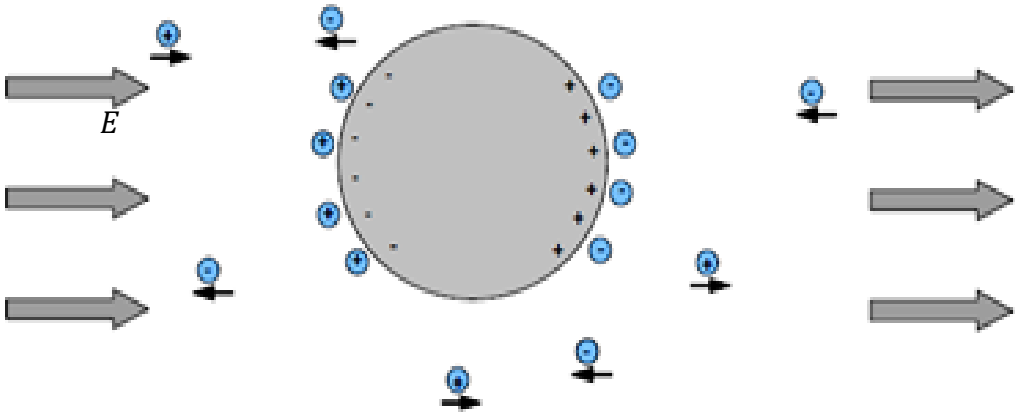


***Figure 1.7:*** *Polarization of a neutral particle [7, 124].*

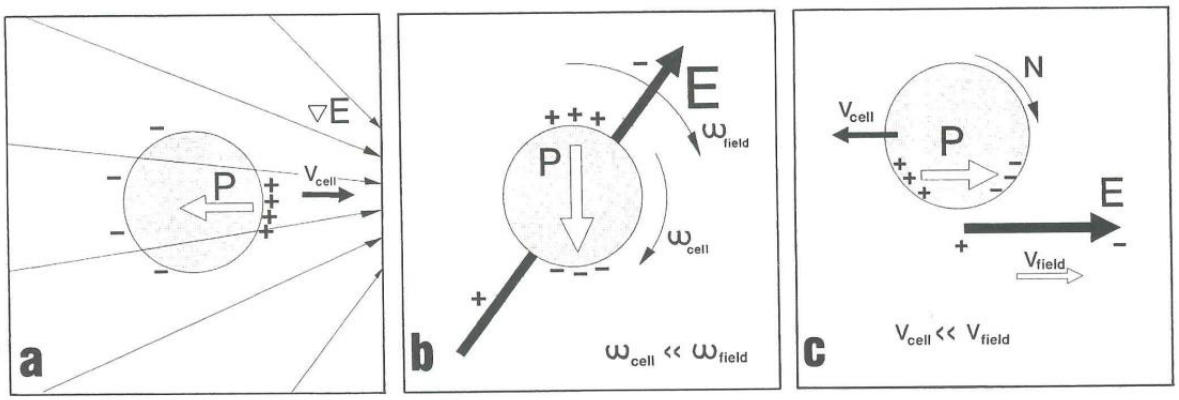


***Figure 1.8:*** *Polarization of particle in varying configuration of electric field (a) particle movement induced by non-uniform field. (b): particle orientation induced by rotational electric field. (c): cell linear movement induced by linear movement of electric field* [7, 124].

The direction of the dipole moment ($p$) induced by the electric field (E) depends upon the polarizability of the particle. In the simple case of two point charges, one with charge + $q$ and the other with charge − $q$, the electric dipole moment $p$ is defined:

$$p = qd \tag{1.1}$$

Where, $d$ is the displacement vector.

If the polarizability of the particle is bigger than that of the surrounding medium, the induced dipole moment in the particle is in the same direction as the electric field. If polarizability of the particle is smaller than that of surrounding medium, the induced dipole moment in the particle would be in the opposite direction of the applied electric field. Thus, direction can be controlled for translating cells [7, 124, 125].

The force acting upon a dipole in a non-uniform electric field can be split into rotational torque ($T$) and translational ($F$) components as defined [126, 127]:

$$F = |u|\,|E|\cos\theta \tag{1.2}$$

$$T = -|u||E|\sin\theta \tag{1.3}$$

Where, $\theta$ is the angle between the dipole direction and that of the electric field, $u$ is the Clausius Mossotti (CM) factor and $E$ is the magnitude of electric field strength in volts per meter.

Force ($F$) is proportional to the gradient of the electric field. Thus, from Equation (1.2), when a dipole is placed between two flat conducting parallel plates, it will experience a zero valued force as $\nabla|E|=0$ for a uniform electric field. If the dipole is oriented at an angle to the electric field, it will rotate until the angle becomes zero.

Equations (1.2) and (1.3) are commonly written in time averaged DEP force and torque, defined:

$$F_{av} = 2\pi R^3 \epsilon \Re[K] \nabla {E_{rms}}^2 \tag{1.4}$$

$$T_{av} = -4\pi R^3 \epsilon_m \Im[K] {E_{rms}}^2 \tag{1.5}$$

Where, $E_{rms}$ is the root mean square of the applied electric field strength, $R$ is the radius of the particle, $\Re[K]$, $\Im[K]$ denote the real and imaginary parts of the quantity contained within the brackets, $\epsilon_m$ is the permittivity of the medium, and K is the CM factor, defined [126, 127]:

$$K = \frac{{\epsilon_p}^* - {\epsilon_m}^*}{{\epsilon_p}^* + 2{\epsilon_m}^*} \tag{1.6}$$

Where, $\epsilon_p{}^*$and $\epsilon_m{}^*$ represent the frequency dependent complex permittivity of the particle and medium, respectively. Detailed theory and the impact of the CM factor are discussed in further detail in Chapter 2.

## 1.6. DEP for cell translation

It is worth noting from Figure 1.9 that the distribution of an electric field can be affected by the electrode geometry. Therefore, the layout of electrode geometry can be used to tune the DEP force obtained, and thus translate particles in a desired fashion. A charged body under uniform electric field experienced net force, but a neutral particle experiences zero net force under uniform electric fields (see Figure 1.9a). If a neutrally charged particle moves away from the region of higher electric field strength, it is termed as negative dielectrophoresis (nDEP) and if the particle moves or translate towards the region of higher electric field strength region, then it is termed as positive dielectrophoresis (pDEP) (see Figure 1.9b). Cell translation has applications in cell characterization, separation, trapping and cell sorting [128, 129]. Figure 1.10-1.12, shows examples of electrode arrays and how they are used to translate cells [127, 128].

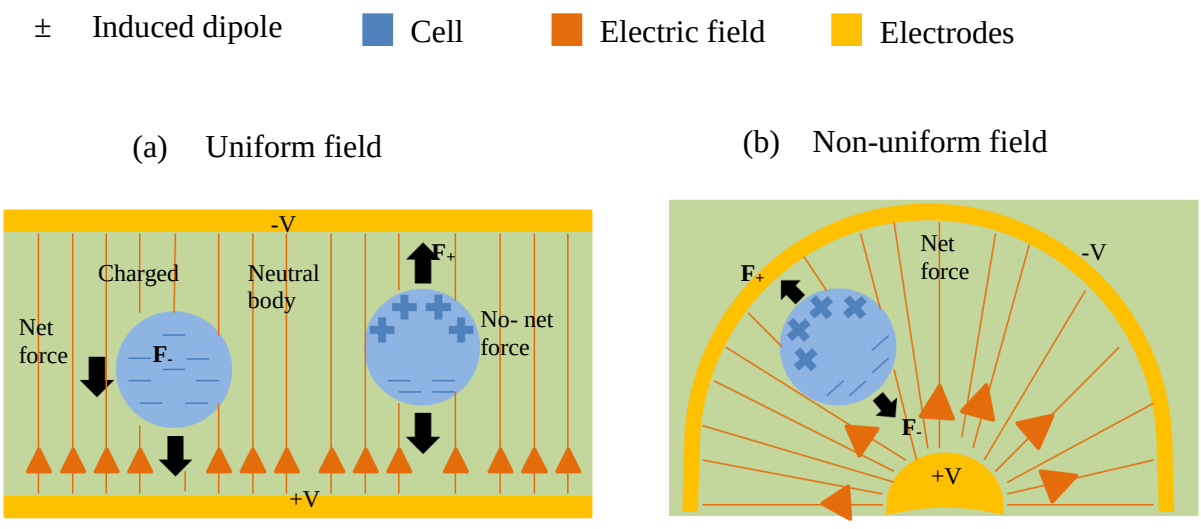


***Figure 1.9:*** *Electric field distribution. (a) Uniform. (b) Non uniform* [127, 128].

Castellated electrode array provides a suitable means to separate healthy cells from unhealthy cells (see Figure 1.10). The healthy cells generally stay away from the region of higher electric

field strength, whereas unhealthy cells generally tend to die of or settle near the region of higher electric field strength. In other words, cells experiencing nDEP collect in the gaps and those experiencing pDEP collect at tips. The castellated system designed by Pethig et al., [130] can only provide cell translation and no rotation.

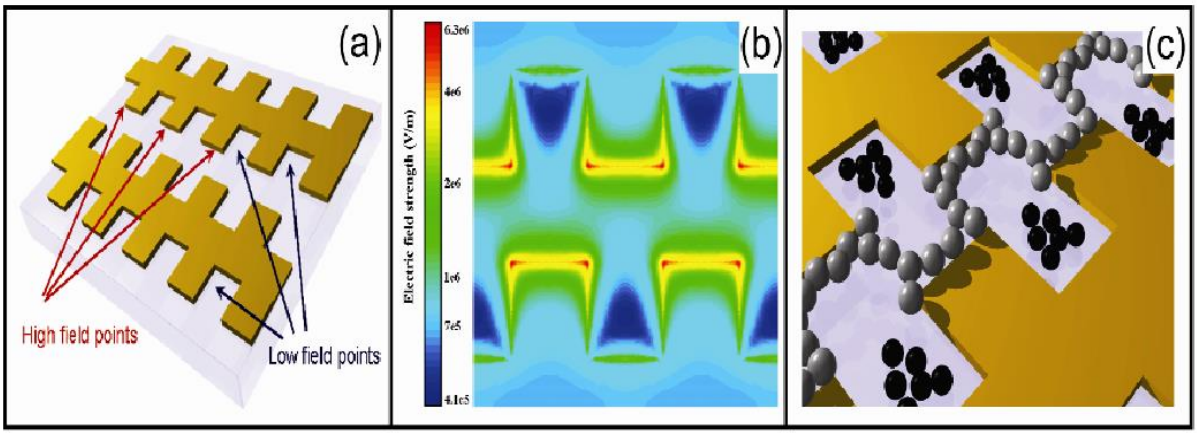


***Figure 1.10:*** *Castellated electrode array for cell transport. (a) Structure. (b) Electric field simulation. (c) Separation mechanism. Note: Typical electrode dimensions are 10-100 µm width and gap. The electric field is maximum at the tips of electrodes and minimum in between the gaps of electrodes. Such electrode arrays have been widely employed to characterize the behaviour of particles. Those cells experiencing nDEP collect in the gaps, and those experiencing pDEP collect at the tips [130].*

Dielectrophoresis based fluid flow fractionation (DEP-FFF) and travelling wave dielectrophoresis (see Figure 1.11-1.12) provides translation movement of cells through suitable laminar fluid inlet flow. Researchers noticed that by placing electrodes on the bottom substrate and applying electric fields with phase shifts, one can translate the cells efficiently. Cell rotation was also seen due to non-uniform field generation. The cell rotation generated is in single axis (pitch axis) and this system cannot control the rotation as flow of fluid will have an effect on cell rotation control. Moreover, the system closed system, making it hard to further process the cells for applications such as injection of drugs and enucleation.

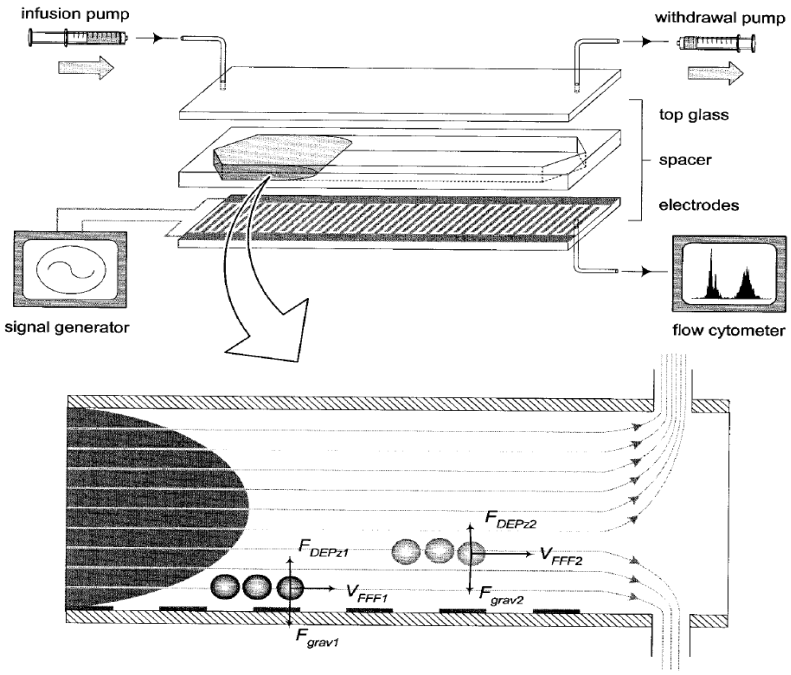


***Figure 1.11:*** *Side view of principle of dielectrophoretic field-flow fractionation (DEP-FFF). DEP force is generated using an array of interdigitated planar electrodes that forms the bottom wall of a flow-through chamber. The electrokinetic force levitates particles of varying polarizability to different equilibrium heights within the chamber. Owing to the parabolic profile of the flowing liquid, particles experience a drag force that depends on their absolute height within the channel and consequently, particles are fractionated along the electrode array* [27].

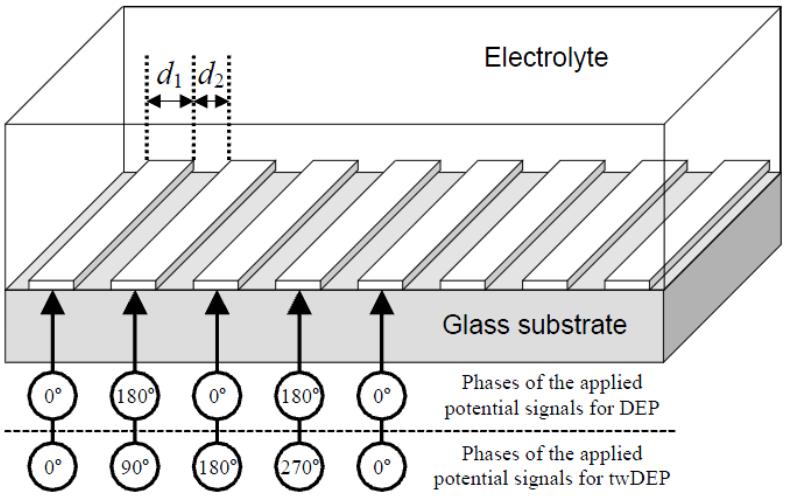


***Figure 1.12:*** *Experimental system for travelling electric fields. Electrodes mounted on glass substrate are subjected to different AC signals and are 90˚-180˚ out of phase. Note: A major difference between FFF and interdigitated electrode array system is the fluid motion which causes the particles to translate in FFF. Whereas in interdigitated electrode system, a travelling wave DEP force causes the particles to move in a stationary liquid electrolyte with phase difference. Due to the phase difference the DEP force also generates particle rotation along with translation* [35].

## 1.7. DEP for cell rotation

During cell rotation, DEP- based EROT torque is generated via the electric field applied between top and bottom electrodes, as shown in Figure 1.13 [131]. The orientation and field analysis concluded that by allocating electrodes in 3D space one can control and analyse the particle rotation [132]. Based on this nDEP, 3D cell handling and levitation has been demonstrated previously, where a single cell is trapped and levitated in the micro-well arrays using nDEP. The cell is processed from the bottom to top ends of the open micro-well channels. However, it is important to note that this approach is not sufficient to obtain controlled rotation of dielectric particle [132, 133]. Because, micro-well array generates nDEP levitation force only in XY-plane (vertical channel), prohibiting rotation control and generation of DEP force in 3D spaces.

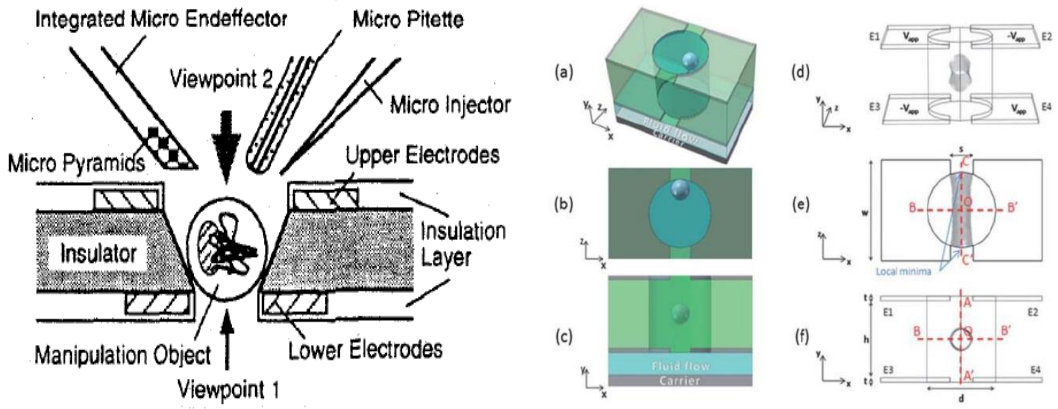


(a) (b)

***Figure 1.13**: 3D cell manipulation. (a). Bio-aligner [23]. (b). nDEP trapping [132].*

Recently, optical trapping, also referred to as optical tweezers, are developed to manipulate particles [134]. In this technique a highly focused laser beam used to trap or rotate micrometre-sized particles depending on the refractive index mismatch to physically hold and move microscopic dielectric objects. Optical tweezers, such as optical cell rotator (OCR), have been used widely in biological, physical, and chemical applications, both as actuators and sensors [36, 135].

In particular, the optical forces are generated as a result of momentum change of optical photons when the optical beam encounters reflection or refraction on an interface, typically the surface of the trapped object. As seen from Figure 1.14-1.15, dielectric objects are attracted to the centre of the beam, slightly above the beam waist by a laser light. The force applied on the object depends linearly on its displacement from the trap centre. However, it has major drawbacks. Optical tweezers develop heat in the cell, which, with force in the order of pN, may damage the cell [36, 136]. Hence, optical tweezers are not of great interest in this application.

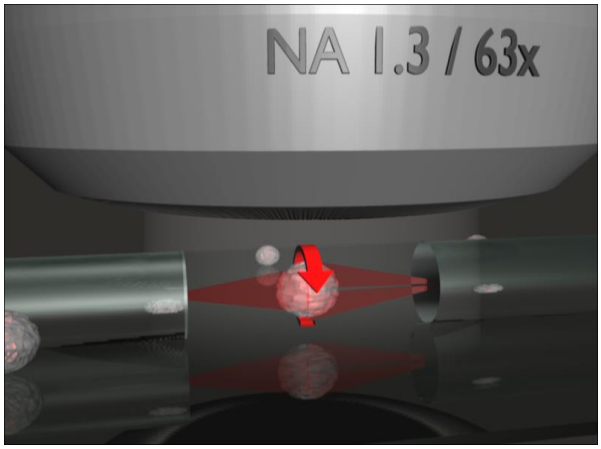


***Figure 1.14:*** *The Optical Cell Rotator (OCR) is a fibre based laser trap that can hold and precisely orient living cells for tomographic microscopy [36].*

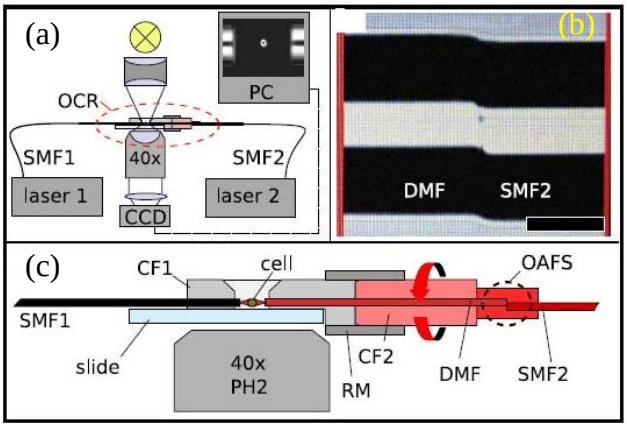


***Figure 1.15:*** *Schematic of the OCR setup. (a) The OCR is mounted on an inverted microscope. SMF, single-mode fibre. (b) Detailed view of the dashed area indicated in (a). SMF1 is mounted in a ceramic ferrule (CF1). SMF2 is spliced with an offset to a dual-mode fibre (DMF), which is mounted in a second ferrule (CF2). Parts shaded in red from one static unit that can be rotated with respect to the rest of the system in a rotation mount (RM). The trapping and rotation of a cell can be imagined through a glass window (slide). (c) Microscopic image of an offset arc fusion splice (OAFS). Scale bar, 50µm [36].*

Researchers have also tried to avoid the disadvantages of optical tweezers, while retaining their flexibility. DEP based tweezers are one result of such attempts, and are described in Figure 1.16 [30]. Other efforts yielded optoelectronic tweezers (OET), based on DEP phenomenon, as shown in Figure 1.16 [137]. In essence, the force is exerted on the cell through optically induced DEP. Even though this method is interesting for its lack of contact, it still lacks the ability to deliver precise rotation control of cells in 3D spaces.

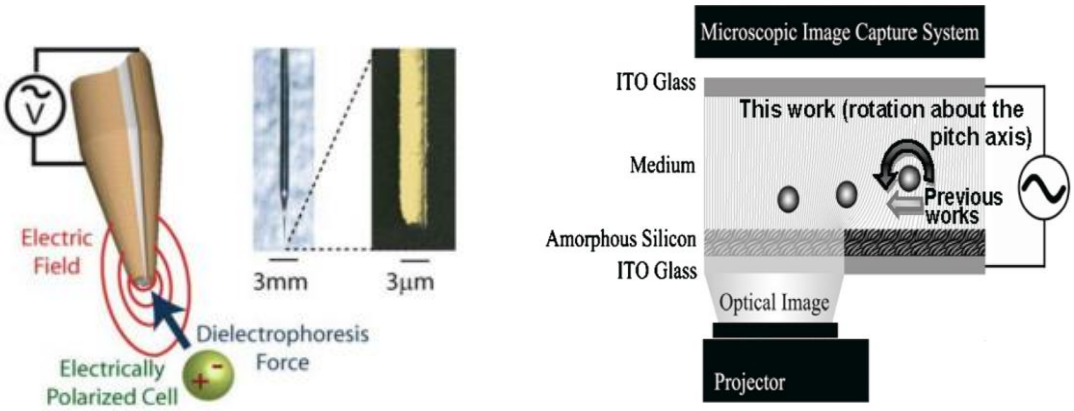


(a) (b)

***Figure 1.16:*** *Cell rotation through optical tweezers. (a) DEP tweezers [30]. (b) Optoelectronic tweezers for cell rotation [137].*

Recently, Wang et al., [52] and Huang et al., [138] presented a nDEP technique to rotate cells using an eight-electrode geometry system (see Figure 1.17-1.18). This system provides easy trapping, levitation of neutrally charged particles in 3D spaces, and are primarily used to analyse the levitated particles for 3D imaging. Even though Wang et al., [52] successfully rotate particles around in-plane and out-of plane axes, the system is closed top. Thus, the fabrication and device design are simple. However, an open-top system is required to enable any further processing of the cell or particle after controlled rotation.

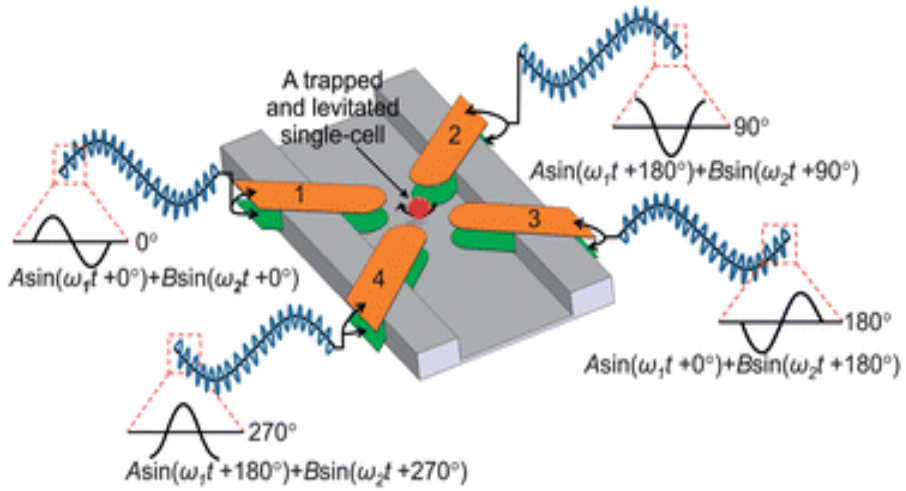


***Figure 1.17***: *Eight-electrode system consisting of two pairs of orthogonally arranged polynomial electrodes on top and two pairs of orthogonally arranged polynomial electrodes on bottom surface. Suitable AC fields are applied to levitate, trap and rotate cells in a single yaw axis through nDEP. This device was mainly used to trap a single suspended particle* [52].

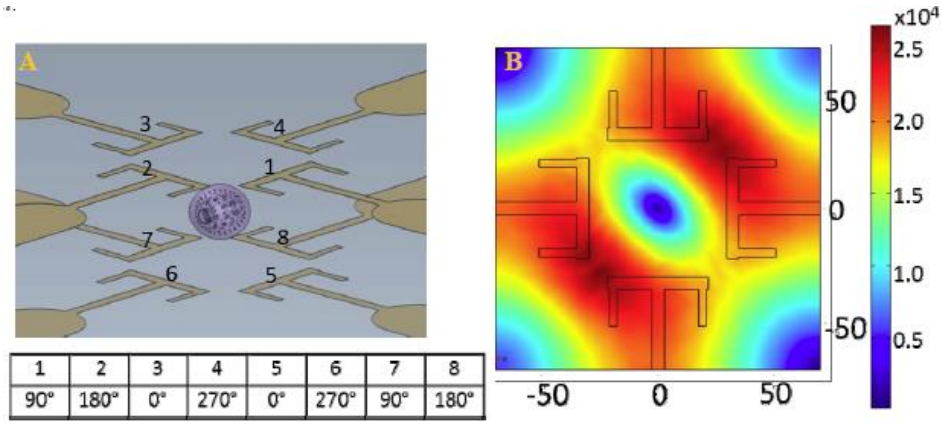


| 1 | 2 | 3 | 4 | 5 | 6 | 7 | 8 |
|---|---|---|---|---|---|---|---|
| 90° | 180° | 0° | 270° | 0° | 270° | 90° | 180° |

***Figure 1.18:*** *Eight-electrode system consisting of two pairs of orthogonally arranged polynomial electrodes on top and two pairs of orthogonally arranged polynomial electrodes on bottom surface. Suitable phase shifted AC fields are applied to levitate, trap and rotate cells in a dual axes through nDEP. This device was mainly used to trap a single suspended particle and rotate particle in 3D spaces, however the system is closed top and is a disadvantage for further processing cells. This system is suitable to analyse cells in 3D spaces, but not suitable for applications such as enucleation* [138].

## 1.8. Problem definition

The cell is a 3D spherical object with neutral charge. Torque needs to be applied to rotate the cell precisely. Research has been carried out to manipulate, levitate and rotate cells in the past.

However, no attempts have been made to precisely orient cells in 3D spaces, in a single micro-device and at low cost. Further, applications such as enucleation and cell injection require a system to be open-top. Hence, a less expensive, open-top but precise and potentially mass scale, cell rotation device is desired to automate the steps and procedures involved in this form of cloning based on enucleation. A DEP based non-contact means of cell manipulation is proposed to best serve this purpose, as DEP polarizes the neutral cell and produces the torque to rotate it without direct contact. Thus, a biochip consisting of an array of electrodes generating dielectric torque to rotate the cells in three dimensions is required and the main goal involves analytical design, analysis, and experimental validation.

## 1.9. Scope and objectives

The vision of this research is to improve the efficiency of manual enucleation by the development of device that could offer high-throughput automation for bovine cloning based on lab-on-chip dielectric cell manipulation. The first objective involves non-contact electro-kinetic manipulation of bovine oocytes on a biochip with greater precise cellular rotation rate control. The second objective is to rotate oocytes in 3D spaces by developing a micro-device concept to rotate oocytes around the yaw and pitch-axis. The final objective is to validate experimental dielectric-spectrum results with a numerical simulation to study oocyte electric characteristics, and thereby produce a suitable micro-device to aid in automation of the enucleation process.

# Chapter 2. DEP Electro-mechanics and modelling

## 2.1. Overview of the system

Polynomial shaped electrodes provide suitable electric fields to rotate cells [139-141]. One such example is shown in Figure 2.1. Polynomial electrode design in two dimensions typically has four electrodes with edges defined by a hyperbolic function in the centre and parallel edges out to an arbitrary distance. Polynomial electrodes are used for trapping and characterizing biological cells using either positive or negative dielectrophoresis [142-144]. Figure 2.1 show the numeric field simulation of the corresponding polynomial electrode.

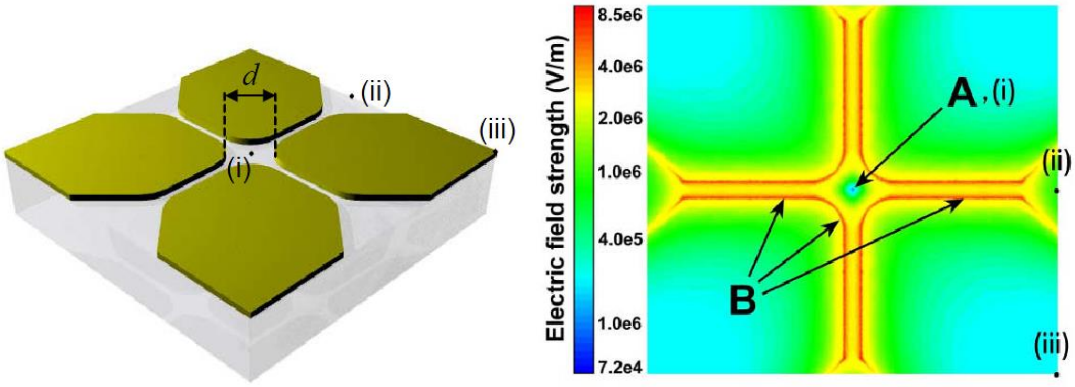


(a) (b)

***Figure 2.1:*** *Cell trapping electrodes. (a). Polynomial electrode design (b). Electric field FEM analysis of electrodes [139].*

The electric field is a function of the electrode dimensions, and for this particular polynomial electrode design, given by [139]:

$$|E| = \frac{4(V_2 - V_1)}{d^2} r \qquad (2.1)$$

Where, $E$ is the electric field, $V_{1,2}$is the electric potential, $d$ is the electrode spacing, and $r$ is the radial distance.

From the analysis of electric field strength also shown in Figure 2.1, the high field strength regions are along the electrode edges (point's labelled B), particularly between adjacent electrodes and around the central region defining the potential minima for positive dielectrophoresis. The symmetry of the design means that there is also a deep potential minimum for negative dielectrophoresis in the centre of the four electrodes that can trap and hold particles (point A) [142-144].

In this research, a similar strategy needs to be employed, where cells can be imported into the micro device using a reservoir, and a DEP force used to move the cells inside the micro channels. DEP also offers the advantage to rotate cells precisely, which cannot be achieved by fluid flow. Fluidic induced rotation on cell require precision instruments such as micro-pumps and injectors, whereas dipole induced DEP-based force and torque directly influence the cell rotation without requiring precision instruments. This general approach was first demonstrated by Morishima et al., [142-145] with DNA molecules, as shown in Figure 2.2 [144].

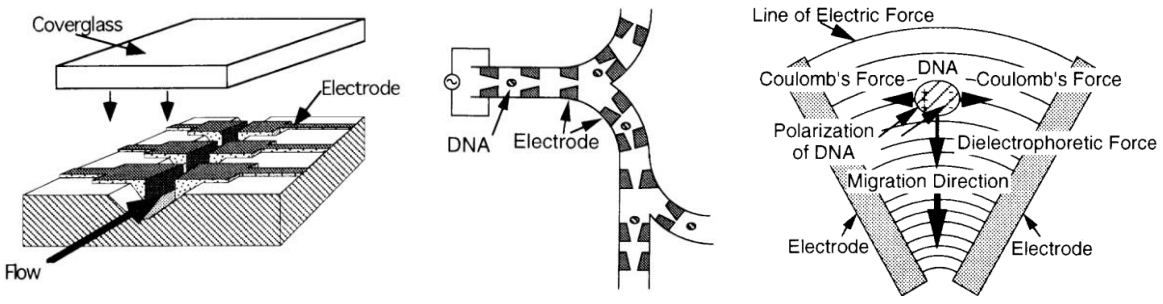


(a) (b) (c)

***Figure 2.2:*** *Transportation and manipulation of cells. (a). micro DNA flow system. (b). Electrode arrangement. (c). Polarization of DNA molecule and dielectric force [144].*

In [144], arrays of electrodes were designed with alternating dielectric currents producing non-uniform electric fields through which a DNA molecule or a cell can be moved. Figure 2.2 shows the forces acting on the molecule and the polarization caused due to the non-uniform electric field generated through the electrode arrangement in a "V" shape with AC voltage. This arrangement has advantages such as: non-invasiveness, selectivity, non-contact, high sensitivity, high speed and durability. This approach is relevant because this type of arrangement can not only trap the particles by optimizing the electric field strength and the torque, but also be used to control the rate of particle rotation in two or three dimensions with a suitable design strategy.

## 2.2. Problem definition

Research over the time [146] has shown that the mechanism responsible for rotation of the cells subjected to electric fields is a relaxation process (Maxwell- Wagner polarization), that retards development of the dipole moment and creates a nonzero torque when electric field rotates . Electrorotation has been used to study the dielectric properties of various bio-particles [147-153], including mammalian cells [154], liposomes [155], parasites and bacteria [147, 156]. Rotation is also valuable in determining cell reaction stimuli, as the measured capacitance and conductance depend on the shape and composition of the membrane and cytoplasm [157]. Overall, the technique has thus also greatly influenced the advancement of automated measurement systems [154, 158].

Even though researchers were successful in configuring EROT phenomenon around one axis, such as yaw [3, 24, 116-123] or pitch [17, 26, 159] rotation, none have tried to rotate dielectrically polarizable particles in 3D spaces using a single micro-device. Non-contact rotation of biological particle around 3D spaces using multiple rotation axes is challenging and requires a wide range of parameters to be optimized. A more detailed understanding of available theory on dielectric EROT is thus required along with a suitable mathematical model to enable design and optimization of such a device.

## 2.3. Theory and methodology

A non-uniform rotational electric field is dependent upon the electrode shape and thus optimization of the electrode shape is required to achieve a desired field to induce motion. An optimization of four electrodes for EROT has been described by Jan. Gisma in 2006 [160]. In most other works [18, 119, 150, 151, 161-163], a rotating field is generated by applying four 90° phase-shifted voltages to four electrodes at right angles to each other. Initially, a 2D parametric simulation model for a basic x-y plane is designed and analysed for different combination of electrodes arrangement. Simulation results are then used to validate experiments in the designed biochip.

### 2.3.1. General equation of electrostatic field and torque (based on dipole moment equations)

In electrostatics, charges are assumed either stationary or to consist of small velocity and accelerations. The force exerted by a stationary point charge $Q_1$ in second stationary point charge $Q_2$ relative to the same origin O, as shown in Figure 2.3, is given by Coulomb's law [164, 165]:

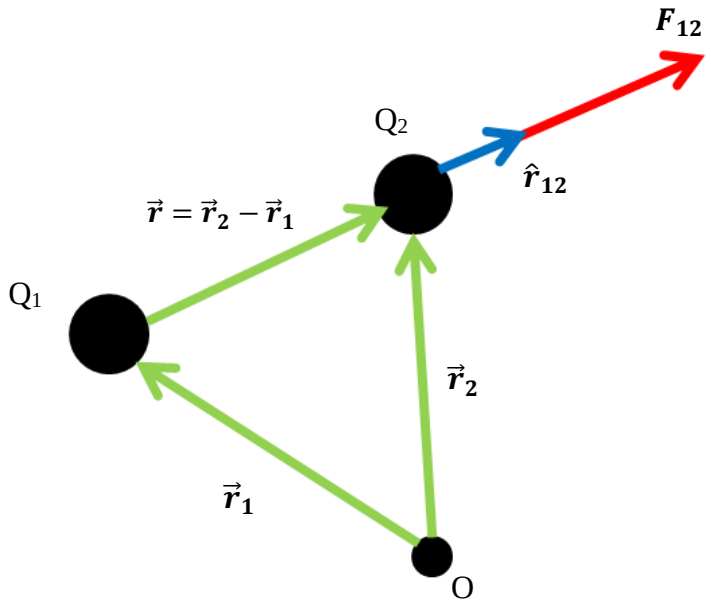


***Figure 2.3:*** *Coulomb's law of two stationary point charges in vacuum experiencing net force.* [165].

$$F_{12} = \frac{Q_1 Q_2}{4\pi\epsilon_0 r^2}\hat{r}_{12} \qquad (2.2)$$

Where r is the separation of the charges and the unit vector $\hat{r}_{12}$ points from $Q_1$ to $Q_2$, $\epsilon_0$ is the permittivity of free space and has the value 8.854×10-12 F/m [166, 167].

Electric field strength from a charge Q is the force per unit charge that produces the Coulomb force on arbitrary unit positive test charge [165, 167], so that:

$$E = \frac{Q}{4\pi\epsilon_0 r^2}\hat{r}_{12} \qquad (2.3)$$

The electric potential is defined to be the scalar $\phi$, such that the electric field is defined [168, 169]:

$$E = -\nabla\phi \qquad (2.4)$$

This electric field is termed as electrokinetic, if it varies with time and frequency. An AC electrical field can thus be defined as a complex function as [168, 169]:

$$E = \Re\left[\tilde{E}e^{i\omega t}\right] \qquad (2.5)$$

This complex AC field leads to atomic, orientation or interfacial polarization on the particle. Over the past few years AC fields have shown promise in manipulating micron scaled biological particles [3, 24, 116-123].

In electrokinetics, electrical fields polarize the particle by generating dipoles on the surface. Non-uniform AC electric fields generate dipole moments causing particle polarizability to

orient in the direction of electric field vectors. If a homogeneous, solid dielectric sphere sits in a homogeneous dielectric medium, charges will accumulate at the interface between the particle and the medium. When an electric field is applied, positive and negative charges are pulled in opposite directions, which gives rise to an effective dipole moment ($p$) across the particle [5, 29, 159, 170]. Hence, the electrokinetic net forces (F) and torque ($T$) on this polarized particle can be calculated from the induced dipole moment, and are defined:

$$F = p \cdot \nabla E \tag{2.6}$$

$$T = p \times E \tag{2.7}$$

The potential of the effective dipole moment $p_{eff}$ can be considered as an increment in the potential distribution of the applied field, with $p_{eff}$ defined:

$$p_{eff} = 4\pi\tilde{\epsilon}_m \left( \frac{{\epsilon_p}^* - {\epsilon_m}^*}{{\epsilon_p}^* + 2{\epsilon_m}^*} \right) R^3 E \tag{2.8}$$

Where ${\epsilon_m}^* and\ {\epsilon_p}^*$ are the complex medium and particle permittivity, respectively, and are functions of AC angular frequency defined:

$${\epsilon_p}^* = \epsilon_p - \mathrm{j}\ (\sigma_p / \omega) \tag{2.9}$$

$${\epsilon_m}^* = \epsilon_m - \mathrm{j}\ (\sigma_m / \omega) \tag{2.10}$$

Where $\sigma_p$ and $\sigma_m$ stand for conductivity of particle and the medium respectively, omega (ω) is the angular frequency of the applied field. Finally,

$$\epsilon_p > 0, \epsilon_m > 0, and -\frac{1}{2} < R[K] < 1$$

Since the $\nabla E^2 = 2E\nabla E$, the DEP force will increase with field strength neglecting cases of zero or constant electric field.

The direction of the force is the same as the sign of K, which depends on the cell polarization with respect to the surrounding medium [31, 106, 171]. The force is zero when the permittivity of the media $\tilde{\epsilon}_m$ and the particle $\tilde{\epsilon}_p$ are equal (K=0). In addition, when $\tilde{\epsilon}_p > \tilde{\epsilon}_m$ the DEP force is positive and directs the particle towards the region of increasing field intensity (positive DEP or pDEP). And, when $\tilde{\epsilon}_p < \tilde{\epsilon}_m$the DEP force is negative and repels the particles to regions of decreasing field intensity (negative DEP or nDEP).

The subscripts $p$ and $m$ thus represent particle and medium, respectively. From Equation 2.8, it is evident that the dipole moment ( $p_{eff}$), is frequency-dependent, where the dependence is characterized by the Clausius-Mossotti (CM) factor $\tilde{f}_{cm}$ [152], defined:

$$\tilde{f}_{cm} = \frac{\tilde{\epsilon}_p - \tilde{\epsilon}_m}{\tilde{\epsilon}_p + 2\tilde{\epsilon}_m} \qquad (2.11)$$

From the induced dipole moments due to the applied electric field, the DEP phenomenon originates as a branch in electrokinetics. In the field, the gradient of the net force on the polarizable particle causes it to translate towards either lower or higher electric field regions, depending upon the particle and the suspended medium properties.

For DEP to originate, two conditions are necessary. One is the difference between polarizability of the particle and the medium to induce a dipole moment. The second is a non-uniform electric field.

If the particle moves towards the region of higher electric field strength positive DEP occurs and if it moves towards lower field strength region then it is termed as negative DEP. It should be noted that DEP force causes the particle translation. Time-averaged DEP force on the dipole is defined:

$$F_{DEP} = \frac{1}{2} V \, \Re[(\tilde{p} \cdot \nabla)\tilde{E}^*] \qquad (2.12)$$

Where $\tilde{p}$ is the induced dipole moment phasor, $V$ is the volume of the particle and $\tilde{E}^*$ is the complex conjugate electric field strength. If the field is non-uniform with no spatially dependent phase, the DEP force simplifies to the form:

$$F_{DEP} = \frac{1}{4} V \, \Re[\tilde{\alpha}] \nabla |\widetilde{E}|^2 \qquad (2.13)$$

Where $\tilde{\alpha}$ is the effective polarizability and if we consider a spherical particle of radius R, Equation (2.13) further simplifies to:

$$F_{DEP} = \pi \epsilon_m R^3 \, \Re\left[\tilde{f}_{cm}\right] \nabla |\widetilde{E}|^2 \qquad (2.14)$$

If phase is spatially varying, then it gives rise to non-zero part of AC electric field. During this time, the dipole sits in a field and the imaginary part of CM is non-zero. The interaction between electric field and this dipole moment leads to a torque on the particle. The finite phase delay between the application of the electric field and the dipole moment results in a change in the direction of the field vector, causing the dipole moment to follow the direction of this field vector. If that applied field vector rotates, then it also rotates the particle giving rise to DEP torque. A DEP torque for the spherical particle is defined:

$$\Gamma_{DEP} = -4\pi\epsilon_m R^3\, Imag\left[\tilde{f}_{cm}\right]|\widetilde{E}|^2 \qquad (2.15)$$

Equation (2.15) shows the frequency-dependent properties of the ROT torque on the non-zero imaginary part of the CM. Moreover, clockwise and anticlockwise rotation of the particle can be obtained by the charge relaxation time constant of the particle [146]. In other words if polarization of the spherical particle is less than that of the medium, the particle rotates in opposite direction to the directional field vector. If particle polarization is more than that of the medium then the particle experiences rotation in the same direction as that of the applied field vector. In a viscous medium, the particle rotates at a constant angular velocity and EROT torque can be measured indirectly by this angular velocity, which is defined [146, 172, 173]:

$$\alpha_{ROT}(\omega) = -\frac{\epsilon_m Imag\left[\tilde{f}_{cm}\right]|\widetilde{E}|^2\xi}{2\eta} \qquad (2.16)$$

Where, $\alpha_{ROT}(\omega)$ is the ROT angular velocity rate and $\xi$ is a scaling factor that is introduced to consider that neither the viscosity, $\eta$ , nor the electric field strength, E, are precisely known [127]. The study of DEP and EROT torque provides vital information about properties of particles in suspension. Moreover, as the particle rotates at constant angular velocity, it is possible to trap, levitate and rotate the suspended particle, which is the key to obtain 3D rotation and control.

Equation (2.16) shows torque dependency upon the ROT electric field strength and CM factor. Terms such as the radius of particle (R) and the permittivity of the medium ($\epsilon_m$) remains constant. Hence, if one can design a micro-device to obtain spatially dependent phase shifted EROT fields, then it is possible to rotate a spherical particle with desired precision.

This approach would avoid the unnecessary cost of rotating cells using optical or fluidic means. The advent of new fabrication methodologies, such as micro-milling, photolithography and

transparent metal electrodes, have also enabled this research and will be described in subsequent chapters.

## 2.4. Limitations and assumptions

Mathematical equations provide a means to numerically calculate the torque or angular velocity of the particle, provided the medium and particle dielectric properties are known. Some of the parameters can be assumed or analysed while designing a device, such as the dielectric constant of the medium and actual electric field strength. Through numerical analysis one can obtain the dielectric spectrum. Numerical results are further required to validate the experiments of rotating cells. Bovine egg cells consist of multiple membranes (zona-intact), or have no membrane (zona-free), making it necessary to analyse both numeric and experimental results.

## 2.5. Proposed design concept

Figure 2.4, shows the basic design concept for the proposed micro-device for 3D electro rotation and the acting torque analysis of the particle. These are further discussed in detail in the following chapters 3 and 4. In comparison to the conventional rotation through DEP, two bottom electrodes are placed and AC signals are switched sequentially to obtain ROT torque simultaneously in yaw, pitch or roll. Since the DEP force and torque are proportional to radius of the particle, it implies that the bigger the radius of particle, the larger the forces acting on it. Moreover, the rotation chamber has to be sized to support the rotation of bigger particles, such as bovine oocytes. In the Chapter 3, the device is designed, analysed and the fabrication methods are detailed.

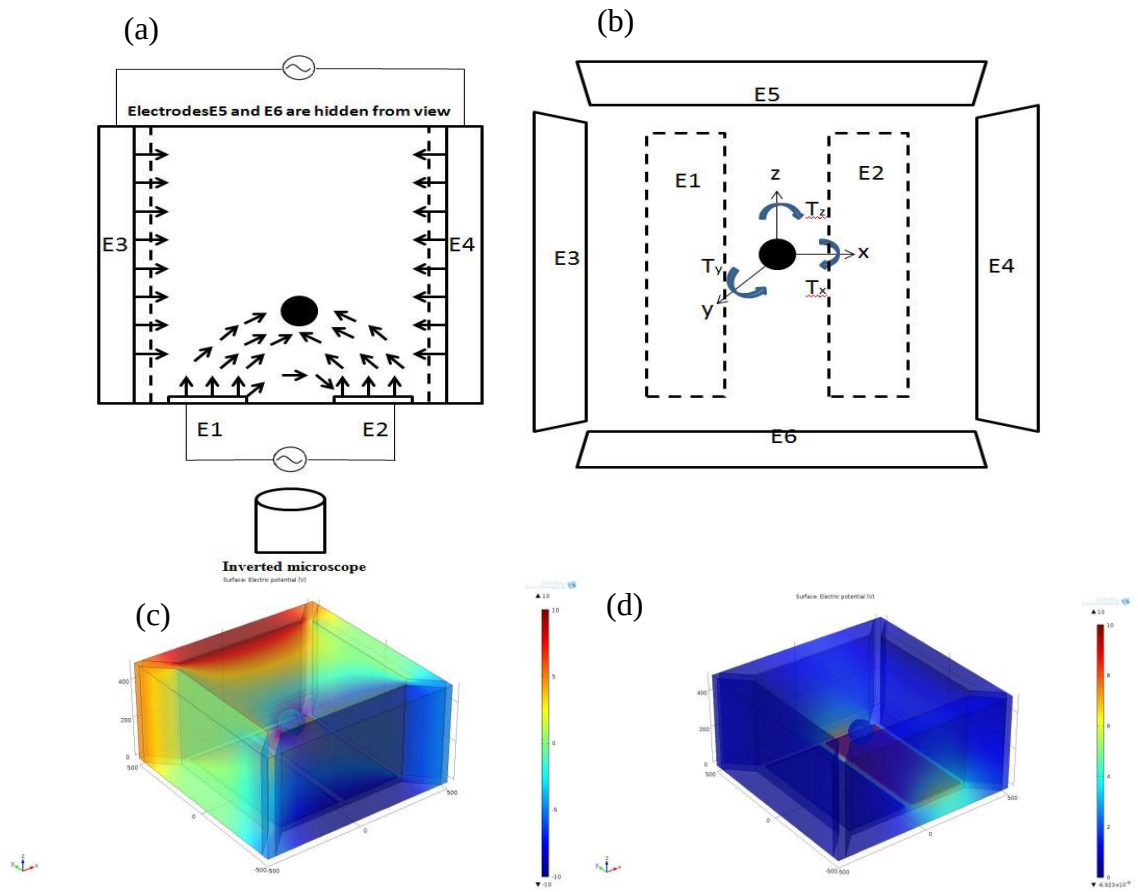


***Figure 2.4:*** *Basic design concept of the device for particle/cell rotation studies (Not to scale). E1 and E2 as bottom ITO electrodes, and E3, E4, E5, and E6 representing vertical side wall electrodes made of brass. (a) Side view of the device. Arrow represents not to scale electric field direction. (b). Rotational torques acting on the particle. (c). 3D model of the device along with electric field simulation, in this case the cell is not inserted to analyse the electric field in the centre region. (c). 3D model of the device along with electric field simulation in yaw-axis. (d). 3D model of the device along with electric field simulation in pitch-axis.*

## 2.6. Summary

In this chapter, the progressive developments in achieving rotation of a dielectric particle using DEP are reviewed and discussed. The theoretical background of DEP and induced EROT is presented to set the stage for explicit design. In particular, DEP-induced cell rotation is dependent on medium and cell dielectric properties along with the electric field strength. The resulting rotation torque is proportional to the size of the particle. A solid shell or solid particle model can be employed to determine numerical rotation torque for a cell with membrane. Bovine oocytes employed in research are zona-free. Hence, they can be considered as a solid model instead of shell.

# Chapter 3. Device design and fabrication

This chapter presents the proposed device design and fabrication process. The fabrication process parameters are characterized and explained. Chapter 4, present the modelling and analysis that has led to these specific device dimensions and design. Finally, a fabricated biochip is shown along with suitable electrical connections.

## 3.1. Device design

The 3D cell rotation device schematic design is shown in Figure 3.1. Positive DEP torque is applied to obtain yaw rotation around the z-axis. In this case, DEP torque is generated by applying AC with a 90° phase shift on the four sidewall vertical electrodes. In addition, the two bottom electrodes, together with the sidewall electrodes, are used to induce pitch-axis rotation either around the x or y-axis. Activation of indium tin oxide (ITO), in particular, enables this pitch axis rotation, but within this single chip design [41].

Hence, the novelty lies in sharing the sidewall electrodes for bovine oocyte rotation around multiple axes, which leave an open top to the biochip and providing access for the micropipette. This last aspect provides a favourable benefit for any subsequent cell manipulations that might be needed. Although chip design for rotation of cells or biological entities is well known, this design is a very simple and cost effective micro-device compared to devices fabricated using conventional photolithography methods. It also offers a single chip for full 3D cell rotation and orientation.

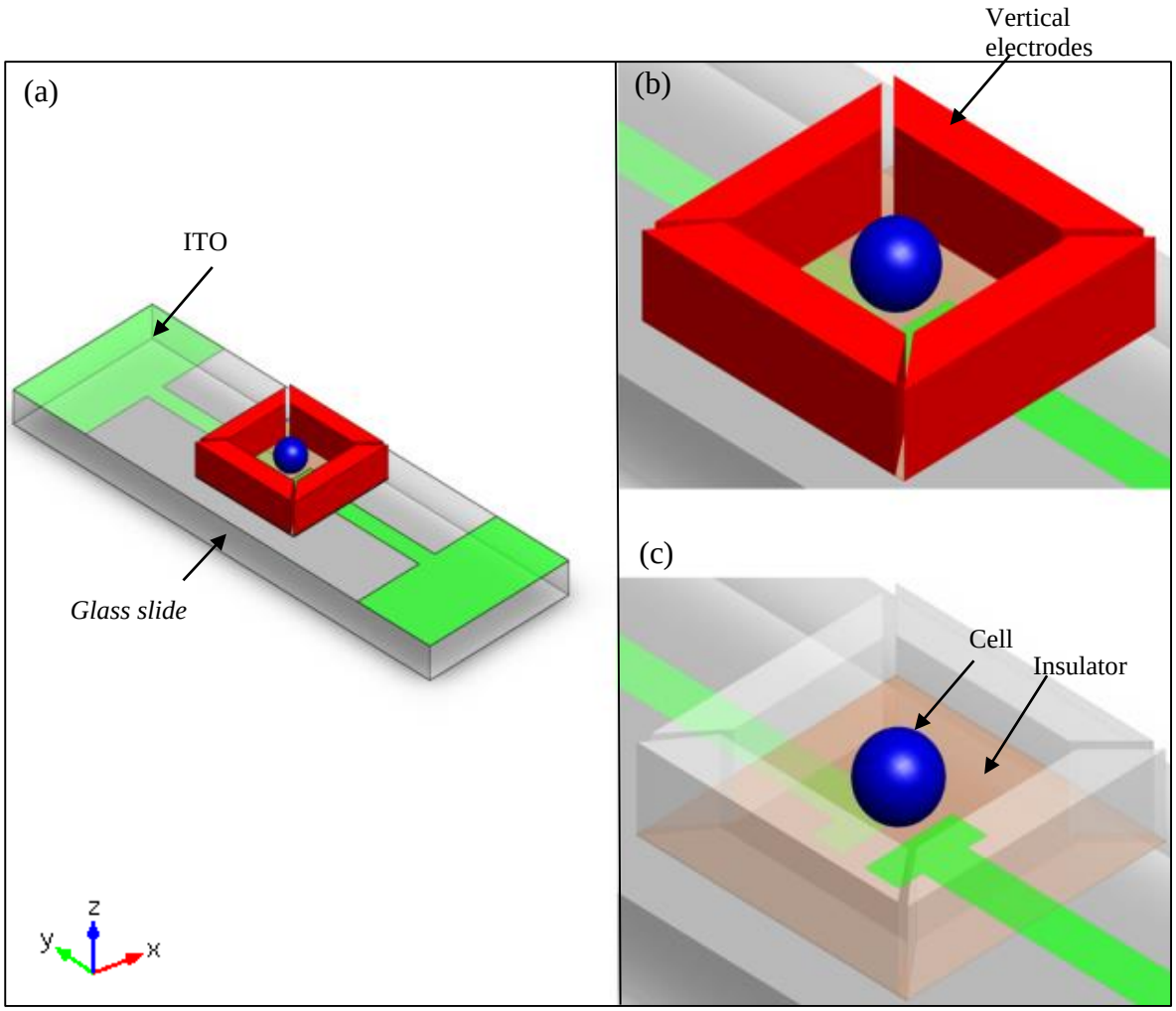


***Figure 3.1:*** *DEP biochip platform design. (a) Overview of the biochip. (b) Four isolated vertical electrodes of height 500 µm forming a chamber with a cell inside. (c) Two bottom ITO electrodes underneath the chamber, separated by a 30-µm gap. Vertical electrodes are set transparent for better visualization effect. Note vertical electrodes are isolated from the bottom ones via an insulator layer (ZnO). Dimensions not to scale.*[41]

## 3.2. Device fabrication

The device is fabricated through the fusion of photolithography for the bottom ITO electrodes and micro-milling for the vertical electrodes. Micro-electrode structures were fabricated on borosilicate glass. In contrast, vertical electrodes are micro-milled instead of electroplating. The vertical micro-milled electrodes are later aligned on top of the bottom ITO electrodes. A small hole is drilled to channel particles into central chamber rotation chamber. The following sections present the detailed fabrication steps and procedures involved during photolithography and micro-milling.

### 3.2.1. Photolithography

Bottom ITO electrodes are fabricated on glass substrate using micro-fabrication technology such as photolithography. Photolithography is the process used to transfer a certain pattern using light from a photomask to a light-sensitive material/chemical, which is often referred to as photoresist [174, 175]. When exposed to UV light, the resist material is modified according to the resist category. There are two types of photoresist, namely positive and negative resist. In the case of negative photoresist, the pattern area which is exposed to radiation UV light will remain after the photoresist developer, while in the case of positive photoresist, the regions hit by the light dissolve after development meanwhile the unexposed region will remain intact.

A positive photoresist (AZ4562, MicroChem, Newton, MA) is used to pattern the transparent ITO electrodes in this research. The resist is medium-viscous of the order 440 cSt at 25° C. The photoresist is capable of producing medium to high aspect-ratio structures. Photoresist further enables film thicknesses of 5.0-8.8 µm depending on the mode of operation. The AZ4562 is spin coated onto glass with a thickness of 8 to 10 micron at a spin speed of 2000 rpm (acceleration 800 rpm/s) for 30 seconds using a spinner (Laurell WS-400B-6NPP/LITE). The coated borosilicate glass slide is then heated on a hotplate at 100˚ C for 50 seconds for prebake. Next, this glass slide with photoresist is exposed to ultra violate (UV) light through the required electrode pattern from a photo mask for 30 seconds in a Sues MA6 (Karl S*ü*ss GmbH, Germany) mask aligner. The exposure dose is defined as the product of light intensity and exposure time defined:

$$\textit{Exposure Dose (mJ/cm2)} = \textit{Exposure time (s)} \times \textit{Intensity (mW/cm2)} \qquad (3.1)$$

This equation is based on the AZ4562 datasheets [176, 177]. The exposure energy dose of 170-180 mJ/cm2 is administered for the thickness of 25-30 µm. Since the light intensity of the mask aligner lamp was measured to be 5.9 mW/cm2. The exposure time estimated from Equation (3.1) is 30 sec.

The mask design is shown in Figure 3.2 for this device. It was created the visualized design using L-edit software (Tanner Tools, USA). As the final stage, the photoresist is developed using MIF351B developer for 10 seconds. Finally the substrates containing patterned photoresist were sputtered with ITO metal in radio frequency (RF) sputterer.

Sputtering of ITO is performed in a magnetron sputtered system (MRC-603) equipped with a load-lock A 5× 15 $in^2$ ITO target (10wt% Sn2) was used for the deposition. The base pressure of the vacuum system was 3.5 × $10^{-6}$ $mbar$. ITO sputtering was done in an argon and oxygen (Ar-$O_2$) gas mixture at pressure of 3 × $10^{-3}$ $mbar$ with a RF power density varying from 1.2 W/cm2 to 3.0 W/cm2. The sputtering time for the optimized process was about 60 minutes for 300 nm thick ITO layers deposition [178, 179]. Figure 3.3, shows the sputtered ITO along with photoresist on glass substrate.

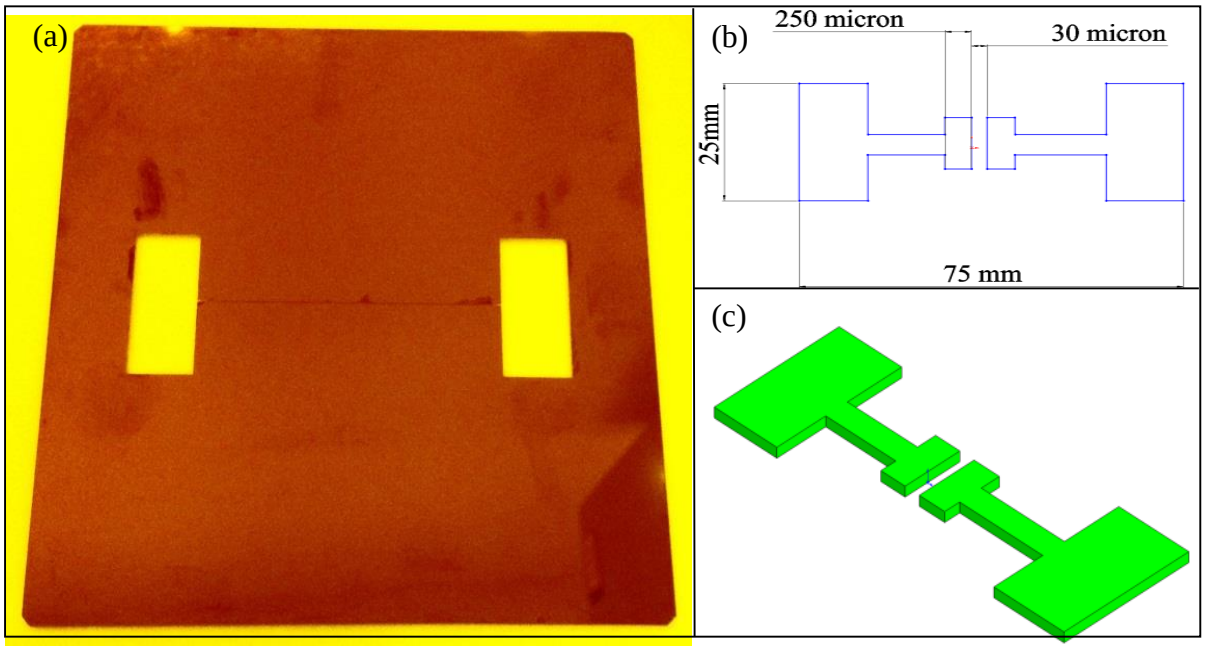


***Figure 3.2:*** *Mask design (a). Fabricated mask (b). Dimensions of ITO pattern (c). 3D isometric view of the electrodes to be fabricated on glass substrate. (Not to scale).*

After these steps, a lift off process is employed to strip off unwanted photoresist from the glass substrate. Lift off is carried out by placing the substrate in acetone bath for 15-20 seconds, and carefully the unwanted materials are lifted off. Finally, the substrate dried with nitrogen gun and is further rinsed with DI water and again dried. Figure 3.3b, shows the fabricated ITO on top of glass substrate.

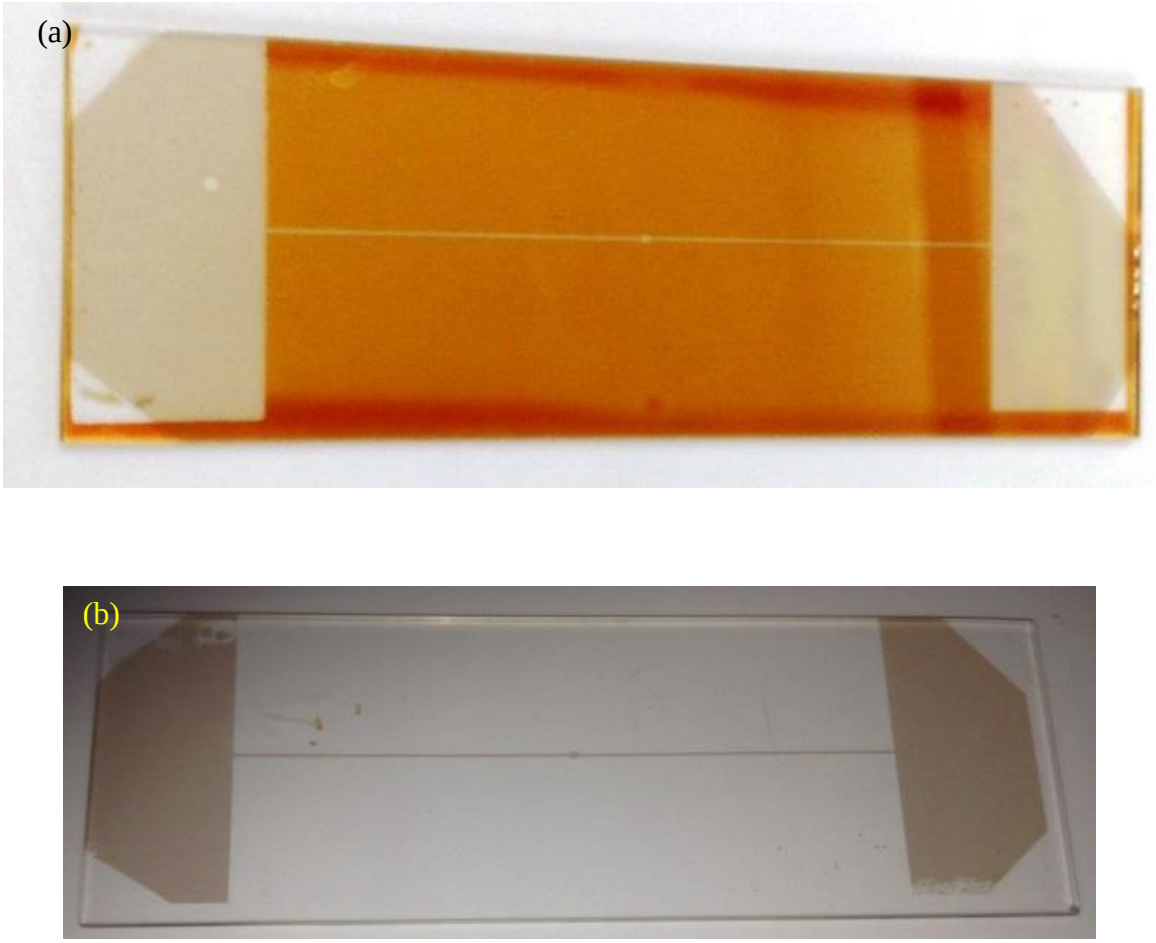


***Figure 3.3:*** *Bottom substrate fabrication. (a) Photoresist on glass substrate along with sputtered ITO metal (b) Glass with ITO only after lift-off process.*

The electrical resistance of sputtered ITO electrodes were found to be 200-250Ω by using a multimeter. This resistance will affect the electric field strength generation during experiments. Hence, the lower the resistance of the ITO metal, the stronger the electric field strength. Overall, the photolithography part of the biochip fabrication process is outlined in Table 3.1.

The full fabrication of the biochip required several further important steps. Figure 3.4 illustrates the overall fabrication process, including the micro-milling method to fabricate vertical wall electrodes. The overall process involves a fusion of photolithography and micro-milling methods.

*Table 3.1: Process parameters for fabrication of ITO electrode for DEP-induced 3D particle rotation.*

| **Process** | **Parameters** |
|---|---|
| Substrate pre-treatment | Treat with acetone, methanol, IPA in ultrasonic bath, followed by plasma $O_2$ asher 10 min at 100W |
| Coat AZ4562 photoresist adhesion layer | 1000 rpm for 30 sec |
| Soft-bake | 101°C for 50 sec |
| Exposure | Soft contact (single time for 30 sec) |
| Post-exposure bake | 101°C for 50 sec, ramp down to room temperature at 15°/hour |
| Develop | 10-15 min in PGMEA using ultrasonic bath |
| RF sputter | Sputter ITO for 60 min in magnetron sputtered in argon and $O_2$ |

Micro-milling is used to fabricate vertical wall electrodes by using CNC Mini- Mill/GX in which required 500 µm thick brass metals were milled. In particular, a brass strip of 500 µm in thickness is cut to 25mm square and glued (permanent epoxy) onto perspex. The brass is micro-milled at 30,000 rpm spindle/mill speed and 1.2 µm/s. At 17,000 rpm spindle speed, a small hole of 350 µm in diameter is drilled in the perspex to provide access to inject bovine cells. The micro milled part is then inverted and placed on top of glass consisting of patterned ITO, as shown in Figure 3.5. Finally, the vertical electrode part of the biochip is mounted

inversely on a glass substrate with suitable electrical connection supply to bottom ITO electrodes.

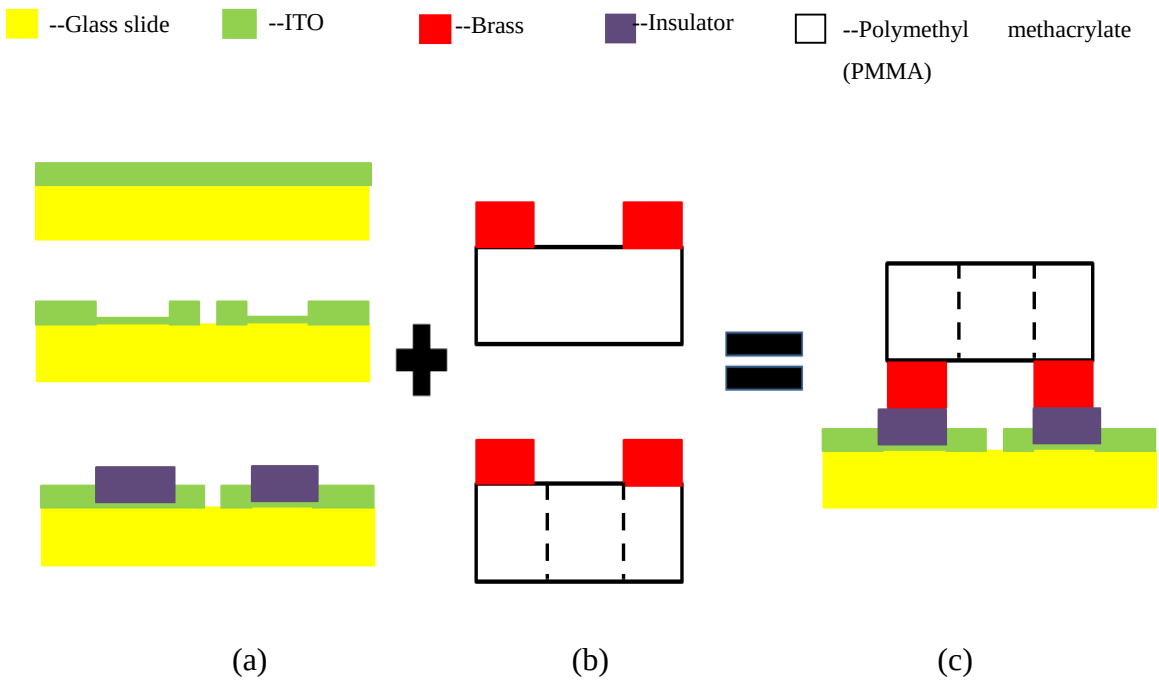


***Figure 3.4:*** *Fabrication process of biochip. (a) Stage one of fabrication involves photolithography to deposit ITO and 10µm cover slip acting as an insulator and glued at the centre with a small grove on top of glass substrate. (b) Second stage involves micro-milling brass on top of poly (methyl methacrylate) (PMMA) as vertical electrodes. (c) Assembly of two pieces. Figure not to scale.*

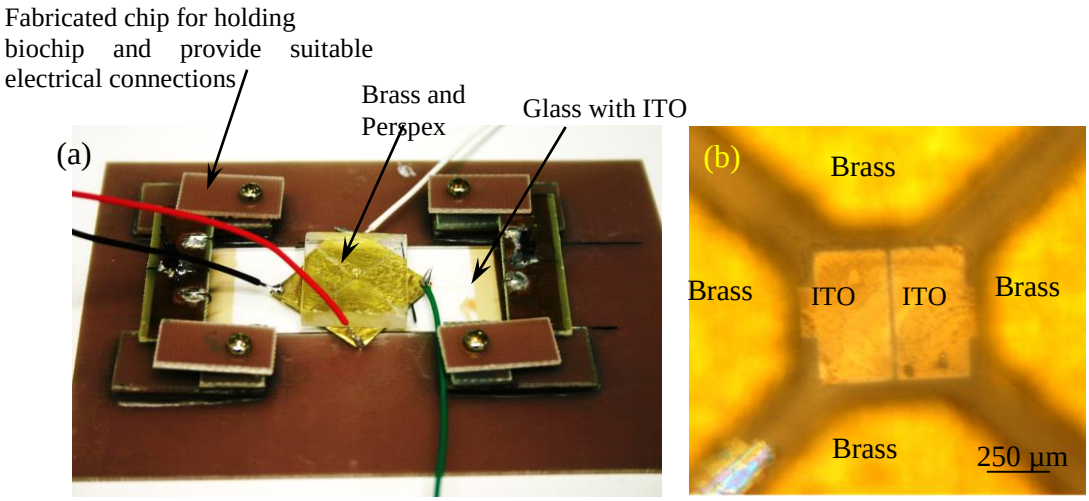


***Figure 3.5:*** *Fabricated biochip. (a) Fabricated biochip along with electrical connections. (b) Close-up view shows aligned vertical electrodes on bottom ITO. The chamber workspace is a 750-µm square area.*[41]

## 3.3. Overall process summary

Overall, fabrications of individual processed parts are shown in Figure 3.6. Vertical electrodes are aligned and glued on top of ITO coated glass substrate. After fabricating the device, inverted epi-fluorescent microscope is used to observe rotation of oocyte through transparent ITO electrode. A single oocyte is injected into the rotation chamber centre and ROT electric fields are applied.

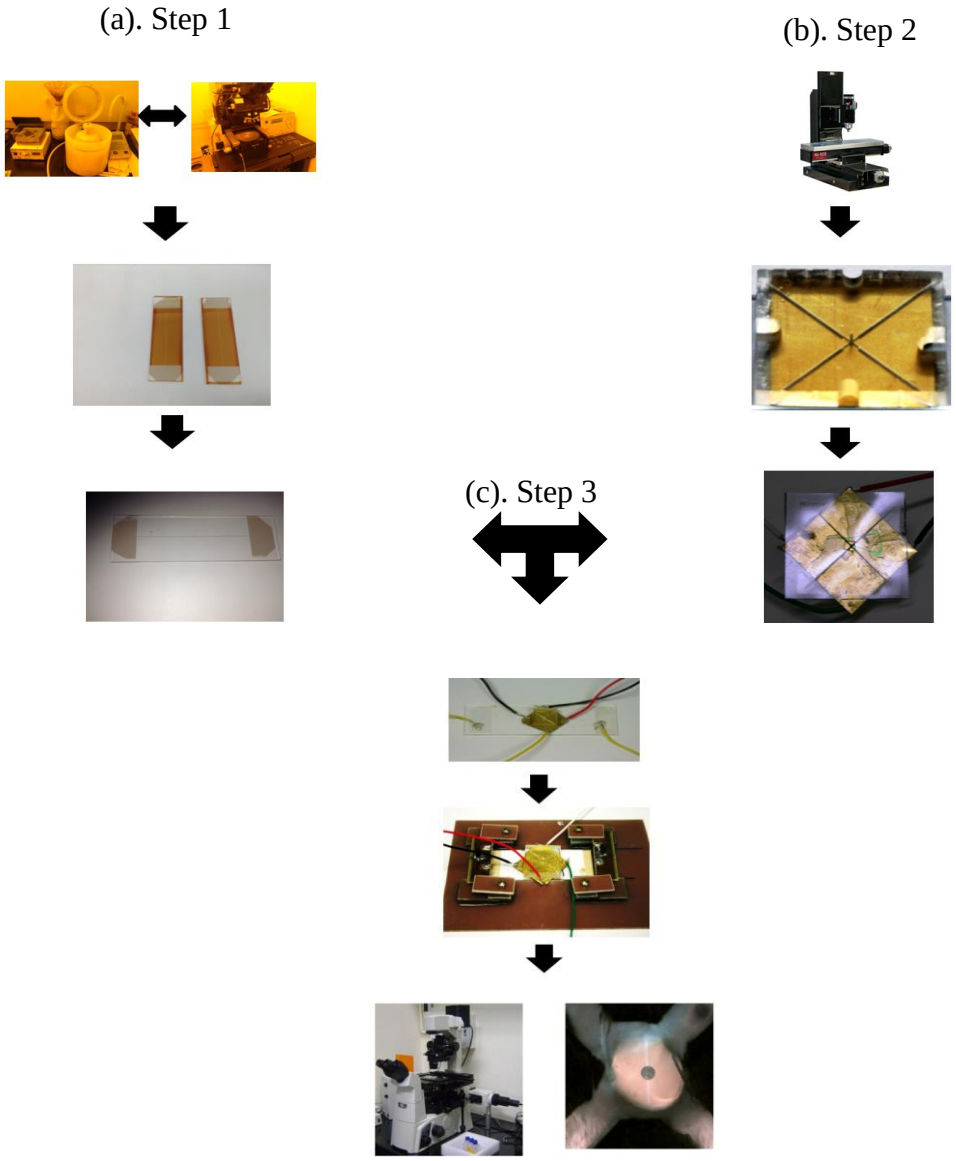


***Figure 3.6:*** *Overall fabrication process and parts. (a) Step1: fabrication of ITO electrode on top of glass. Spin coater and mask aligner instruments are used during this step along with lift-off using acetone. (b) Step2: Micro-milling 500µm brass is carried out using micro-miller. (c) Step: Assembly of ITO and vertical micro milled electrodes mounted on electronic chip for experimentation.*

## 3.4. Summary

Low cost fabrication of this biochip design requires a fusion of photolithography and micro-milling techniques. Bottom layer ITO electrodes were fabricated using photolithography. The ITO electrode resistance is required to be low to achieve better field strength, which is aided by this (high cost) process. The resulting electrodes are of high resolution and are suitable for experiments. In contrast, micro-milling is performed to obtain large, vertical square tipped electrodes at low cost and higher fabrication speed to yield a suitable cell rotation volume. Both fabricated parts are later aligned to obtain a biochip suitable for the validation experiments in this thesis. Overall, this chapter presents a biochip device design and a complete detailed fabrication procedure. Photolithography and micro-milling procedures are characterized for the high resolution required, and thus will define basic device performance.

# Chapter 4. Simulation of device design and optimization

In this chapter, numerical simulations are carried out to optimise a biochip specifically designed to rotate a single suspended dielectric bovine oocyte of ~120 µm diameter. Governing equation and boundary conditions are established to perform the numerical finite element analysis and optimization. Electrode dimension and the ROT chamber are characterised in terms of the parameters and variables required for DEP particle rotation. Yaw and pitch axis ROT fields are characterized numerically to asses performance.

## 4.1. Problem definition

Equation *(2.15)* shows that torque on the spherical particle depends solely upon three parameters, (i) Radius of cell (ii) Electric field strength and (iii) Imaginary part of Clausius-Mossotti (CM) factor. Diameter of the bovine oocyte is ~120 µm and this is a known factor, hence radius of oocyte is not considered as a variable (Note that in this thesis, size of the cell or bovine oocyte is kept constant, instead of considering it as a variable). The factors such as, imaginary part of CM factor cannot be optimized, since the dielectric properties of the bovine oocytes are yet unknown and hence one cannot optimize CM factor. CM factor also depend on the medium dielectric properties. For this purpose a brief discussion is given on the electrolyte concentration.

ROT electric field strength is a factor which can be optimized to obtain suitable field strength to rotate a single suspended cell. Hence, before fabrication, numerical simulation of the ROT field in the micro-device is essential to validate expected performance. Different size of dielectric particle sizes requires different electrode shape, electrode arrangement and the chamber design. Spherical particles, such as bovine oocytes, require electric field strength of the order of $10^4$ V/m [180, 181]. This field strength is the key parameter to optimise the electrode and rotation chamber design. Optimized electric field strength from the analysis is employed to determine the potential particle rotation rate.

## 4.2. Parameter optimization for cell rotation

One can optimize the behaviour of a ROT field according to several possible requirements. In this research, three key optimization parameters are used for ROT field optimization:

**(i) Electric field strength**

- Electrode arrangement
- Electrode shape
- Rotation chamber size

**(ii) 3D rotation field in yaw and pitch**

**(iii) Device geometry (Initial design concept)**

**(iv) Electrolyte concentration**

ROT electric field depends upon the arrangement of electrodes. Analysis of a circular tipped electrodes arranged circularly is considered for the initial analysis. After analysing the behaviour of the fields at the center of the chamber, then the shape of the electrodes were configured to check, which electrode shapes are suitable in this research. Finally, a rotation chamber is optimized to rotate a cell of size 120 µm in diameter. Following sections provide methods, results and discussion of ROT electric field optimization analysis results.

## 4.3. Method

Numerical methods most commonly used for field characterization are based on Mie theory [182, 183] or finite element and the finite difference time domain techniques. Finite-element analysis (FEA) is adopted to simulate electric fields in this research. Geometric models are drawn using the built-in tools in FEA software such as COMSOL v4.3a.

### 4.3.1. Governing equations and boundary conditions

Dielectrophoresis torque is a function of the electric field strength, medium and particle conductivities along with the permittivity factor. Thus, analysis of the ROT electric field strength generated by the vertical micro-electrodes within the rotation chamber (ROT) acts as an initial step. Electric field analysis is carried out using charge relaxation theory in which the flow of electric current through a conducting medium in the quasi-static case is governed by the equation of continuity which can be written in the form:

$$\nabla \cdot \left(\sigma \cdot \nabla V - \sigma \cdot E + \frac{\partial}{\partial t}(\epsilon_0 \epsilon_r \cdot \nabla V\right) = Q_j \qquad (4.1)$$

where, $\sigma$ is the conductivity tensor, $Q_j$ is a current source term which is zero in this study and $\epsilon_0$ is the permittivity of free space and $\epsilon_r$ is the relative permittivity tensor. Under static conditions, the electric potential ($V$) is defined by the equivalence:

$$\mathrm{E} = -\nabla V \qquad (4.2)$$

For the electric field analysis electrode is applied with an AC sinusoidal potential ($V$) along with phase shift ($\phi$) as:

$$V = A_0 \, sin(\omega t + \phi) \qquad (4.3)$$

where, $A_0$ is the amplitude, and $\omega$ is the angular frequency. From the AC voltage as a boundary condition on the vertical electrodes, electric field strength along with ROT direction are determined. Electrical fields are analysed at a single period at an interval of $\pi/2$.

## 4.4. Electrode field strength optimization

### 4.4.1. ROT field analysis for varying number of electrodes

Initially, circular tipped electrodes are arranged in circular arrangement, as in Figure 4.1, because they are simple and effective for model-based design. Combinations of 3D circular electrode designs are analysed to assess wider ROT field regions. Models of a micro-device consisting of three, four, six and eight circular electrodes placed evenly in a circular ring at a suitable distance are considered. As an initial step, electrical field analysis is carried out in the rotation chambers and the buffer medium is considered as dielectric water.

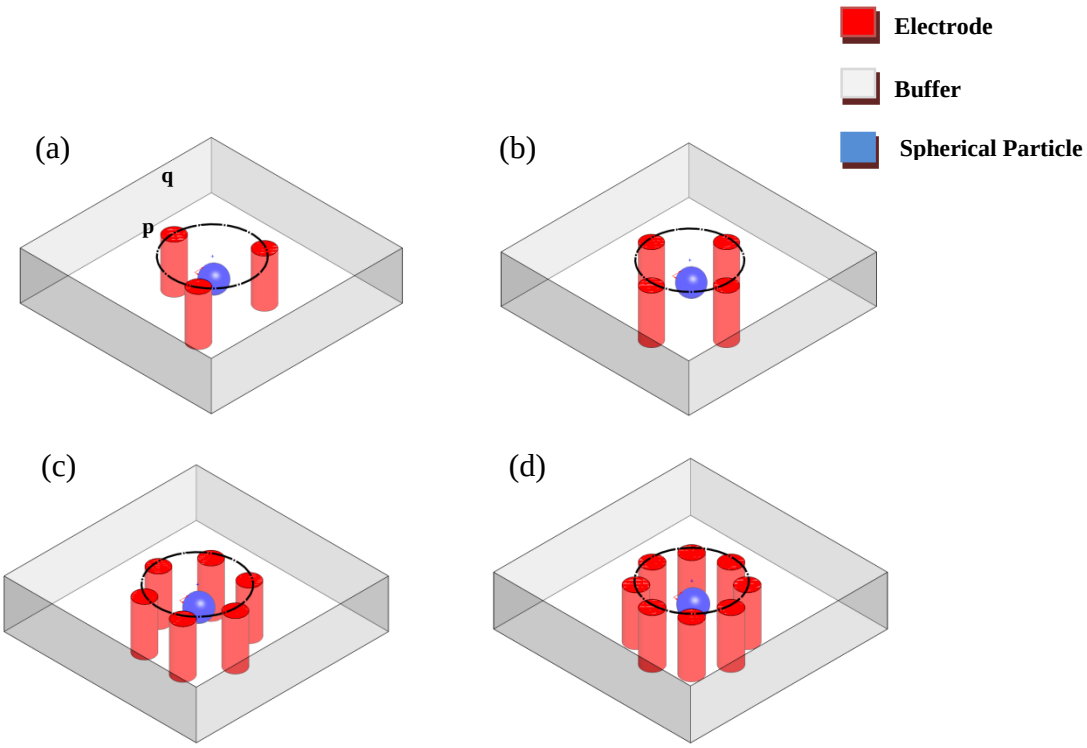


***Figure 4.1:*** *3D model device design arrangement with electrodes height of* $p$=500 $\mu m$ *and diameter of* $q$=150 $\mu m$. *(a). 3-electrode (b).4-electrode (c). 6-electrode (d). 8-electrode. A spherical particle is shown at the centre of each ROT chamber. Sphere radius is* 120 $\mu m$. *Electrodes in the four configurations are all evenly spaced in a circle of diameter of* 1200 $\mu m$. ***Figure not to scale.***

The ROT electric field is initially analysed for the strength consistency along a line 1200 $\mu m$ from the center. Figure 4.2 shows the distribution of electric field strength analysis for the three, four, six, and eight electrode arrangements respectively. High resolution plots of electric field strength variation along the center to the electrode tip indicate that electric field strength

increases in magnitude with the increased number of electrode arrangements. Four, six and eight electrode arrangements provide suitable ROT fields because of the uniformity of the rotating fields generated within 400 $\mu m$ square chamber. However, the six and eight electrode arrangements provide the most uniform distribution at electric field strength in the ROT chamber. About 85% of the fields within 1200 $\mu m$ center region consist of ROT fields with constant electric field strength for the eight electrode arrangement. Hence, the electric field distribution for eight electrode chamber is considered suitable to obtain a distribution of constant field magnitude in a wider rotation region suitable for rotating larger diameter particles and cells.

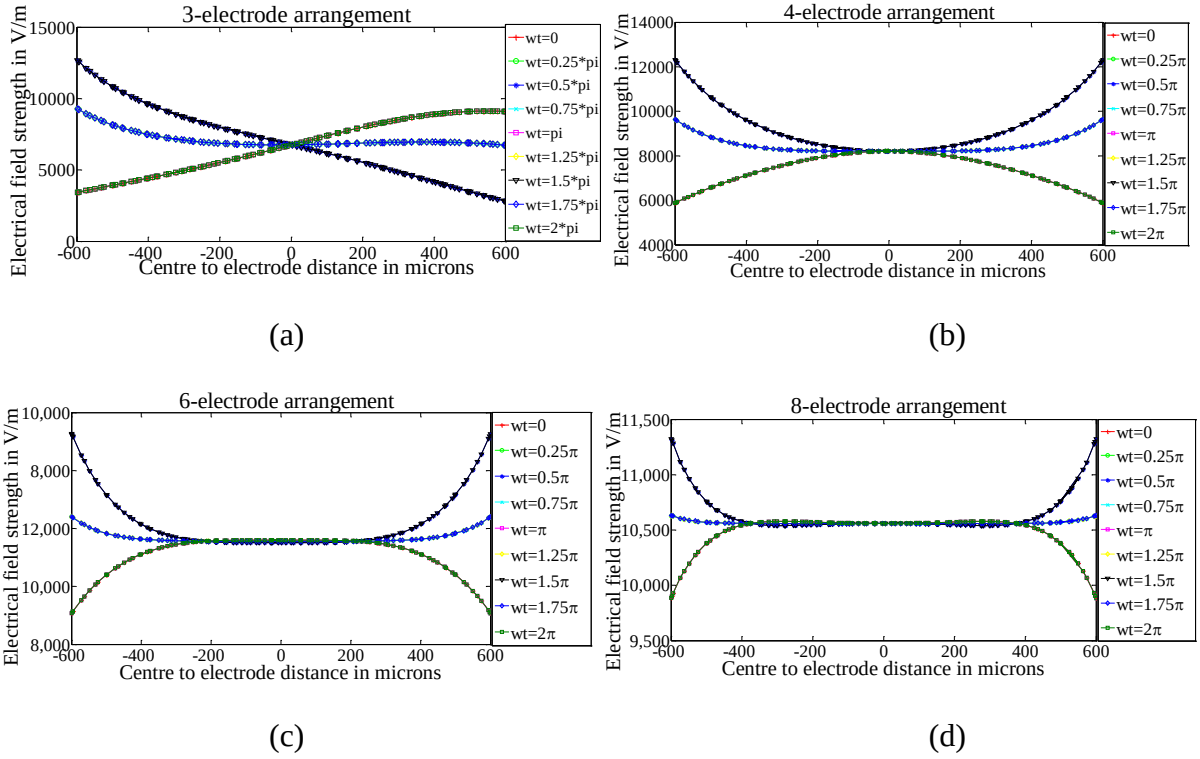


***Figure 4.2:*** *ROT field analysis at* 1200 × 1200 *center region. (a). Three electrode arrangement consisting of uniform rotation field with constant field at the center. (b). Four electrode arrangement consisting of uniform rotation fields with constant field magnitude within* 150$\mu m$ $region$. *(c).Six electrode arrangement consisting of uniform rotation fields with constant field magnitude within* 300 $\mu m$ $region$. *(d).Eight electrode arrangement showing uniform constant magnitude rotation regions between* 400 $\mu m$.

## 4.4.2. ROT field analysis for different electrode shape

Circular and square tipped 3D electrodes are considered in this study, as shown in Figure 4.3, considering the suspended spherical particle. The spherical particle at the centre is neglected during initial simulations as the behaviour of the ROT fields is being characterised. A $1500\ \mu m \times 1500\ \mu m$ square shaped liquid domain is defined and extruded to $500\ \mu m$. Circular electrodes of $150\ \mu m$ in diameter or square tipped electrodes of $150\ \mu m$ side length are introduced by even placement on a circle and extruded to a height of $500\ \mu m$.

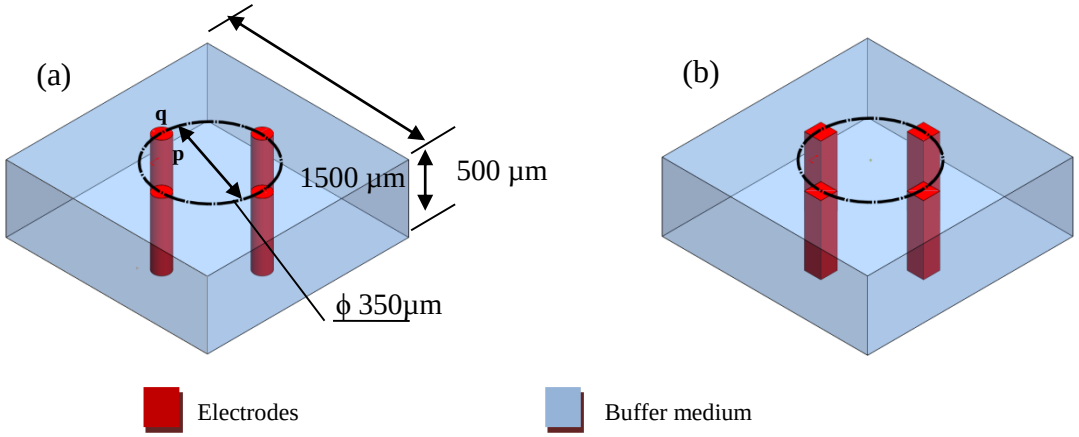


***Figure 4.3:*** *3D model device design arrangement with electrodes height of p=500 µm and diameter of q=150 µm. (a). 4-circular electrode (b).4-Square electrode. Electrodes in the four configurations are all evenly spaced in a circle of diameter of* 350 µm. *Figure not to scale.*

The parameters in Table 4.1 are employed to simulate ROT field strength. Alternating fields vary with the time and AC frequency, so analysing field strength will provide information about rotation capability. An AC electric potential boundary condition is applied with a phase shift interval of $360°/n$ on each of the n electrodes.

In each model, extremely fine mesh is generated of the order of $3 \times 10^4$ elements and finite nodes. On each of these elements the electric field gradient is calculated. The resulting fields are analysed numerically in Matlab v2002a, at high resolution of the order $10 \times 10\ \mu m$ at the center to determine the effective ROT field regions within the device.

***Table 4.1:*** *Parameter constant of electrode and medium for the calculation of electric field strength*

| **Item** | **Relative permittivity ($\epsilon$)** | **Conductivity($\sigma$)** |
|---|---|---|
| Vertical electrode/Brass | 1 | 5.998e7[S/m] |
| Bottom electrode/ITO | 1 | 150 $\frac{\Omega}{\text{sq}}$(Internal resistance) |
| Buffer medium (DI water) [184] | 78 | 5.5e-6 (S/m) |

### 4.4.2.1. Design

The steps involved for designing the model in COMSOL v4.3a include:

**Step 1: Setting up the model**

The 3D model is designed by considering the 2D micron sale geometries. Figure 4.4, shows the initial model created.

**Step 2: Defining material properties and selection of material domain**

Material properties are defined considering Table 4.1. Electrodes are defined as one domain with specific material properties. Similarly, the liquid buffer solution is considered as one domain.

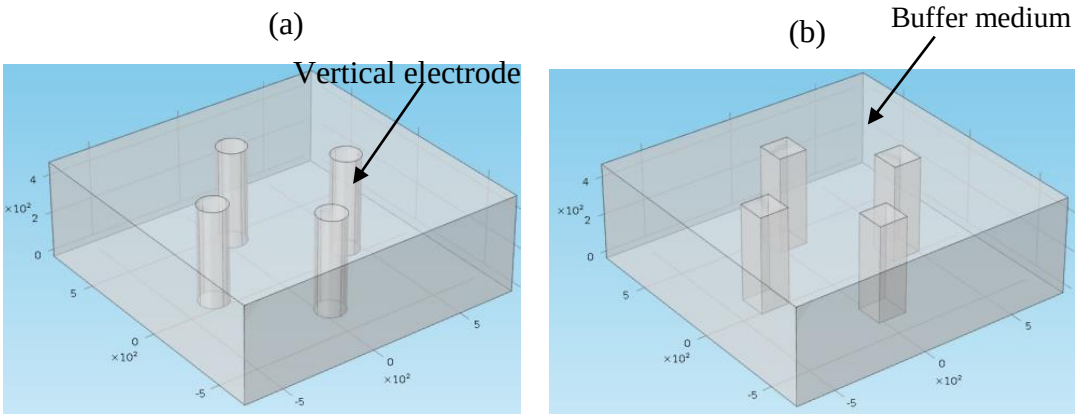


***Figure 4.4:*** *3D geometry for electro rotation analysis. (a) 4-circular tip electrode arrangement. (b) 4-square tip electrode arrangement.*

**Step 3: Pre-processing (selection of domains for electric field generation)**

An AC sinusoidal electric potential of peak to peak amplitude 10V and a constant frequency is applied on the edge of electrodes with 90° phase shift from electrode to electrode. The circular shaped cell or object is chosen as a polarising object. An electric field analysis mesh is generated consisting of an extremely fine mesh with 11467 nodes.

**Step 4: Post-processing (analysis of the applied electric field)**

A stationary simulation solver is used to investigate the effect of a single period of $\omega t = 0, 0.5\pi, \pi, 1.5\pi$. The results are exported into Matlab to obtain a high resolution image to clearly understand the behaviour of the induced fields at a micron scale near the centre region where the cells will be placed. ROT fields are analysed for rotation around the yaw-axis at different periods along with a sinusoidal potential and phase shifts. Period steps of 0 to $2\pi$ seconds are considered to assess the field variations. The data from COMSOL is exported into Matlab software to get a higher resolution image of $10 \times 10\ \mu m$.

Figure 4.5-4.13, shows the results for a square tipped electrode situation. It is evident from the simulation that the electric field near the centre region remains uniform with very minute field strength variations for the square tipped electrode arrangement.

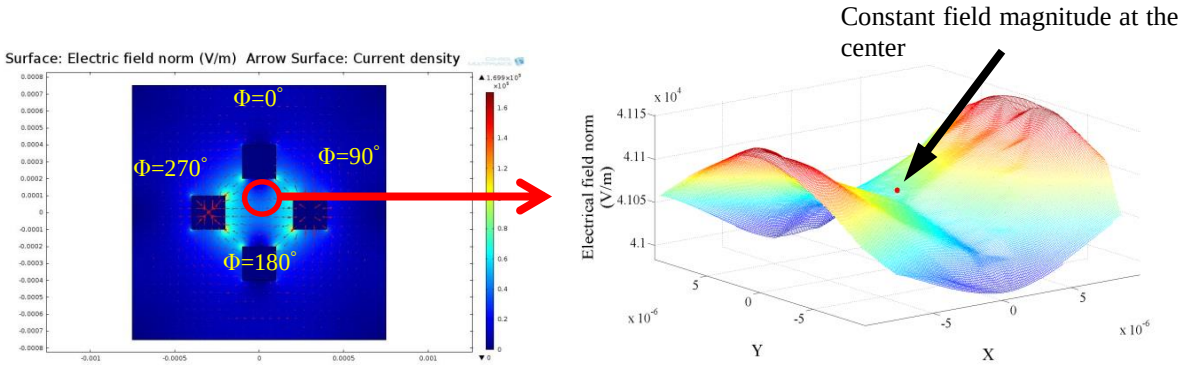


(a) (b)

***Figure 4.5:*** *Electric field simulation for a square tipped electrode arrangement. Applied voltage at the orthogonal square tipped electrode sin(0+ ϕ) (a).COMSOL finite element analysis of electric field (b).* $10 \times 10$ *μm plot of electric field along z-axis with a probe at the centre to estimate the electric field magnitude using Matlab software.*

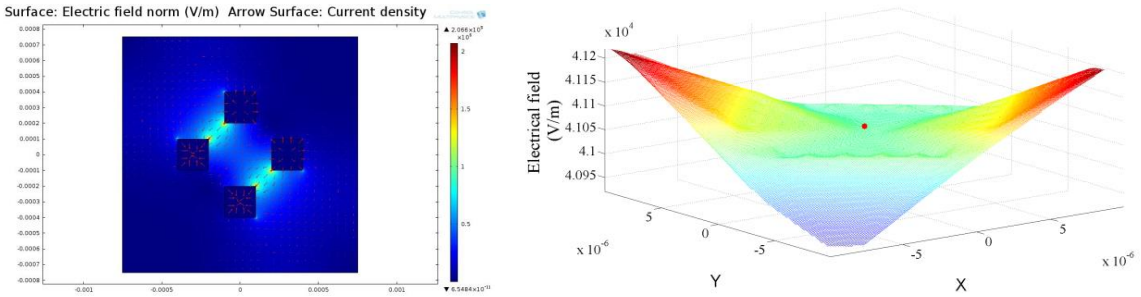


(a) (b)

***Figure 4.6:*** *Electric field simulation for a square tipped electrode arrangement. Applied voltage at the orthogonal square tipped electrode sin(0.25π+ ϕ) (a).COMSOL finite element analysis of electric field (b).* $10 \times 10$ *μm plot of electric field along z-axis with a probe at the centre to estimate the electric field magnitude using Matlab software.*

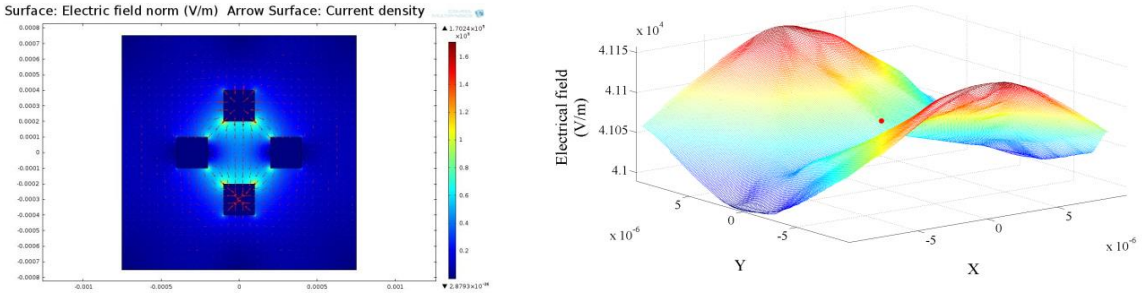


(a) (b)

***Figure 4.7:*** *Electric field simulation for a square tipped electrode arrangement. Applied voltage at the orthogonal square tipped electrode sin(0.5π + ϕ) (a).COMSOL finite element analysis of electric field (b).* 10 × 10 µm *plot of electric field along z-axis with a probe at the centre to estimate the electric field magnitude using Matlab software.*

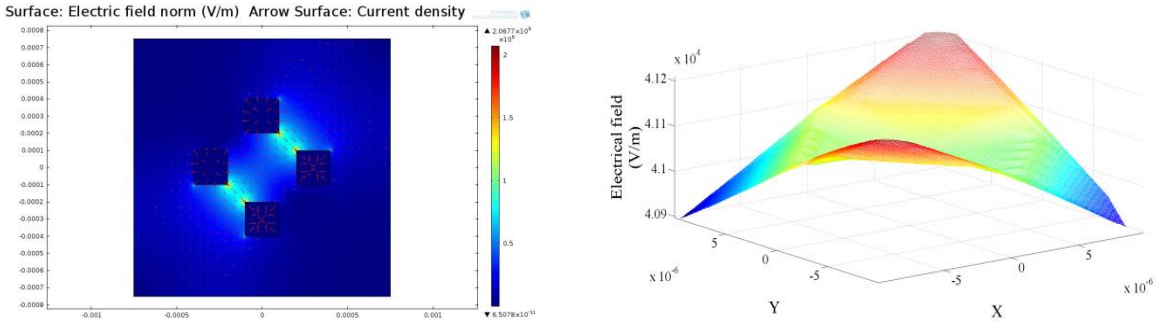


(a) (b)

***Figure 4.8:*** *Electric field simulation for a square tipped electrode arrangement. Applied voltage at the orthogonal square tipped electrode sin(0.75π +φ) (a).COMSOL finite element analysis of electric field (b).* 10 × 10 µm *Plot of electric field along z-axis with a probe at the centre to estimate the electric field magnitude using Matlab software.*

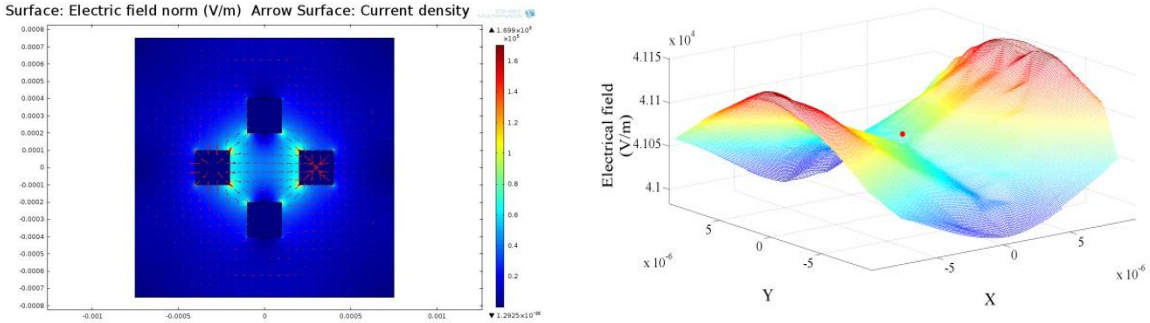


(a) (b)

***Figure 4.9:*** *Electric field simulation for a square tipped electrode arrangement. Applied voltage at the orthogonal square tipped electrode sin(π +φ) (a).COMSOL finite element analysis of electric field (b).* 10 × 10 µm *plot of electric field along z-axis with a probe at the centre to estimate the electric field magnitude using Matlab software.*

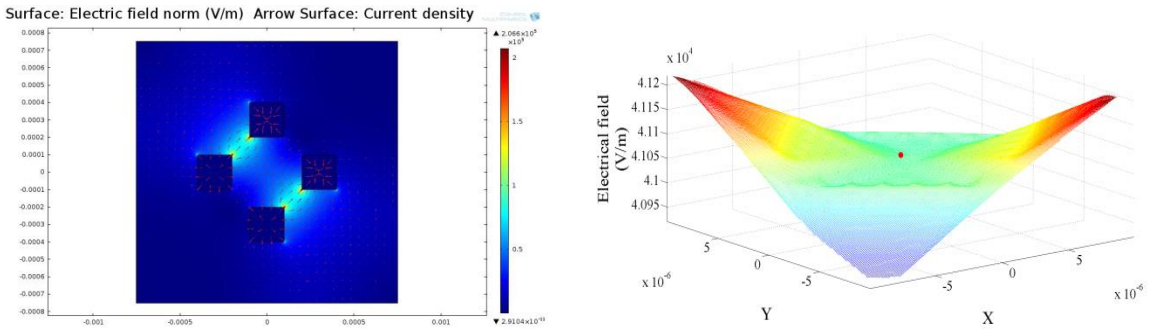


(a) (b)

***Figure 4.10:*** *Electric field simulation for a square tipped electrode arrangement. Applied voltage at the orthogonal square tipped electrode sin(1.25π +φ) (a).COMSOL finite element analysis of electric field (b).* 10 × 10 µ*m plot of electric field along z-axis with a probe at the centre to estimate the electric field magnitude using Matlab software.*

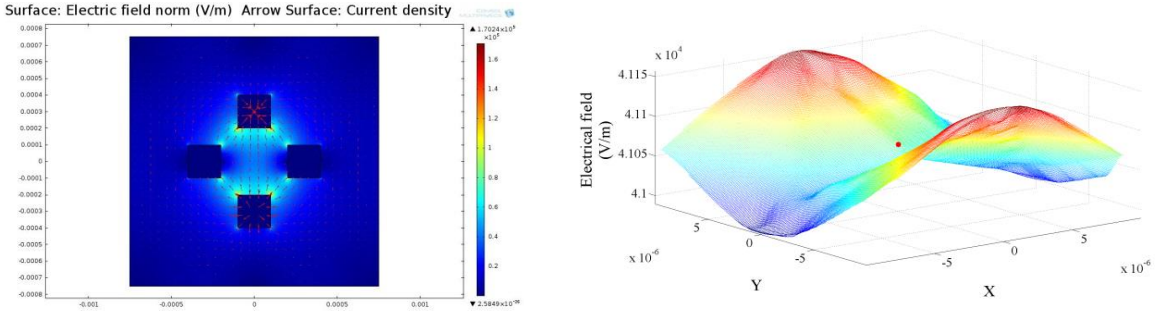


(a) (b)

***Figure 4.11:*** *Electric field simulation for a square tipped electrode arrangement. Applied voltage at the orthogonal square tipped electrode sin(1.5π +φ) (a).COMSOL finite element analysis of electric field (b).* 10 × 10 µ*m plot of electric field along z-axis with a probe at the centre to estimate the electric field magnitude using Matlab software.*

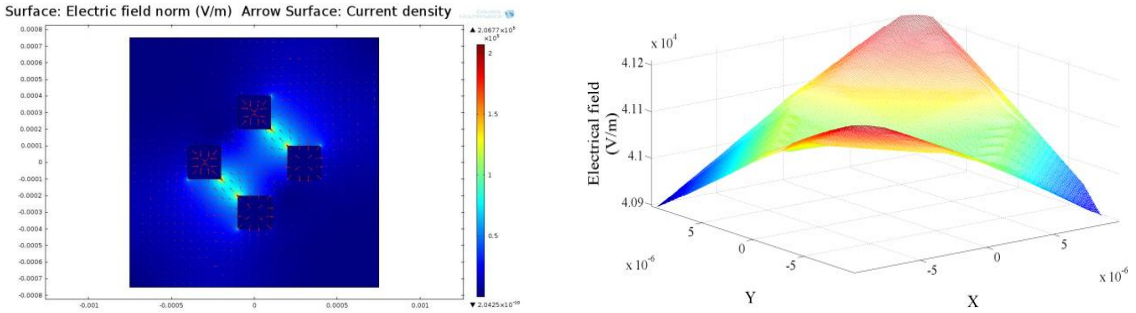


(a) (b)

***Figure 4.12:*** *Electric field simulation for a square tipped electrode arrangement. Applied voltage at the orthogonal square tipped electrode sin(1.75π +φ) (a).COMSOL finite element analysis of electric field (b).* 10 × 10 µ*m plot of electric field along z-axis with a probe at the centre to estimate the electric field magnitude using Matlab software.*

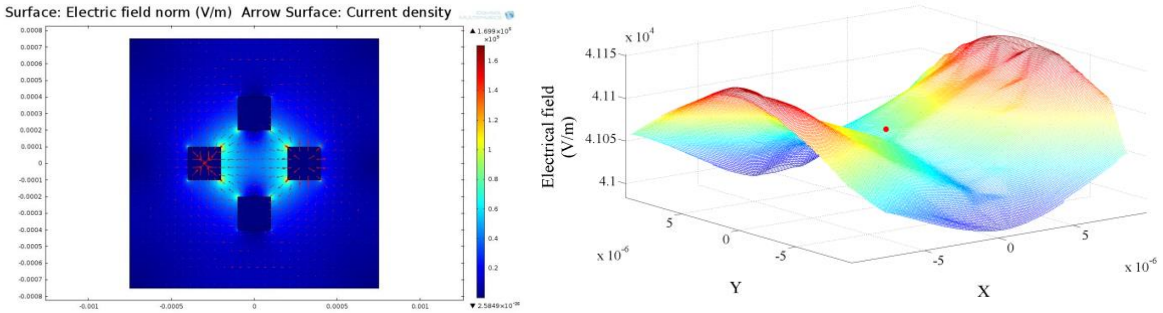


(a) (b)

***Figure 4.13:*** *Electric field simulation for a square tipped electrode arrangement. Applied voltage at the orthogonal square tipped electrode sin(2π +φ) (a).COMSOL finite element analysis of electric field (b).* 10 × 10 µm *plot of electric field along z-axis with a probe at the centre to estimate the electric field magnitude using Matlab software.*

Next, a circular tipped electrode shape is considered, as shown in Figure 4.14-4.22. Electric field magnitude norm arrows show the periodic variations at different a sinusoidal voltage. Periodic steps of 0 to 2π seconds are considered. It is again evident from the simulation that the electric field at the centre remains uniform in magnitude with very minute field strength variations for both square and circular tipped electrode arrangements. The data for the electric field at the centre of cell rotation chamber is also as shown in Table 4.2 and Table 4.3.

.

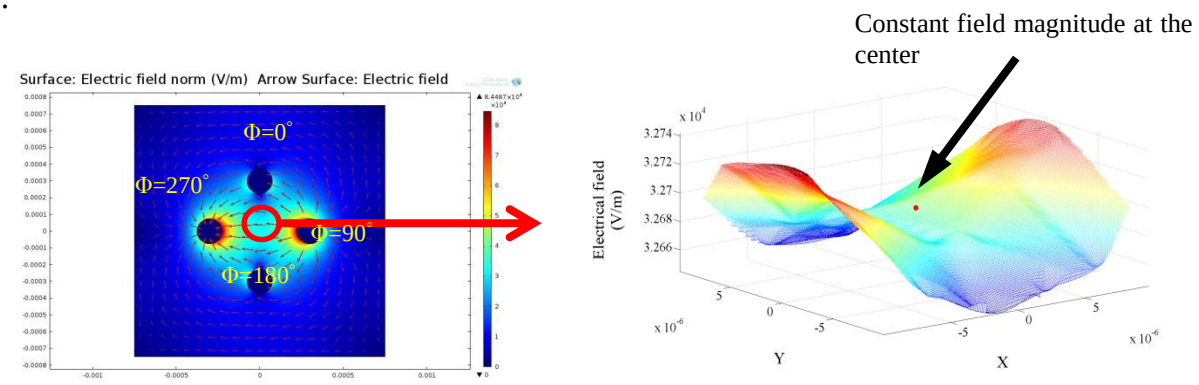


(a) (b)

***Figure 4.14:*** *Electric field simulation for a circular tipped electrode arrangement. Applied voltage at the orthogonal circular tipped electrode sin(0+φ) (a).COMSOL finite element analysis of electric field (b).* 10 × 10 µm *plot of electric field along z-axis with a probe at the centre to estimate the electric field magnitude using Matlab software.*

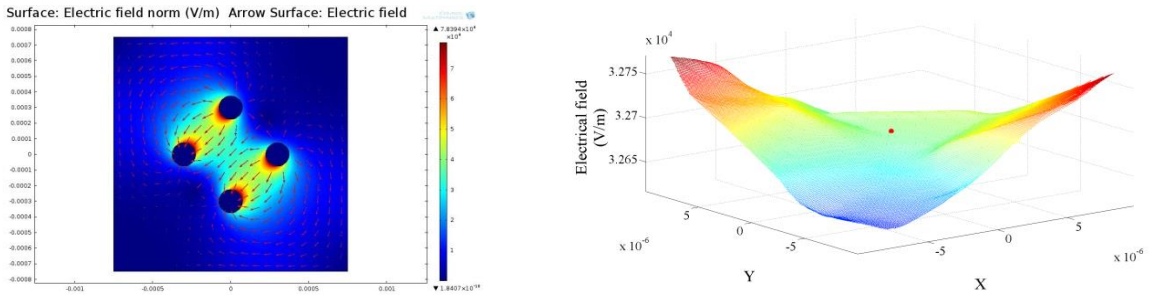


(a) (b)

***Figure 4.15:*** *Electric field simulation for a circular tipped electrode arrangement. Applied voltage at the orthogonal circular tipped electrode sin(0.25π+φ) (a).COMSOL finite element analysis of electric field (b).* 10 × 10 μm *plot of electric field along z-axis with a probe at the centre to estimate the electric field magnitude using Matlab software.*

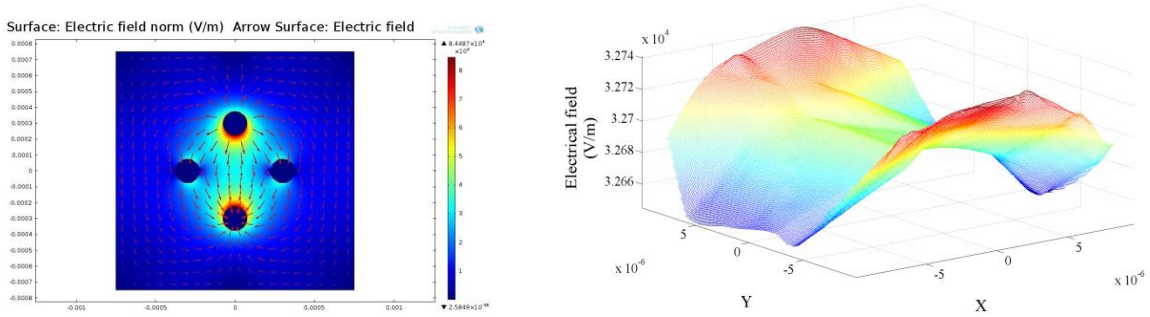


(a) (b)

***Figure 4.16:*** *Electric field simulation for a circular tipped electrode arrangement. Applied voltage at the orthogonal circular tipped electrode sin(0.5π +φ) (a).COMSOL finite element analysis of electric field (b).* 10 × 10 μm *plot of electric field along z-axis with a probe at the centre to estimate the electric field magnitude using Matlab software.*

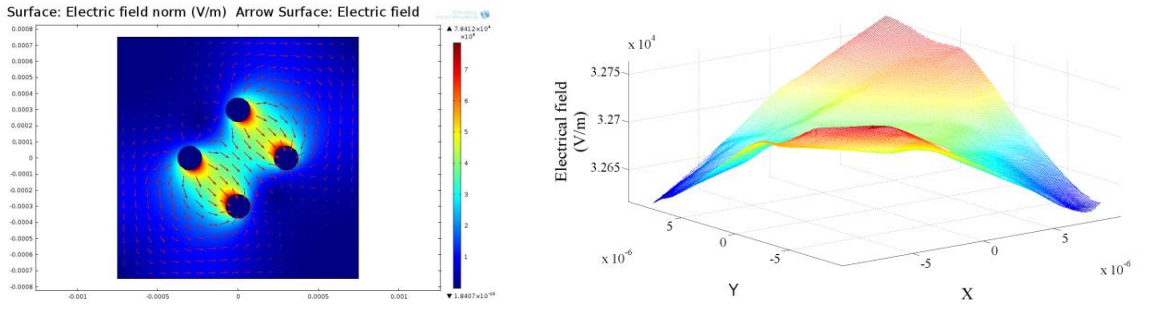


(a) (b)

***Figure 4.17:*** *Electric field simulation for a circular tipped electrode arrangement. Applied voltage at the orthogonal circular tipped electrode sin(0.75π +φ) (a).COMSOL finite element analysis of electric field (b).* 10 × 10 μm *plot of electric field along z-axis with a probe at the centre to estimate the electric field magnitude using Matlab software.*

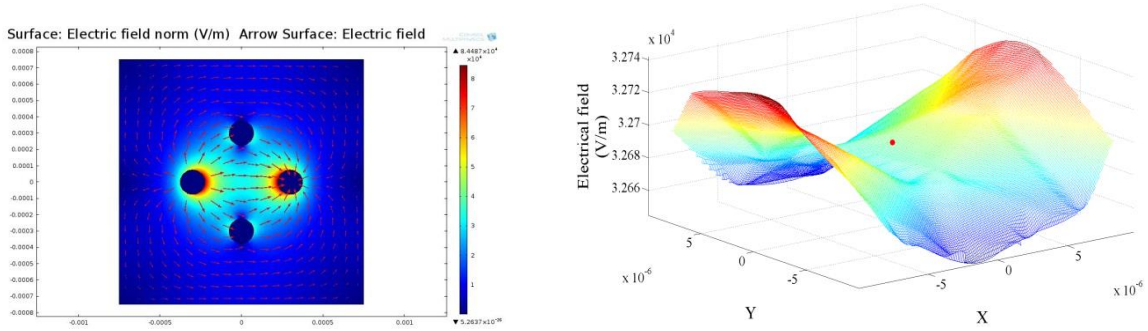


(a) (b)

***Figure 4.18:*** *Electric field simulation for a circular tipped electrode arrangement. Applied voltage at the orthogonal circular tipped electrode sin(π +φ) (a).COMSOL finite element analysis of electric field (b).* 10 × 10 μm *plot of electric field along z-axis with a probe at the centre to estimate the electric field magnitude using Matlab software.*

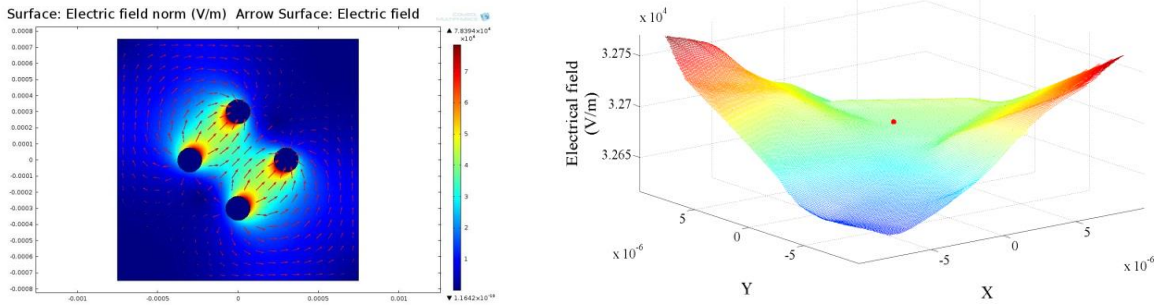


(a) (b)

***Figure 4.19:*** *Electric field simulation for a circular tipped electrode arrangement. Applied voltage at the orthogonal circular tipped electrode sin(1.25π +φ) (a).COMSOL finite element analysis of electric field (b).* 10 × 10 μm *plot of electric field along z-axis with a probe at the centre to estimate the electric field magnitude using Matlab software.*

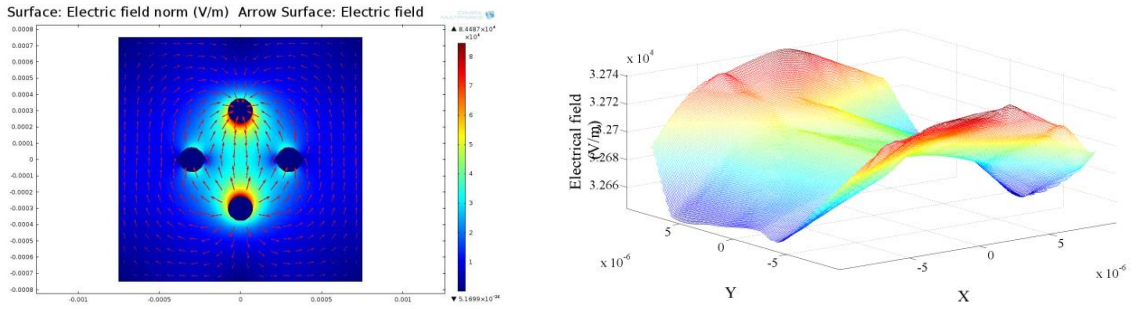


(a) (b)

***Figure 4.20:*** *Electric field simulation for a circular tipped electrode arrangement. Applied voltage at the orthogonal circular tipped electrode sin(1.5π +φ) (a).COMSOL finite element analysis of electric field (b).* 10 × 10 μm *plot of electric field along z-axis with a probe at the centre to estimate the electric field magnitude using Matlab software.*

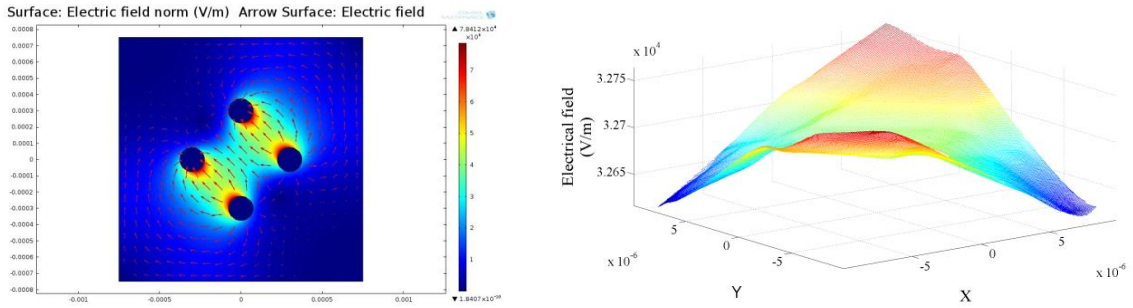


(a) (b)

***Figure 4.21:*** *Electric field simulation for a circular tipped electrode arrangement. Applied voltage at the orthogonal circular tipped electrode sin(1.75π +φ) (a).COMSOL finite element analysis of electric field (b).* 10 × 10 µm *plot of electric field along z-axis with a probe at the centre to estimate the electric field magnitude using Matlab software.*

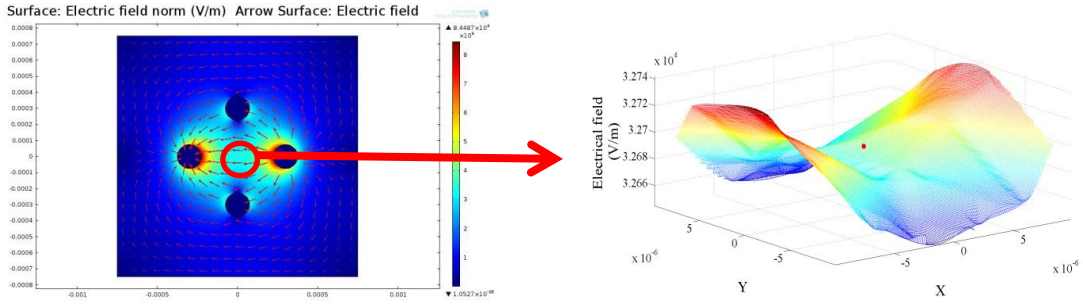


(a) (b)

***Figure 4.22:*** *Electric field simulation for a circular tipped electrode arrangement. Applied voltage at the orthogonal circular tipped electrode sin(2π +φ) (a).COMSOL finite element analysis of electric field (b).* 10 × 10 µm *plot of electric field along z-axis with a probe at the centre to estimate the electric field magnitude using Matlab software.*

The fields remain uniform in all the case along with non-varying average electric field. This means that there is the ROT electric fields generated are constant in magnitude at the center of the chamber compared to its surroundings. This also means that there is minimum or negligible field strength in magnitude at the centre and hence, the electric field strength in the ROT torque equation *(2.15*) is a constant factor. Further, the simulation results show that by considering constant magnitude ROT electric field strength, one can optimize the rotation field behaviour.

***Table 4.2:*** *Electric field from square tipped electrode*

| **Applied wave** | **Electric field norm(V/m)** | **Average field 10×10μm region** | **%Standard deviation 10×10 μm region** |
|---|---|---|---|
| sin(0+φ) | 4.107e+04 | 4.106e+04 | 0 |
| sin(0.25π+φ) | 4.107e+04 | 4.107e+04 | 0 |
| sin(0.5π +φ) | 4.107e+04 | 4.105e+04 | 0.002 |
| sin(0.75π +φ) | 4.107e+04 | 4.102e+04 | 0.004 |
| sin(π +φ) | 4.107e+04 | 4.107e+04 | 0 |
| sin(1.25π +φ) | 4.107e+04 | 4.107e+04 | 0.001 |
| sin(1.5π +φ) | 4.107e+04 | 4.107e+04 | 0 |
| sin(1.75π +φ) | 4.107e+04 | 4.105e+04 | 0 |
| sin(2π +φ) | 4.107e+04 | 4.104e+04 | 0 |

The percentage standard deviation is calculated by dividing the standard deviation by the mean values. These values also indicate very minute deviation from the mean. Hence, it can be concluded that the AC ROT electric field strength in magnitude at the centre of the rotation chamber remains constant. This outcome is the key finding of this first analysis- as it is essential to rotate dielectric particles.

Simulations are also carried out for different combinations of radius and thickness of the circular tipped electrodes. Table 4.4, shows the electric field variations for different combinations of circular tipped electrodes. Thickness had a negligible effect on the electric field near the centre region and was thus neglected for further analysis.

***Table 4.3:*** *Electric field from circular tipped electrode*

| Applied wave | Electric field norm(V/m) | Average field10×10 µm region | %Standard deviation10×10 µm region |
|---|---|---|---|
| sin(0+φ) | 3.269e+04 | 3.269e+04 | 0 |
| sin(0.25π+φ) | 3.269e+04 | 3.269e+04 | 0 |
| sin(0.5π +φ) | 3.269e+04 | 3.268e+04 | 0.001 |
| sin(0.75π +φ) | 3.269e+04 | 3.268e+04 | 0.001 |
| sin(π +φ) | 3.269e+04 | 3.268e+04 | 0.001 |
| sin(1.25π +φ) | 3.269e+04 | 3.268e+04 | 0.001 |
| sin(1.5π +φ) | 3.269e+04 | 3.269e+04 | 0 |
| sin(1.75π +φ) | 3.269e+04 | 3.269e+04 | 0 |
| sin(2π +φ) | 3.269e+04 | 3.269e+04 | 0 |

Square tipped electrodes are suitable for rotation of cells, due to the increased electric field strength near the centre chamber. However, circular tipped electrodes also generate efficient gradient fields. Square tipped electrodes are considered in further analysis to optimize the rotation chamber, this is because,

- Square tipped electrodes are easier to fabricate by micro-milling.
- Square tipped electrodes provide higher field gradient at the centre, making it more suitable to rotate bigger size particles if necessary.

Hence, a square rotation chamber is analysed for square spacing to handle and rotate a bovine oocyte of 120µm diameter. It is to be noted that electrorotation chamber (EROT) needs to be at least 300µm side to easily inject the oocyte into the rotation chamber.

***Table 4.4:*** *Electric field estimation for varying thickness of electrodes*

| Exp. No. | Radius of circular electrode (µm) | Rotation chamber/ distance between tip of electrodes (µm) | Thickness of electrode (µm) | Amplitude (Vp-p) | Electric field (V/m) |
|---|---|---|---|---|---|
| 1 | 250 | 300 | 50 | 10 | 5.42e+04 |
| 2 | 250 | 300 | 100 | 10 | 5.41e+04 |
| 3 | 250 | 300 | 200 | 10 | 5.41e+04 |
| 4 | 250 | 300 | 300 | 10 | 5.40e+04 |
| 5 | 250 | 300 | 800 | 10 | 5.39e+04 |
| 6 | 150 | 300 | 50 | 10 | 2.55e+04 |
| 7 | 150 | 300 | 100 | 10 | 2.54e+04 |
| 8 | 150 | 300 | 200 | 10 | 2.54e+04 |
| 9 | 150 | 300 | 300 | 10 | 2.52e+04 |
| 10 | 150 | 300 | 800 | 10 | 2.51e+04 |
| 11 | 150 | 500 | 50 | 10 | 1.41e+04 |
| 12 | 150 | 500 | 100 | 10 | 1.40e+04 |
| 13 | 150 | 500 | 200 | 10 | 1.40e+04 |
| 14 | 150 | 500 | 300 | 10 | 1.39e+04 |
| 15 | 150 | 500 | 800 | 10 | 1.38e+04 |

### 4.4.3. ROT chamber optimization

Electric field strength rotating at the center of the ROT chamber is one of the essential parameters to calculate DEP torque on a spherical particle. Analysis of this rotating vector at the center point of rotation region thus provides vital information to characterise device performance potential. Figure 4.23, shows the variation of electric field strength for the two

pairs of square tipped orthogonal electrodes at different ROT chamber sizes. At the center of each ROT chamber field strength is determined at the incremental values of $0, 0.25\pi, 0.5\pi, 0.75\pi, \pi, 1.25\pi, 1.5\pi, 1.75\pi \; and \; 2\pi$. Results shows that field strength increases with decreasing chamber size at the center, as expected. Magnitude of the electric field within each of the rotation chamber for a single period remains constant. Even though constant magnitude of the field strength is found at the center point of each chamber, the strength of the field varies surrounding the center region.

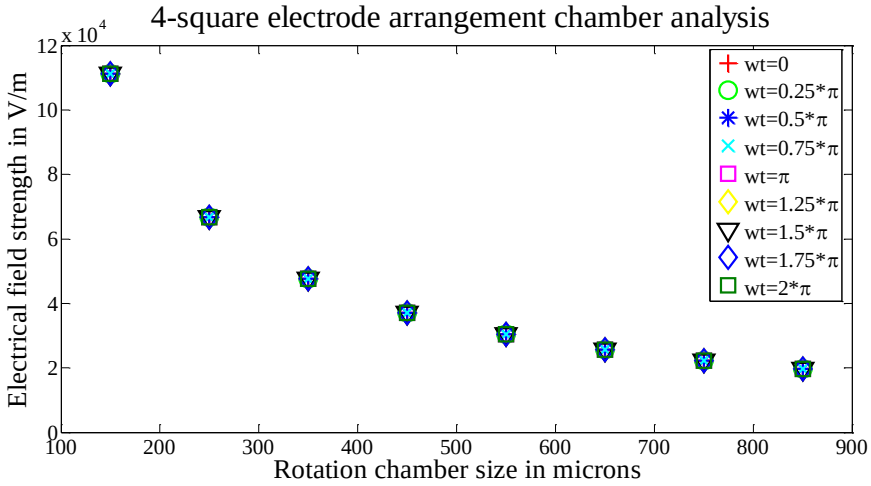


***Figure 4.23:*** *Electric field strength data is taken at the center of the ROT chamber. Fields at different period varies directly proportional to the decrease in size of the chamber size. Four square shaped electrode arrangements are used to obtain the field strength.*

Field strength with a chamber size between 150 to 850 µm is appropriate to obtain 120µm bovine oocyte rotation. In particular, within a 150 to 850 µm square chamber side, a constant rotating electric field strength of magnitude 2-3 $\times 10^4 \, V/m$ can be generated and is sufficient to polarise and create a net moment on the suspended particle. Initially, a square chamber size of 750µm is chosen for ease of manufacturing and handling bovine oocyte. Electric field strength at the center of a $750 \; \mu m$ square ROT chamber is determined to be$2.2 \times 10^4 \, V/m$. Further, this field strength is suitable to avoid electrophoresis or any damage to the cell [79], if handled carefully.

### 4.4.3.1. DEP torque from simulation

The DEP torque from Equation *(2.15*) is solely dependent upon the applied AC field frequency and complex material parameters. Therefore, torque equation merely reduces to a variable function of the CM factor (see Equation (*(2.4*)) leading to the numerical calculation of angular velocity or the DEP torque on polarizable particles (see Equation ((2.16)). One can therefore assume the dielectric properties of the particle and the buffer medium from Table 4.1 for calculating dielectric spectrum numerically. One such rotation spectrum plot is shown in Figure 4.24, where a constant electric field magnitude of $2.2 \times 10^4 V/m$ is considered from the simulation results. In this analysis polystyrene beads and bovine oocytes are treated as solid spherical homogeneous particles to obtain angular velocity plots and as a solid shell model [149, 152, 185] for the numerical modelling. Note that the single solid shell model provides an accurate approximation for how a bovine oocyte may actually behave in practice in the designed biochip.

Figure 4.24, shows that the rotation rate of the bovine oocyte is higher than the polystyrene bead because of the low density, and higher conductivity. Moreover, the two peaks indicate clockwise and anticlockwise rotation of the particles. The negative peak indicates particle polarizability more than that of the medium, and the positive peak indicates less polarizability of particle than that of the surrounding medium. Maxwell Wagner (MW) relaxation can be seen at frequency of 550 KHz. During this period particle polarizability becomes equal to that of the surrounding medium making it stationary for a moment. This frequency at which particle polarizability reaches to that of the medium is called the critical frequency [125, 153]. In a similar way one can obtain a dielectric spectrum plot of particle rotation rate by simulating electric fields. Numerical analysis of dielectric spectrum plots provides further valuable guidance to validate experimental results.

Simulation results of rotational electric fields act as a basis to estimate the dielectric spectrum of particles. DEP-induced rotation of the particle is solely dependent upon characterising rotating electric fields. Simulation results of these fields showed a constant magnitude of the rotating field strength as the essential parameter to characterize and configure electrodes and rotational workspace. It is also critical to precise constant controllable rotation.

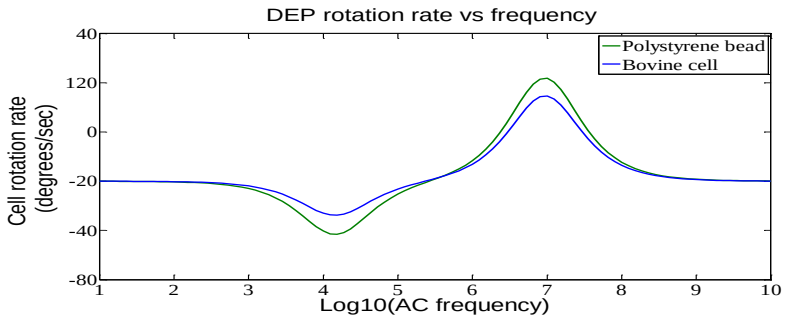


***Figure 4.24:*** *Frequency dependency of particle rotation on complex conductivity and permittivity factors of cell and the surrounding medium. Table 1 is used as a reference to obtain these plots (a). Real part of CM factor (b). Imaginary part indicates a positive peak for particle rotation in clockwise direction. Negative peak indicates particle rotation in anticlockwise direction. (c). Rotation rate of bovine cell and polystyrene bead at* $2\times10^4$ *V/m field strength.*

Further results showed that wider regions of constant rotational field strength can be obtained by configuring number of electrodes. Increased wider rotational field regions imply that one can introduce a single cell or a particle at any point within the rotational workspace to induce a similar DEP torque. This outcome is advantageous because it provides flexibility during the picking and placing of biological entities in a wider rotation field without risk of losing rotation or control. Specifically a single cell can be placed in any region within the configured rotational workspace to obtain effective DEP-induced rotation and trapping, thus avoiding directing the particles into the center.

## 4.5. 3D rotation field optimization in yaw and pitch

Figure 4.25, shows the AC potential schemes for rotations in yaw and pitch respectively. The AC potential scheme in Figure 4.25a, generates a rotational electric field about the yaw-axis. The AC potential scheme in Figure 4.25b generates a rotational electric field about the pitch axis. Combination of the yaw-axis and the pitch-axis rotational fields can be generated by the application of boundary potentials on the respective electrodes.

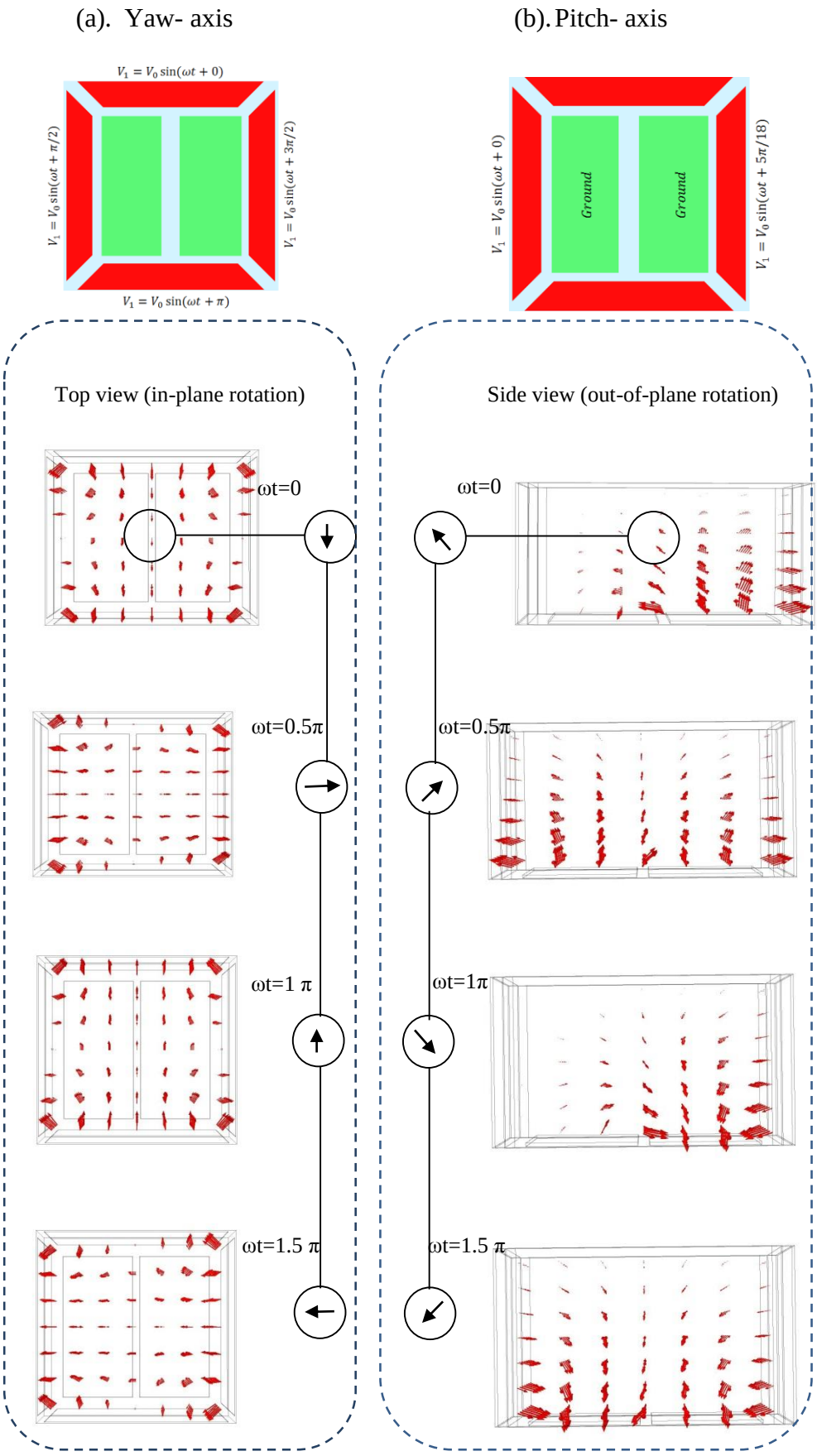


***Figure 4.25:*** Electric field analysis. (a) In-plane rotation: top view. (b) Pitch rotation: side view. Complete rotation of electric field for a single period of ωt=0 to 1.5π, using COMSOL v4.3 FEA software. ω-angular frequency of the applied ac electric field and t-time in seconds. Arrow vectors length and thickness correspond to field strength [41].

Spherical particle during simulation is not considered in this case to check for rotational fields in yaw and pitch. During yaw and pitch rotational fields, electric field normal arrow makes one complete rotation at the centre region for the period between 0, 0.5π, π and 1.5 π. This indicates that the designed biochip or micro-device is suitable for generation of rotation fields in 3D spaces. By controlling the frequency of the applied field, it is thus possible to control the direction and magnitude of the rotating fields during 3D rotation.

## 4.6. Electrolyte concentration

Whenever biological particles are subjected to non-uniform or uniform electric fields, dipoles are generated on the opposite poles of the particle. These dipoles make the particle polarizable along with the surrounding electrolyte medium. Hence, rotation of a single suspended particle in a rotating field depends primarily on the electrolyte concentration.

If the medium is dense or highly viscous, then the ionic distribution across the medium and the particle will be negligible. This negligible distribution results in negligible polarization of the particle, and thus no net movement or rotation. If the electrolyte concentration is low, the particles start to float in the medium, making it difficult to control particle handling. Hence, one needs to optimize the electrolyte concentration. However, optimizing a suitable buffer medium (electrolyte) to suspend a neutrally charged particle perfectly is extremely difficult, where room temperature and local heating make it harder to optimize the electrolytic concentration.

To optimise the medium concentration, a mixture of dextrose and sucrose are added by weight to volume ratio (w/v). A number of mixture iterations are carried out to assess the resulting medium conductivity. It was determined that four possible concentrations of electrolyte at different medium conductivity are suitable to suspend a bovine oocyte of ~120 µm in diameter. These concentrations are 3.5 µS/cm, 5.7 µS/cm, 9.5 µS/cm and 11.3 µS/cm. The significance of buffer medium conductivity is further highlighted in Chapter 6.

## 4.7. Device geometry (Initial device concept)

After analysing the behaviour of rotational fields in the rotation chamber the rotation chamber size is calibrated to obtain rotational fields in yaw and pitch axes, as shown in Figure 4.26. Finally, in this designed rotation chamber, transparent Indium Tin Oxide (ITO) electrodes are introduced to specifically add the ability to induce pitch-axis rotation, and a spherical particle is introduced for further analysis to assess potential device performance for comparison to experiment tests.

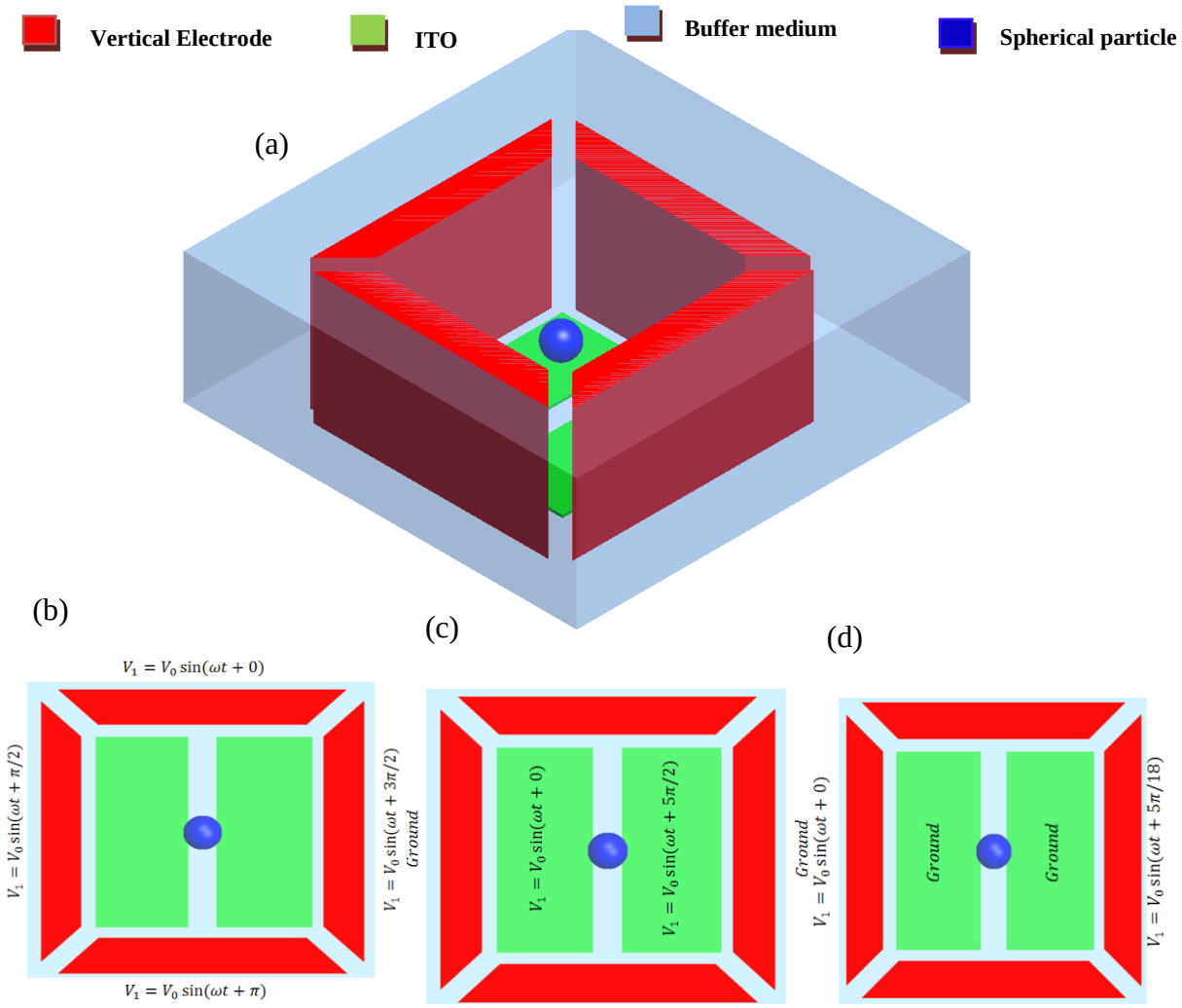


***Figure 4.26:*** *Device layout for 3D rotation in yaw and pitch axis. (a) Iso metric-3D model device design arrangement. (b). Yaw-axis rotation principle. (c). Pitch-axis rotation principle. (d). Alternative pitch-axis rotation principle. Figure not to scale.*

## 4.8. Summary

In this chapter, in depth simulation and numerical analysis is carried out to design, optimise and validate the biochip. Electrode designs to obtain suitable DEP rotational fields are calibrated and the rotation chamber is optimized. The DEP torque is numerically simulated and results generated to validate cell rotation experiments. Concepts of yaw and pitch-axis rotational fields are defined and analysed. From the analysis, a broader understanding of the concept of DEP induced dielectric particle rotation is established.

# Chapter 5. Cell rotation measurement

In the previous Chapters 3-4, device fabrication protocols and simulation results has been outlined to carry out experiments. The first section of this chapter will discuss specifically the actual finalised experimental setup that utilised the biochip used in Chapter 3. This includes the experimental setup, data collection and the post processing using an image processing algorithm in order to determine the frequency dependent dielectric spectrum of the bovine oocyte. Materials used during storage and handling of the bovine oocytes is discussed. Limitations along with assumptions employed during the experiments are also discussed.

## 5.1. Experimental Setup

The experimental setup consists of an inverted epi-fluorescent microscope mounted on an anti-vibration table, as shown in Figure 5.1. The biochip and insulated electrical connections are immersed in a glass jar containing buffer solution, as shown in Figure 5.2. A four channel TGA1240 series 40MHz arbitrary waveform generator is used to provide suitable AC signals to the micro-electrodes with the desired phase shifts.

Oocyte rotation was imaged in bright-field mode at 10 × objective using an inverted Nikon Eclipse 80i microscope (Nikon Instruments Inc., Americas). A computer is interfaced with the inverted microscope to capture video and images of particle rotation at high resolution. Video files during experiments are captured from bandicam (Bandisoft Inc., USA) software with 30Hz sampling frequency for each individual oocyte. Videos are then analysed offline using customized image processing software, ImageJ 1.47n (National Institute of Health, USA). Angular velocity was estimated manually by picking rotating pixel points in ImageJ.

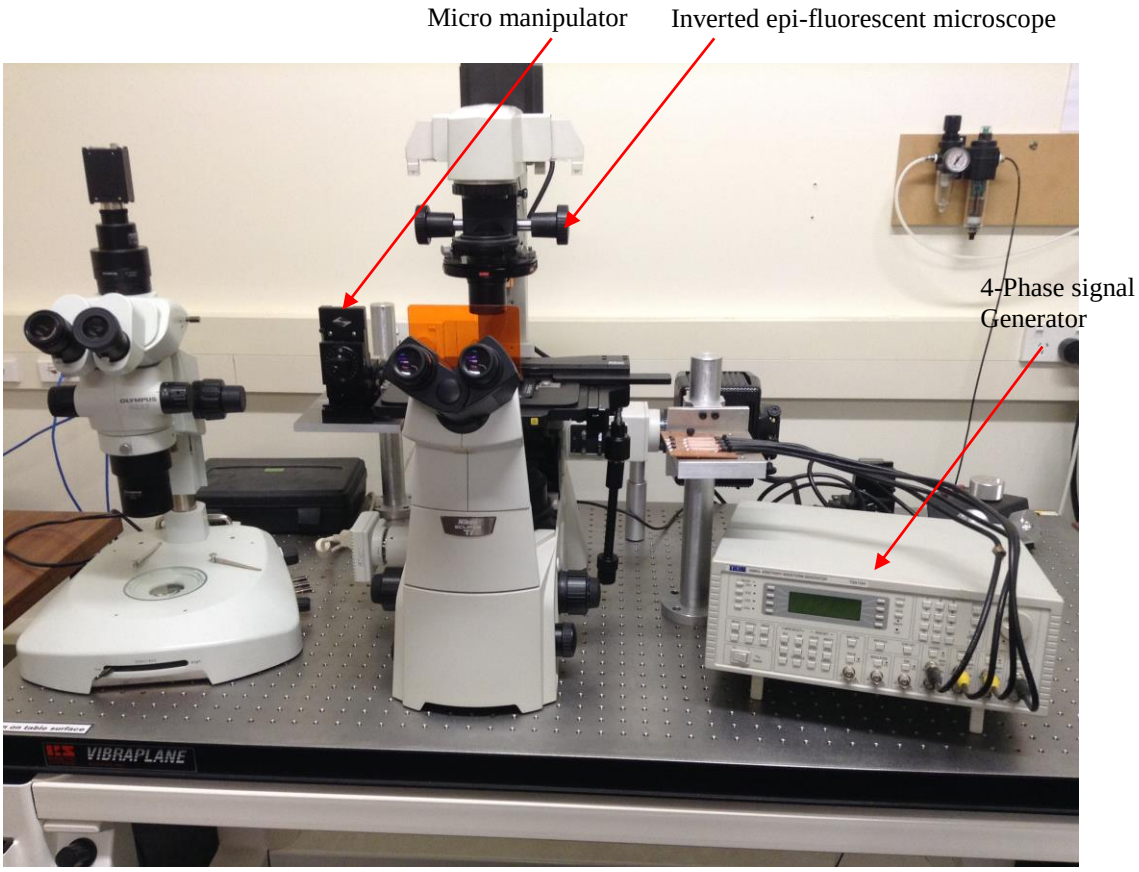


***Figure 5.1:*** *Electro-rotation experimental device setup. Inverted epi-fluorescent microscope is employed with computer interfaced with the computer.*

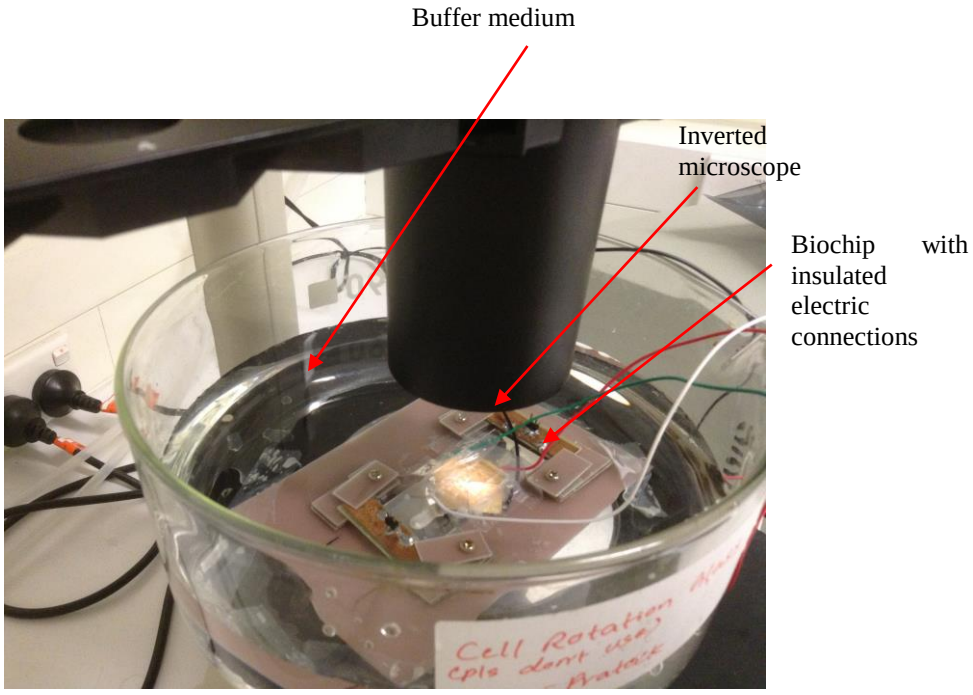


***Figure 5.2:*** *Electro-rotation experimental device setup. Inverted epi-fluorescent microscope is employed with computer interfaced with the computer.*

Hypoosmolar buffer medium was used in all the experiments to maintain oocyte viability [186]. Electric conductivity of the buffer medium during experiments is determined using Portable pH/conductivity meter (Thermo Fisher Scientific, US).

## 5.2. Materials

### 5.2.1. Oocyte preparation

Cumulus cells are collected from bovine ovaries from a slaughter house. Metaphase two (MII) oocytes are extracted from two 5ml vial containing cumulus-cells. Oocytes are treated first with hyaluronidase for removing cumulus cells surrounding the oocyte, as shown in Figure 5.3. Both zona-intact and zona-free oocytes as shown in Figure 5.3b-c are analysed during experiments. For zona-free oocyte collection, later Pronase is used to remove the zona from zona-intact cells. Sterile HSOF solution is used to wash the oocytes. Zona-free eggs are then held at room temperature. The micro-device along with fabricated chip is submerged in a beaker containing buffer solution made up of 0.85% dextrose and 3% sucrose by weight ratio. Matured oocytes are then manually injected from a mouth pipette into the ROT chamber.

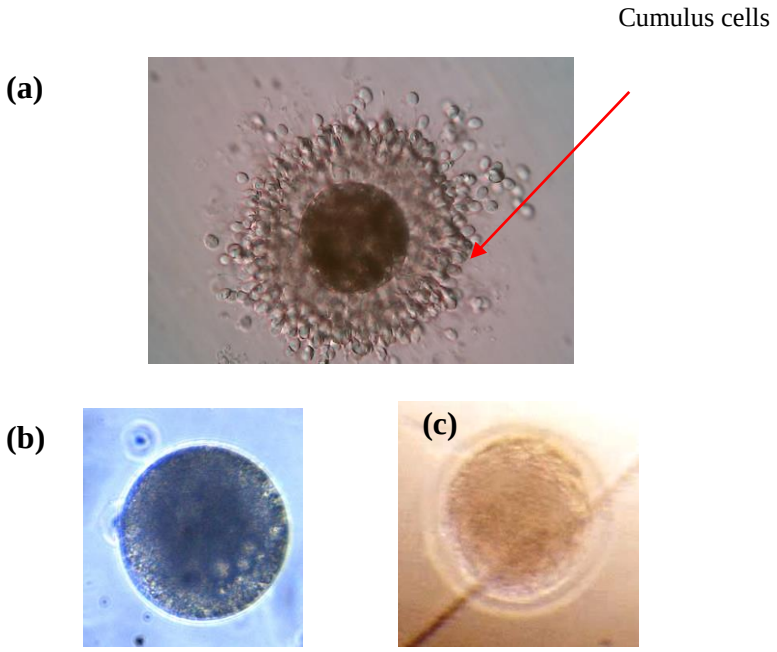


***Figure 5.3:*** *Preparation of bovine oocyte for experiments. (a) Oocyte surrounded by cumulus oocytes (b) Zona free oocyte. (c) Zona-intact oocyte.*

### 5.2.2. Oocyte handling in rotation chamber

A single Zona-free and zona-intact oocyte is extracted from the group through a micropipette. Through a series of dilution process and experience, single oocyte is injected inside the rotation chamber center consisting of buffer medium, before applying AC signals. Care should be taken while placing the oocyte at the centre chamber, as oocytes consist of lower density or weight, making it challenging to handle a single oocyte.

## 5.3. Post processing

Experimental video data are collected in a desktop interfaced with the video camera and the microscope. High definition videos are captured and processed using an image processing software such as ImageJ to calculate the dielectric spectrum.

### 5.3.1. Image processing and rotation measurement

In order to calculate the corresponding rotational velocity, an image processing manual tracking algorithm was employed to determine the angular change along successive frames. In particular, when the cell has a yaw-axis rotation, it is like a flat disk rotates about its center. Using this observation, we are able to draw a line in each video frame connecting two consistent reference points on the cell, one is the cell center and the other a feature point on the circumference of the cell, as shown in Figure 5.4. The angle between this line and the horizontal line is denoted by theta (θ). The change in θ between each two successive frames is denoted by $\partial\theta$, then the rotation rate can be given by $\Omega=\partial\theta/\Delta t$, where $\Delta t$ is the sampling period ($\Delta t=1/f=0.33s$). In practice, to accommodate the case when $\partial\theta$ is immeasurable, angle change in several successive frames divided by that time period for the rotation rate ($\Omega$) is considered.

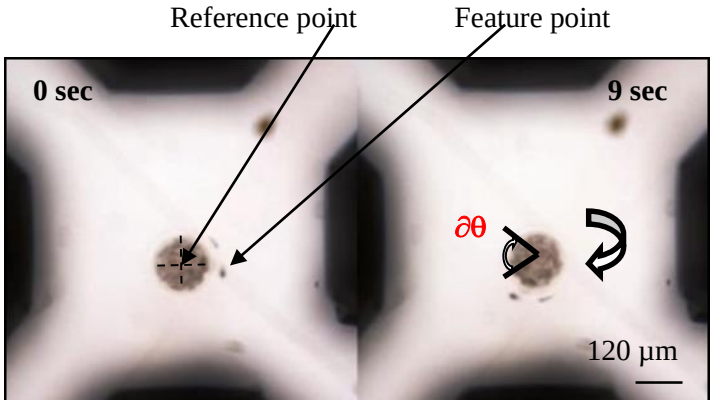


***Figure 5.4:*** *Manual tracking of rotation of oocyte in yaw-axis. A single bovine oocyte undergoing yaw axis rotation at 10 Vp-p, 500 kHz frequency and 90° phase shift between two pairs of orthogonally arranged vertical electrodes.*

When the cell has a pitch-axis rotation, it resembles a rolling sphere. Due to the cell's extremely complicated texture, a feature point with unique gray-level properties is impossible to choose from the cell, posing a problem to estimate the rotation rate by tracking feature points. To roughly estimate the rotation rate, hereby we assume the cell rolls without any sliding. With this assumption, we measure the distance (denoted by d) the cell travels between two successive frames, then the rotation rate can be given by $\Psi=d/(r\cdot\Delta t)$, where r is the cell radius, as shown in Figure 5.5. In practice, similarly to the case for yaw-axis rotation, to accommodate the case when d is immeasurable, we use the distance in several successive frames divided by that time period for the rotation rate $\Psi$.

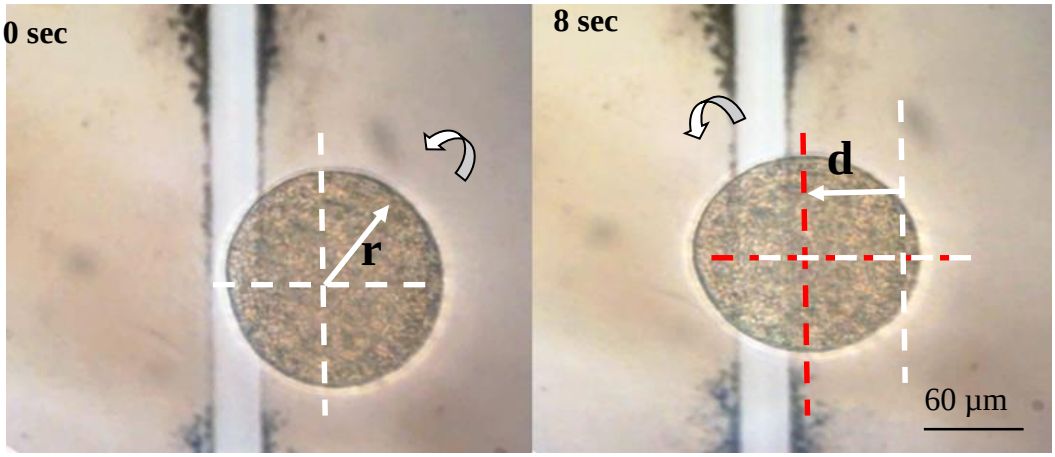


***Figure 5.5:*** *Manual tracking of rotation of oocyte in pitch-axis. A single bovine oocyte undergoing pitch axis rotation at 10 Vp-p, 80 kHz frequency and 50° phase shift between two pairs of orthogonally arranged vertical electrodes.*

## 5.4. Limitations and Assumptions

EROT involves the study of variation of different parameters, complex conductivity, complex permittivity, and electric field. Due to the increased amount of variables and parameters, it makes the problems more challenging. Hence, in this research, the goals are limited to obtain experimental rotation by varying AC amplitude, frequency, and phase and buffer medium conductivity. Detailed experimental analyses are presented in Chapters 6-7.

During experimentation, certain parameters are assumed, such as buffer medium permittivity, viscosity and oocyte diameter to approximately ~120μm. Since, DEP-based electrorotation torque on the particle or cell is directly proportional to the radius of the particle, 5% variation in diameter will provide increased or decreased electrorotation rate. However, the radius of cell is considered as constant in this research as the effect of diameter variation is negligible in determining the rotation rate. Then Bovine oocytes are considered as spherical dielectric objects in this research and a shell model [149] is also considered for analytical validation of dielectric spectrum and rotation measurements. The effect of rotational electric field on viability of the oocyte growth has not been determined in this thesis. Since, this would require one to die the oocyte and determine the rotational effects. Nonetheless, under controlled rotation condition of 500 kHz at 10 Vp-p, oocytes are found to be intact after rotation experiments indicating the survival ability of the oocytes.

## 5.5. Summary

In this chapter, the experimental setups used for all tests in subsequent electro-rotation studies are provided, including details of the buffer medium preparation. Materials and methods are presented, including the method to handle and prepare the bovine oocytes. These details and experimental setup are used in chapters 6-7 where the device is experimentally tested and validated. Method used during calculation of angular velocity or the dielectric spectrum of the rotating oocytes in yaw and pitch-axis is explained. Assumptions made during experiments are also presented.

# Chapter 6. Experimental Validation – Yaw Axis Rotation

In this chapter, controlled rotation around the yaw-axis is demonstrated in the fabricated biochip, and the electric field activation frequency range and electrokinetic properties of the bovine oocytes are characterised. Rotation is measured via video image processing. Optimum rotation rates are defined experimentally for yaw axis rotation. Zona intact and zona free oocytes are tested for electrical equivalence to assess the robustness and generality at the biochip and results. Finally, the dielectric properties of the oocytes are fully characterised based on the results.

## 6.1. Experimental analysis

Videos of experiments are captured at 30 Hz for each individual oocyte, and processed manually using the ImageJ V1.46r manual tracking plugin, NIH, USA. Video clips during experiments are captured with $f$=30 Hz sampling frequency for each individual oocyte. These video frames are processed offline manually using the free software ImageJ to estimate the cell rotation rate. The estimation methods for two axes rotation have to be different, because the cell has completely different motion patterns and observable features. In case feature points are hard to determine on the cell, the video files are imported into ImageJ and each frame is further processed (via Image > Adjust > brightness/contract> auto; Image > Adjust > Threshold > manual-threshold [136-low and 136-high level threshold]) to determine several pixel points on the circumference of the oocyte. The obtained key points are manually tracked by using the Manual Tracking plug-in tool (via point-selection tool; Plug in > Manual tracking [Time interval-1sec; X/Y calibration-1µm]). A detailed procedure to calculate the rotation measurement is provided (supplementary methods).

In particular, when the cell has an in-plane rotation, it is like a flat disk rotating about its center. Using this observation, we are able to draw a line in each video frame connecting two consistent reference points on the cell, one being the cell center and the other a feature point on the circumference of the cell. The angle between this line and the horizontal line is denoted by $\theta$. The change in $\theta$ between each two successive frames

is denoted by $\partial\theta$, then the rotation rate can be given by $\Omega=\partial\theta/\Delta t$, where $\Delta t$ is the sampling period ($\Delta t=1/f=0.033$ s). In practice, to accommodate the case when $\partial\theta$ is immeasurable, we use the angle change in several successive frames divided by that time period for the rotation rate $\Omega$. When the cell has a rolling rotation, due to its extremely complicated texture, it is impossible to choose a feature point with unique gray-level properties, making the previous method of tracking feature points invalid. To estimate the rotation rate, hereby we assume the cell rolls without any sliding. With this assumption, we measure the distance (denoted by $d$) the cell travels between two successive frames, then the rotation rate can be given by $\Psi=d/(r\cdot\Delta t)$, where $r$ is the cell radius. In practice, similarly to in-plane rotation, to accommodate the case when $d$ is immeasurable, we use the distance in several successive frames divided by that time period for the rotation rate $\Psi$.

The average value for four oocytes is calculated at successive frequencies. Percentile standard error is calculated from the data. Dielectric spectrum plots are obtained by plotting these values versus the applied frequency.

The specific experimental tests include:

- Application of AC voltage to test yaw-axis rotation of bovine oocytes and to characterize the dielectric spectrum with the applied peak to peak voltage (Vp-p) and frequency for this motion.
- Experiments are carried out to characterise and compare the dielectric spectrum of zona-intact and zona-free oocytes. This goal is to determine the electrical equivalency between oocyte membrane and the cytoplasm, which assesses the robustness and generality of the biochip.
- A study is carried out at different w/v ratios of sucrose and dextrose concentration in the deionised medium to check for variation in the rotation rate of bovine oocytes with corresponding medium conductivity. These tests characterise the range of medium solutions that are effective.

The experimental results are designed to specifically quantify the dependency of suspended single bovine oocyte rotation around the yaw-axis due to an applied AC frequency range between 10 kHz to 10MHz. Tests will validate if the bovine oocytes are highly polarizable and check for the presence of MW charge relaxation. Rotation results are verified in the clockwise and anticlockwise direction to evaluate if the rotation can be controllable. Controlled rotation is defined by how quick the oocytes polarize and rotate in the direction of the AC field, and achieved by applying and then halting the applied field to assess to what rotational resolution control can be achieved.

## 6.2. Results and Discussion

Experimental rotation of bovine oocytes is shown in Figure 6.1 and Figure 6.4. Images are obtained from the video files also available as an electronic appendix. Clockwise and anticlockwise rotations are demonstrated in Figure 6.2. From the experiments, oocyte rotations are observed at AC frequencies between 100 kHz and 10 MHz's. Rotation is not observed below 100 kHz and the oocytes internal structures, such as proteins and chromosomes in the cytoplasm start to deteriorate at frequencies above 5-10 MHz. Deterioration indicated that the oocytes die and the cytoplasm materials are expelled out of the membrane due to membrane breakdown. It is found that bovine oocytes significantly rotate and trap at the centre of the ROT chamber, as expected by design, at 500 kHz AC frequency. This result is shown in Figure 6.3.

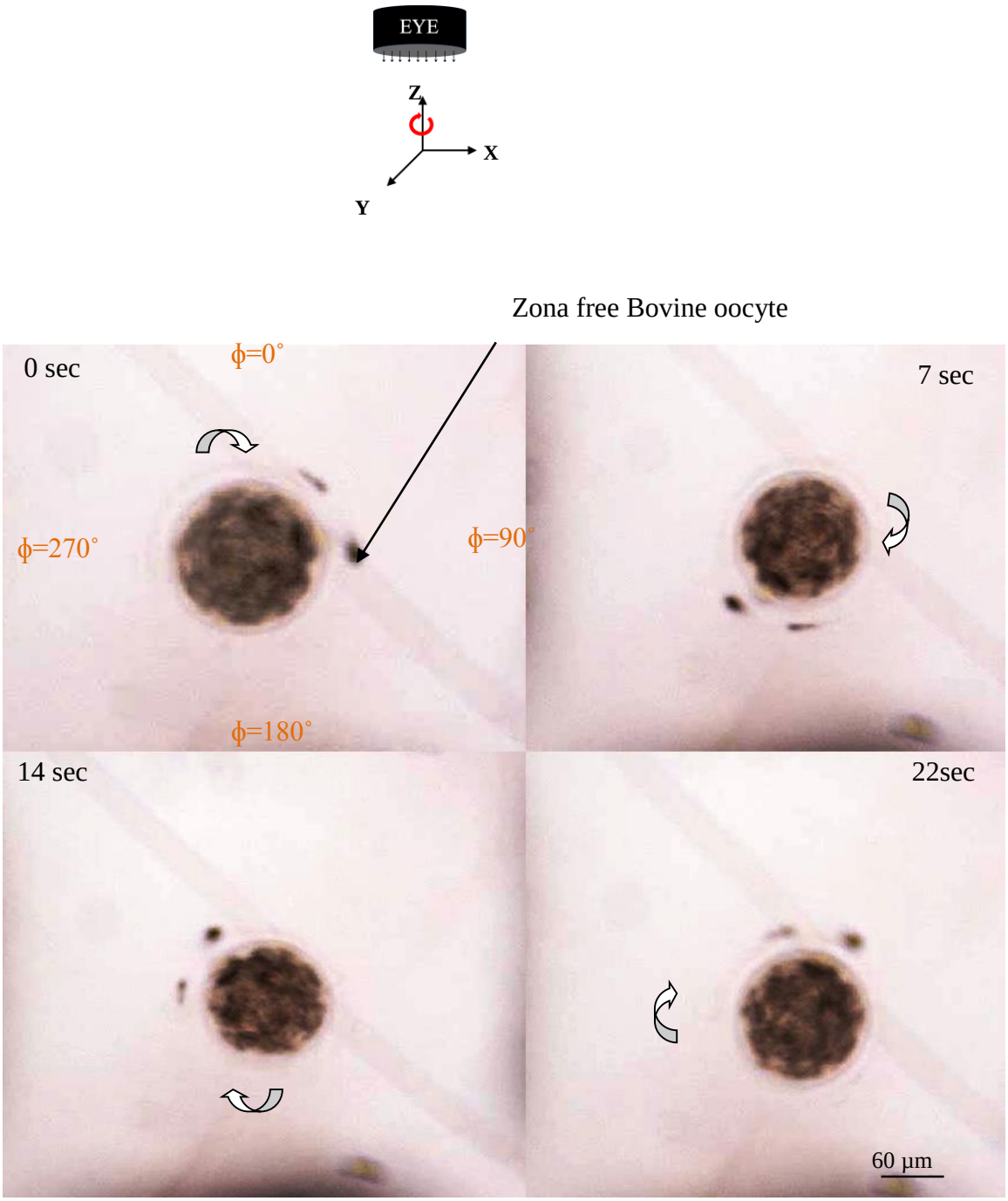


***Figure 6.1:*** *Experimental results of bovine oocyte rotation: A single bovine oocyte undergoing yaw axis rotation at 10 Vp-p, 500 kHz frequency and 90° phase shift between two pairs of orthogonally arranged vertical electrodes. Arrow shows rotation direction of oocyte [41]. (SI: video 1)*

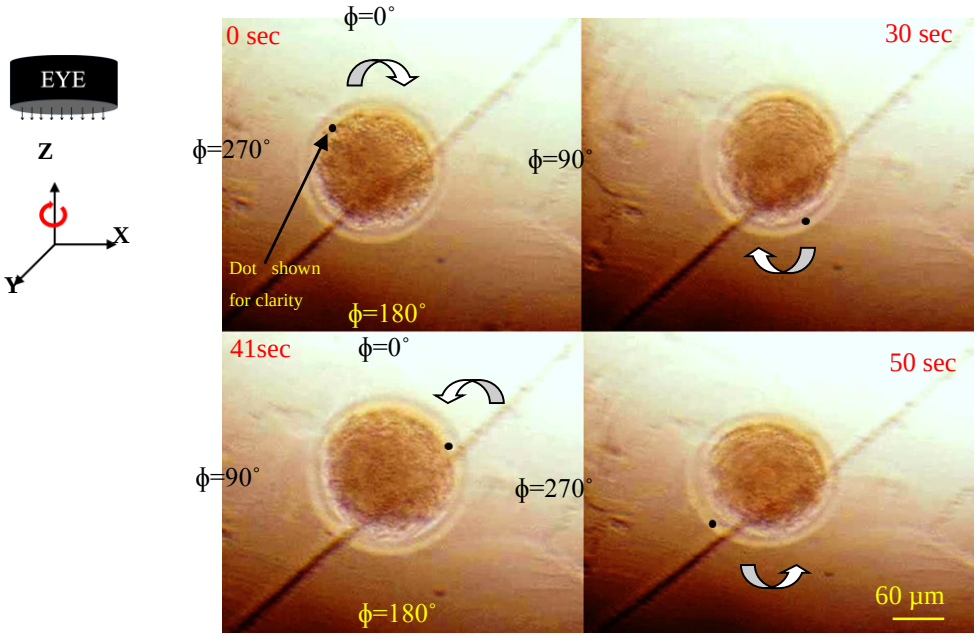


***Figure 6.2:*** *Experimental results of bovine oocyte rotation: Bovine oocyte rotating in clockwise and anticlockwise directions to show that cell is rotating in DEP torque. (c). Precise rotation control of oocyte and about 5-10˚ angular rotation can be easily controlled by controlling the phase shifts at the electrodes[41]. (SI: video 2)*

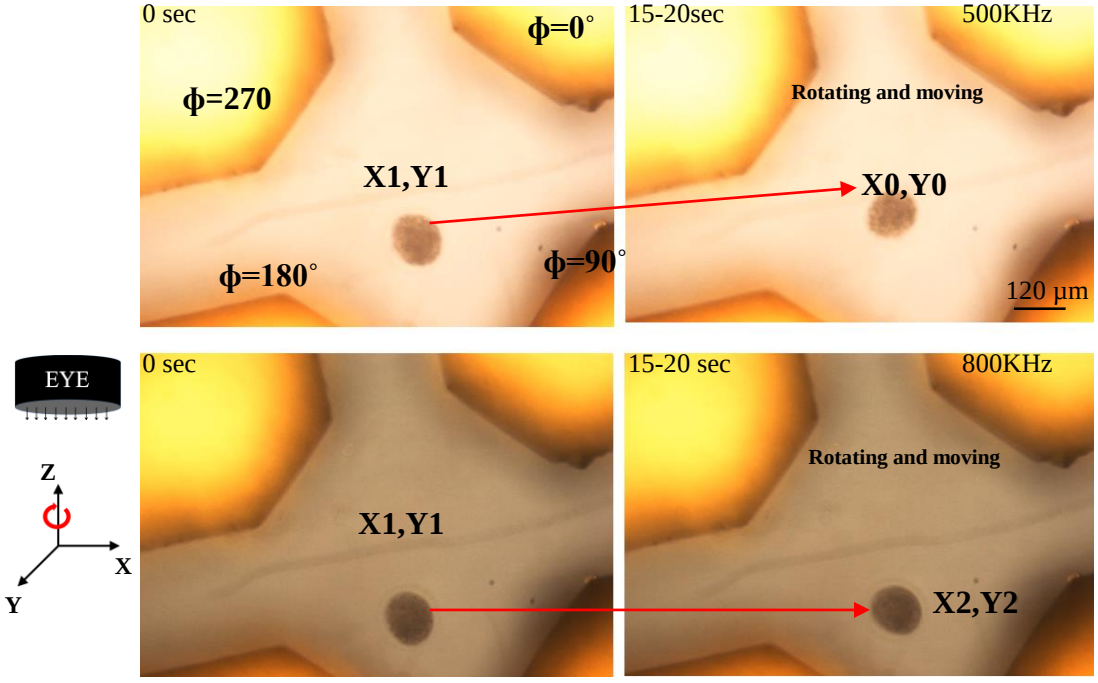


***Figure 6.3:*** *Experimental results of bovine oocyte rotation: Bovine oocyte rotates and traps at the centre of the rotation chamber at 10 Vp-p and 500 KHz AC frequency as compared to the rest of frequency zones. (X0, Y0) is the centre of the rotation chamber. (SI: video 3)*

Moreover, due to the rotation of oocytes in one constant direction regardless of the applied field frequency, amplitude and phase, bovine oocytes are thus shown to be more polarizable than the medium. Due to this finding, it is now possible to control the rate of rotation of the bovine oocytes. Figure 6.4, shows rotation with precision control by the application of start-stop AC voltage to the electrodes. Oocytes are rotated ~0.57-5 degrees in each time frame, which is suitable to specifically orient the oocyte in a desired position for enucleation. Angular rotation of the order of 0.57 degree is found to be the minimal showing precision rotation control. Supplementary video provides detailed evidence of this controlled rotation. Finally, the rotation rate increased with increasing frequency with no MW relaxation [148, 149, 153, 173]. Hence, only one peak in the angular velocity spectrum is expected.

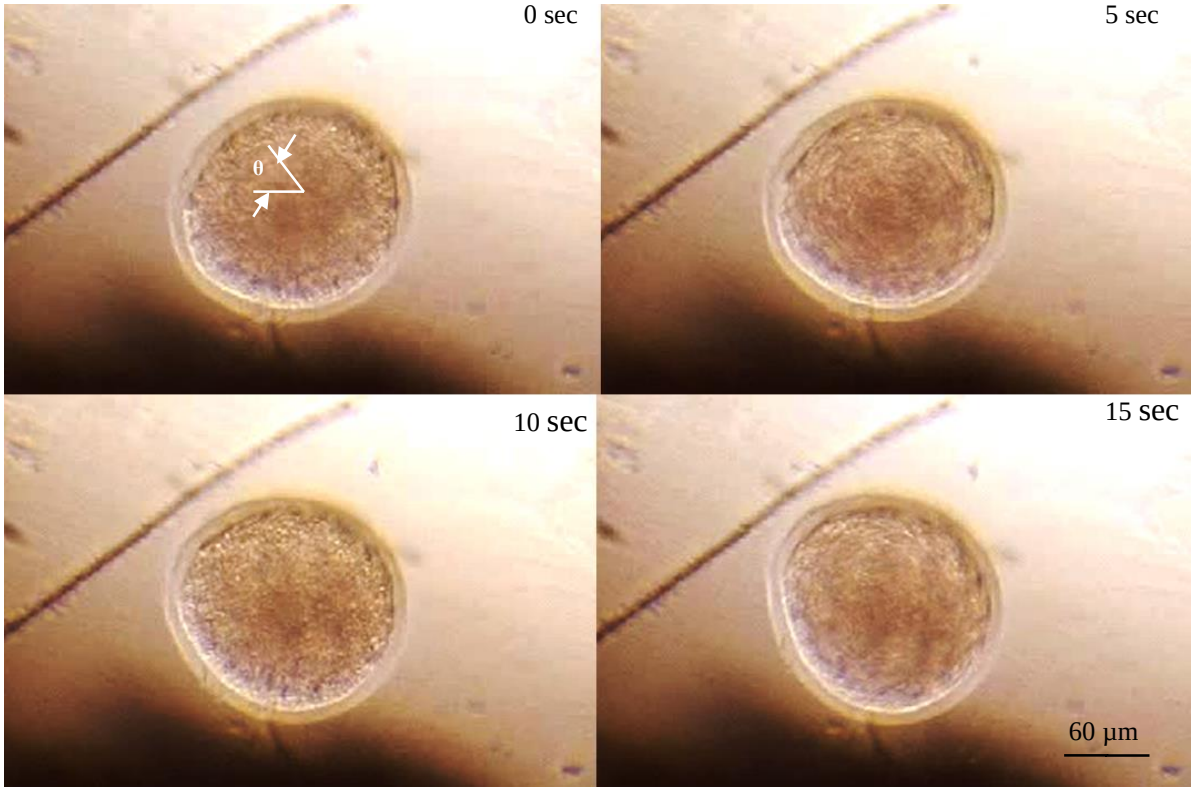


***Figure 6.4:*** *Precise rotation control of oocyte and about 5-10˚ angular rotation can be easily controlled by controlling the phase shifts at the electrodes. (SI: video 4)*

### 6.2.1. Effect of changes in AC amplitude

Experimental results to assess the dependence of bovine oocyte rotation on at 10 Vp-p and 20 Vp-p, is shown in Figure 6.5. The rotation rate increases with the increase in AC amplitude and frequency.

However, for 20 Vp-p amplitude, the suitable operable frequency range is found to be between 100 kHz-1MHz. Above AC frequency of 1MHz, the oocyte lyses takes place. A controlled rotation and rotation rate is observed with inputs of 100 kHz for 20 Vp-p and 500 kHz for 10V.

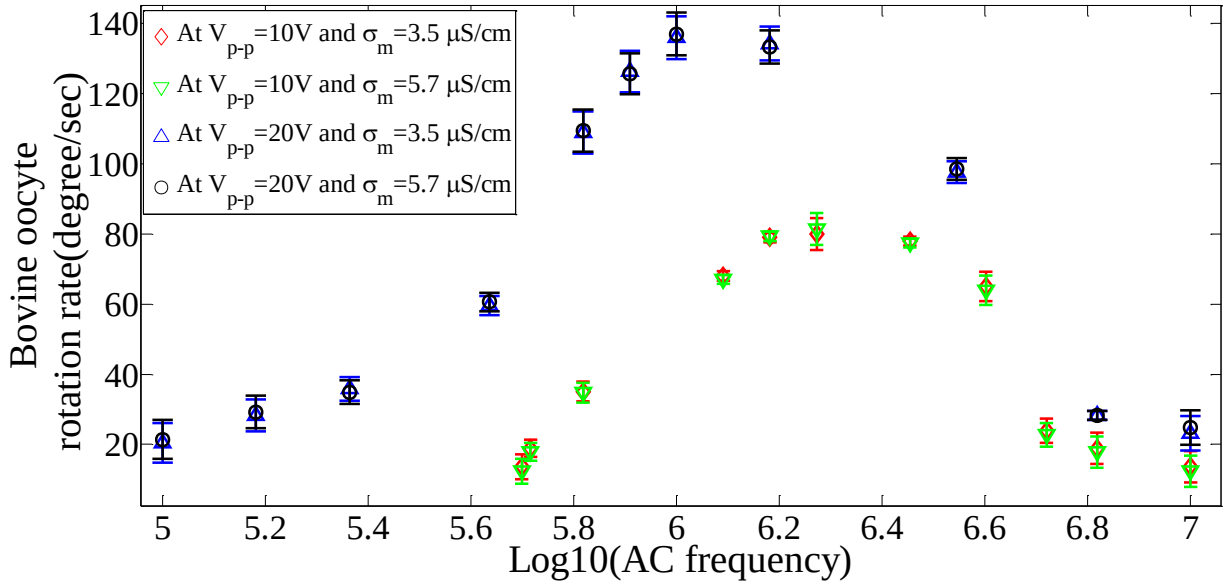


***Figure 6.5:*** Bovine oocyte in-plane rotation rate in relation to the conductivity ($\sigma_m$) of buffer medium and the applied AC power supply (frequency and amplitude Vp-p) in experiment. Used, 4 oocytes× 3 replicas (n=3, N=4) with n-no of biological or technical replicates and N-no of samples.

### 6.2.2. Effect of change in medium conductivity

Although there is no difference observed from Figure 6.5 regarding a change in media conductivity, additional experimental work identified that increasing conductivity does slightly increase the rotation rate, which can be observed from Figure 6.6. For example, at 10 Vp-p, the difference between rotation rates is 10 degree/sec between $\sigma_m$ at 3.5 and

11.3 µS/cm. It should be noted that when the medium conductivity is higher, it becomes less viscous, making it harder to suspend the oocyte. In contrast, when the medium conductivity is lower, it becomes more viscous, making it more difficult to transfer oocytes.

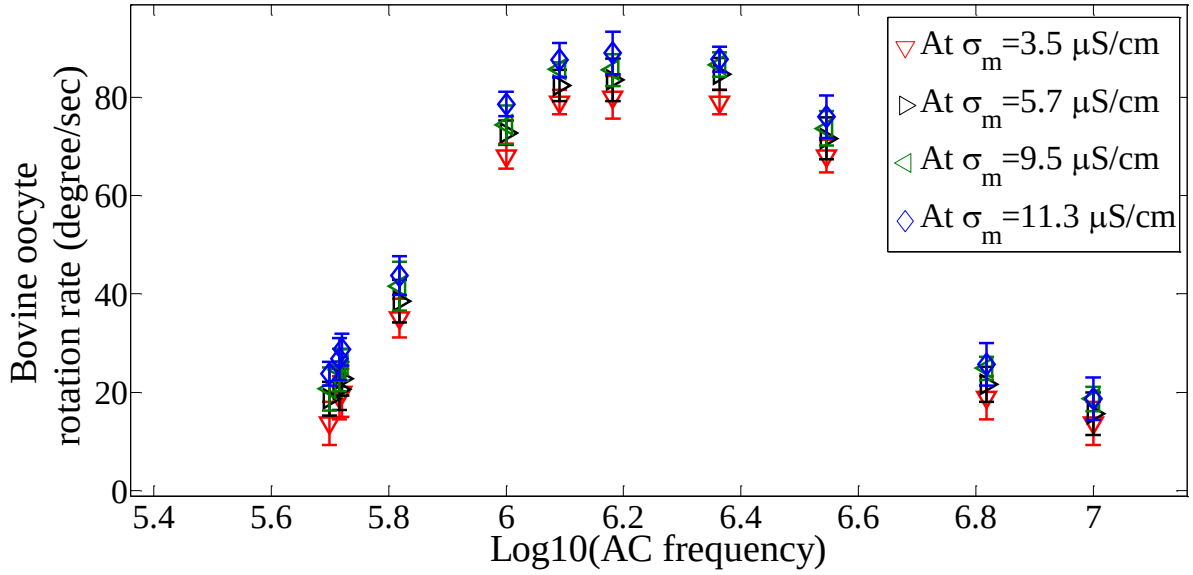


***Figure 6.6:*** Bovine oocyte in-plane rotation rate in relation to the conductivity ($\sigma_m$) of buffer medium and the applied AC power frequency in experiment. Here AC amplitude is fixed at 10 Vp-p. Used, 4 oocytes× 3 replicas (n=3, N=4) with n (no of biological or technical replicates) and N (no of samples).

Standard deviation error bars are represented to show the difference in error while calculating the rotation spectra. Relative standard deviation (RSTD) error of less than 1% is obtained from the calculation and shows the accuracy of measurement of rotation rate.

Three to four oocytes are considered to determine the rotation spectra and rotation rate is calculated at different medium conductivity. RSTD is calculated by the following formula:

$$\%RSTD = \frac{STD}{Mean} \times 100 \qquad (6.1)$$

Statistical analysis using a t-test for different data groups in Microsoft Excel 2010 revealed that increasing conductivity has negligible effect on the rotation rate (see Figure 6.7). In particular,

12 data points are analysed for each applied AC frequency at 10 Vp-p at different buffer medium conductivity ($\sigma_m$). Results showed p-value of $p > 0.4$ for all cases, indicating that buffer medium conductivity has no statistically significant effect on the rotation rate of bovine oocytes in these tests. It should be noted that when the medium conductivity is higher, it becomes less viscous, making it harder to suspend the oocyte. In contrast, when the medium conductivity is lower, it becomes more viscous, making it more difficult to transfer oocytes.

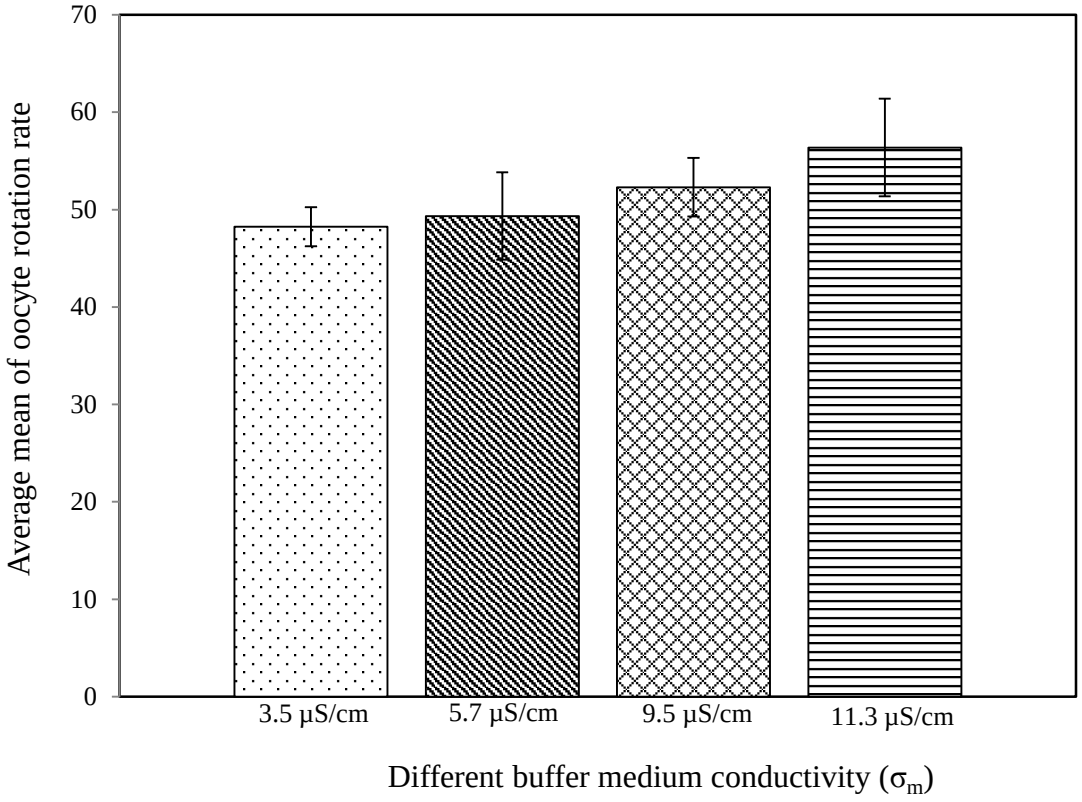


***Figure 6.7:*** *Effect of medium conductivity (σm) on rotation rate (mean rotation rate ±5% standard deviation (SD)) of bovine oocytes. Means with letters in along with A indicate no significant difference. t-test for 22 degree of freedom (df), (p<0.05), and two-sample with equal variance test used.*

## 6.2.3. Effect of zona pellucida

Bovine oocytes with zona pellucida had slower rotation rates compared to zona free oocyte, all else equal. However, the difference between rotation rates is negligible, as shown in Figure 6.8. Removal of zona pellucida does not substantially reduce the size and weight of the oocyte,

from Equation *(2.15*), it can be deduced that the rotation torque remains the same. Therefore, the dielectric property of the zona-free oocyte is almost equivalent to the zona-intact oocyte, indicating an electrical equivalency between the cytoplasm and its surrounding zona pellucida. At 10 Vp-p amplitude and 500 kHz AC sinusoidal frequency, controlled rotation of oocytes is possible with and without zona. Controlled rotation is determined by the degree at which the rotation can be started and stopped by the application of rotational field.

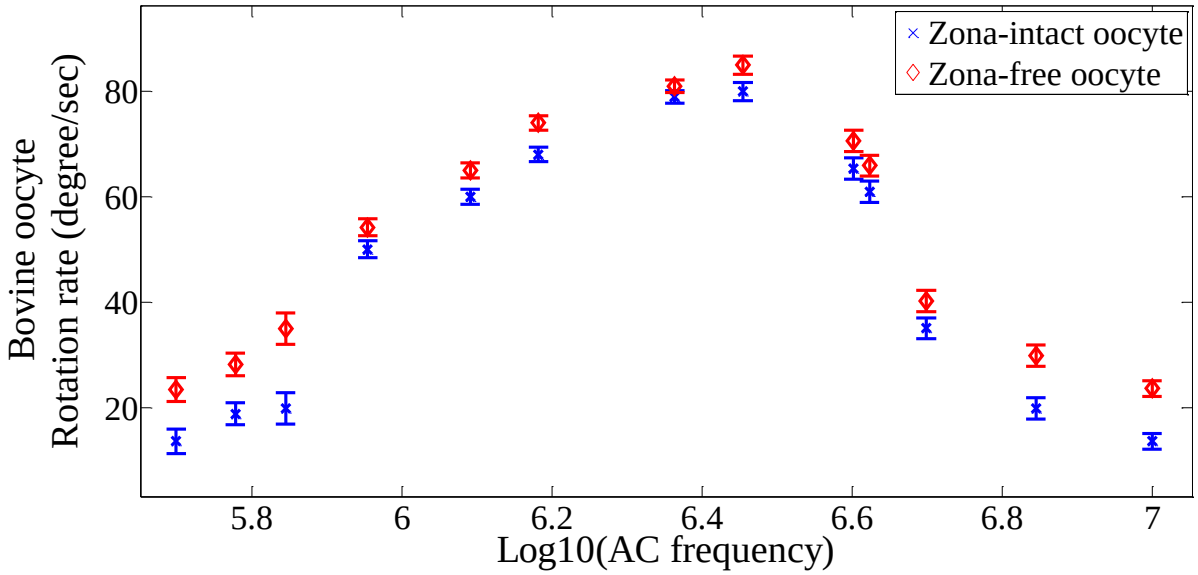


***Figure 6.8:*** *Comparison of the in-plane rotation rate for ZP-intact and ZP-free bovine oocytes. Here the AC amplitude is fixed at 10 Vp-p. N=13 (N- number of biological replicates used for this plot). Used, 4 oocytes× 3 replicas (n=3, N=4) with n (no of biological or technical replicates) and N (no of samples). Medium conductivity used is* $\sigma_m$*=3.9 µS/cm.*

Basically, there are few key findings from yaw-rotation study:

- The rotation rate versus frequency curve is like a band-pass filter. On two ends, the oocyte does not rotate at all; in the middle, the oocyte rotates first faster as the frequency increases and then slower down as the frequency increases further – like a Gaussian graph. There exists one and only one peak rotation rate (160 degree/s for AC amplitude 20 Vp-p and 90 degree/s for 10 Vp-p) in the frequency axis.

- Higher AC amplitude results in a faster rotation, which is evident if comparing the data points for 10 Vp-p and 20 Vp-p. The latter voltage led to nearly 1.5 times increase in rotation rate.
- Applied with higher AC amplitude, the rotation rate increases to its peak at a lower AC frequency. This can be evident if we analyse the data points for 10 Vp-p and 20 Vp-p again. The latter voltage made the peak rotation rate occur at a lower AC frequency by nearly one order.
- Higher medium conductivity results in a higher rotation rate, which can be reflected by the data points for 3.5 μS/cm and 5.7 μS/cm, as referenced from Figure 6.5-6.8. Consistent with the theoretical analysis and findings in literature [148, 172, 187], these findings are valuable for guiding the design of control scheme of cell rotations in various applications.
- Zona-free and zona-intact oocytes showed electrical equivalency. This key observation will enhance the understanding of characteristic and behaviour of bovine oocytes.

## 6.3. Summary

Controlled rotation around multiple axes of bovine oocytes is achieved in a micro-device/biochip fabricated using a mixture of conventional photolithography and micro-milling processes. The oocytes are found to be highly polarizable. Optimum rotation rates at which one can control the rotation of oocytes for enucleation are empirically found for inputs of 10 Vp-p and 500 kHz AC frequency for yaw-axis rotation, and 10-20 Vp-p and 10 kHz-100 kHz AC frequency for pitch-axis rotation. Controlled rotation of the oocyte in both the clockwise and anticlockwise direction is achieved. Further dielectric spectrum results for the zona intact oocytes and zona free oocytes showed electric equivalence. Characterization of cell rotation also provides vital information about the dielectric properties of bovine oocytes to enable their non-contact manipulation using DEP torque. Finally the biochip presented is a useful, low-cost tool for rotating cells in a controlled fashion in 3D spaces. The materials in the fabricated biochip are biocompatible, except brass, which may induce toxic effects on cells. This effect can be avoided by micro-milling different biocompatible materials such as titanium, gold and aluminium.

# Chapter 7. Experimental Validation – Pitch Axis Rotation

In this chapter, rotation of bovine oocyte around the pitch-axis is demonstrated in the fabricated biochip, and the electric field activation frequency range during pitch rotation is determined. Behaviour of bovine oocytes during pitch rotation is analysed along with varying medium permittivity parameter. Optimum rotation rates are experimentally determined for pitch-axis rotation.

## 7.1. Experimental analysis

During pitch-axis rotation of oocyte, rolling occurs. Because of rolling, referencing a major pixel line to assess rotation is not considered. Instead the oocyte center as a pixel point is referenced and the number of revolutions made in degrees per second by the pixel point is estimated manually from video measurements.

Similar to yaw-axis rotation, the angular velocity of oocyte rotation is calculated by the mean value of three to four oocytes at successive frequencies. Percent standard error is calculated by dividing the standard deviation by the mean value. Dielectric spectrum plots are obtained by plotting these mean value data points with respect to the applied AC frequency input.

The specific experimental tests during pitch-axis rotation experiment include:

- Experiments are carried out to characterise and compare the dielectric spectrum of bovine oocytes in pitch-axis. This test is the first time in which, pitch rotation process is characterized using DEP.
- Different combination of rotation field activation on the electrodes are employed, as shown in Figure 7.1 during pitch- axis rotation tests, and are tested to assess the validity of the biochip and its ability to manipulate cells.
- A study is carried out at different w/v ratios of sucrose and dextrose concentration in the deionised medium to check for variation in the rotation rate of bovine oocytes as a

function of surrounding medium conductivity. These tests characterise the range of medium solutions that are effective.

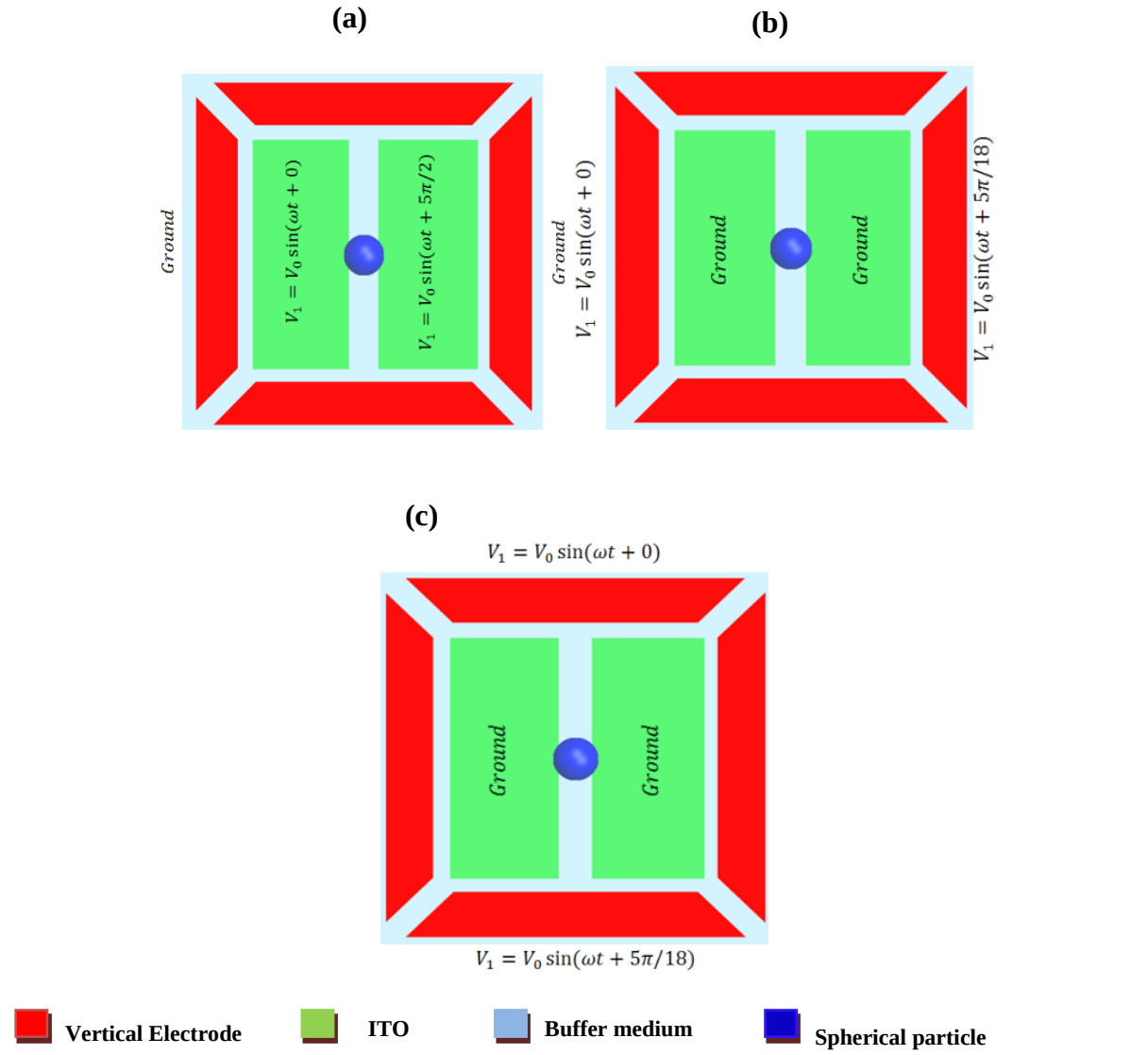


***Figure 7.1:*** *Concept of pitch-axis rotation in the designed biochip. (a) Concept-1: to obtain pitch axis rotation along x-plane, (b) Concept-2: to obtain pitch axis rotation along y-plane. (c) Concept-3 to obtain pitch axis rotation along y-plane with other ends of vertical electrodes applied with AC.*

The experimental results are designed to specifically quantify the dependency of suspended single bovine oocyte rotation around the pitch-axis due to an applied AC frequency range between 10 kHz to 10MHz. Tests will also validate if the bovine oocytes are able to polarize with the application of pitch rotation concepts. Finally they are used to define and characterize the electrokinetic properties of these cells.

## 7.2. Results and Discussion

Experimental pitch axis rotation of bovine oocytes is shown in Figure 7.2 and supplemental video. The concept from Figure 7.1a is used to obtain these initial rotation results. In comparison to yaw-axis rotation, bovine oocytes rotated around the pitch axis with an input of 10-20 Vp-p amplitude and 10 kHz-100 kHz. At 10 Vp-p amplitude the pitch rotation is steady within the specified frequency. At 10 Vp-p, the pitch-axis rotation was very gentle and at or above 15 Vp-p, the rotation was more significant with a faster rate. Due to the faster rotation along with rolling, the oocyte moves away from the ROT chamber.

Even though rotation in pitch is evident, rolling also occurs unless the oocytes are perfectly suspended in the medium above the bottom ITO electrode. Rolling motion of the oocyte can be attributed to the frictional or drag force on the interface between oocyte and the bottom substrate. Hence, suspension of oocytes in a perfect isotonic solution is necessary to obtain steady pitch axis rotation.

Note that the pitch axis rotation had a different pattern than the yaw-axis in-situ rotation in that the cell rolled over like a wheel on the run. Due to the lack of unique feature points on the rolling oocyte, the rotation pattern shown in Figure 7.2, from a top view, looks as if the oocyte moved toward the gap between the two bottom electrodes. However, the time-varying textures of the oocyte indicate its rotation, which can be better seen from the attached video clip available as an online appendix.

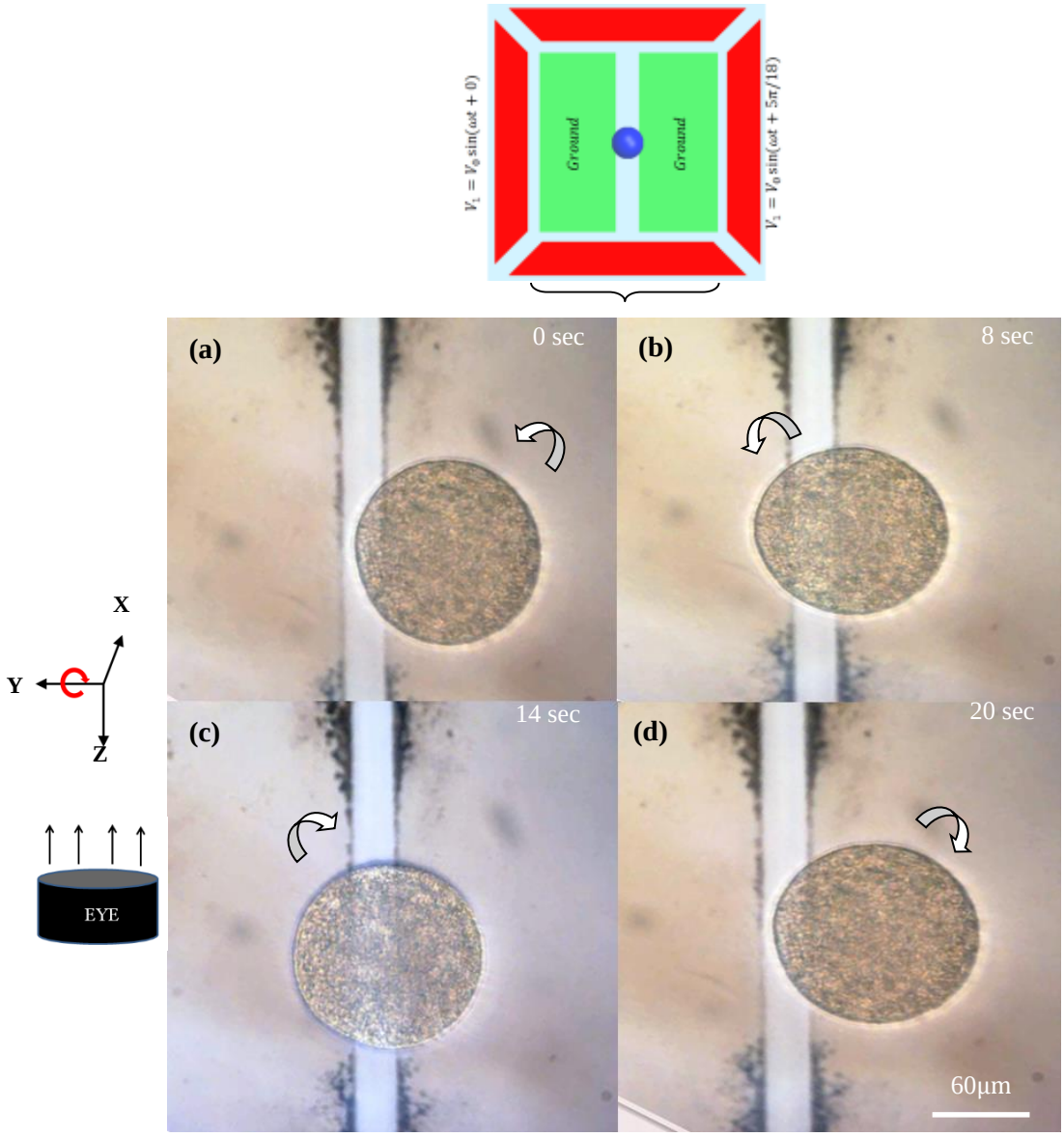


***Figure 7.2:*** *Experimental results. (a-d). Co-ordinate system along with a single oocyte undergoing pitch axis rotation at 10 Vp-p, 80 kHz frequency and 50° phase shift between two bottom electrodes and grounded vertical electrodes. Arrow shows the rotation direction of oocyte rotation [41]. (SI: video 5)*

Figure 7.3, shows the proof of the pitch rotation concept adapted and modified from Figure 7.1a. Images are obtained from the video files available as an appendix. Bottom ITO electrodes are subjected to an AC of 10 Vp-p and 80 kHz frequency input along with 50° phase shift, and the two vertical electrodes are grounded. Simulation of DEP fields in the biochip with 50˚ phase shift resulted into increased amounts of uniform rotational fields with constant magnitude within the region enclosed above the bottom ITO electrodes, as compared to 90˚

shifts. This is the main reason to employ 50˚ rather than 90˚ during experiments. Phase shift of 50° during pitch rotation is also shown from previous simulations using optoelectronic tweezers [19, 188]. Rotation in pitch along with rolling is evident for both the two oocytes at the centre of ROT chamber. From the experimental results, it is found that any two vertical walls can be made ground along with bottom electrodes with alternating current. Further rotation can be obtained by providing an AC input to the vertical electrodes and grounding the ITO electrodes. Thus, the biochip provides flexibility in generating required 3D fields.

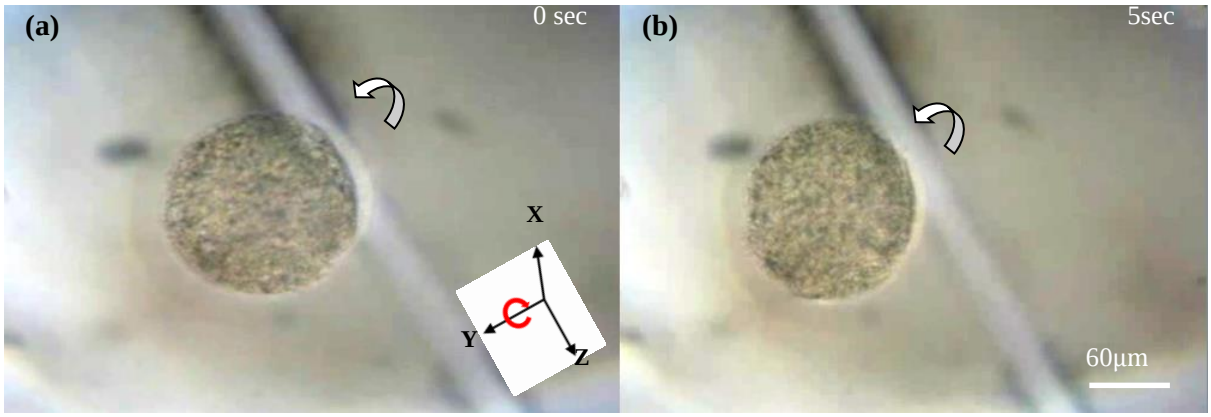


***Figure 7.3:*** *Experimental results. (a-b). Co-ordinate system along with a single oocyte undergoing pitch axis rotation at 10 Vp-p, 60 kHz frequency and 50° phase shift between two bottom electrodes and grounded vertical electrodes. Arrow shows the rotation direction of oocyte rotation. (SI: video 5)*

Thus, the biochip can obtain pitch axis rotation via a variety of actuation strategies over the electrodes. Figure 7.4, shows the case where bottom electrodes are grounded and vertical side wall electrodes are subjected to AC field with 50˚ phase shift. Referring to the concept shown in Figure 7.1b, rotation around the pitch-axis is obtained by activating two opposite vertical wall electrodes and grounding the bottom ITO electrodes. Both co-field and anti-co-field rotation in pitch is obtained with a degree of rotation control at sinusoidal 10Vp-p amplitude and 40 kHz AC frequency.

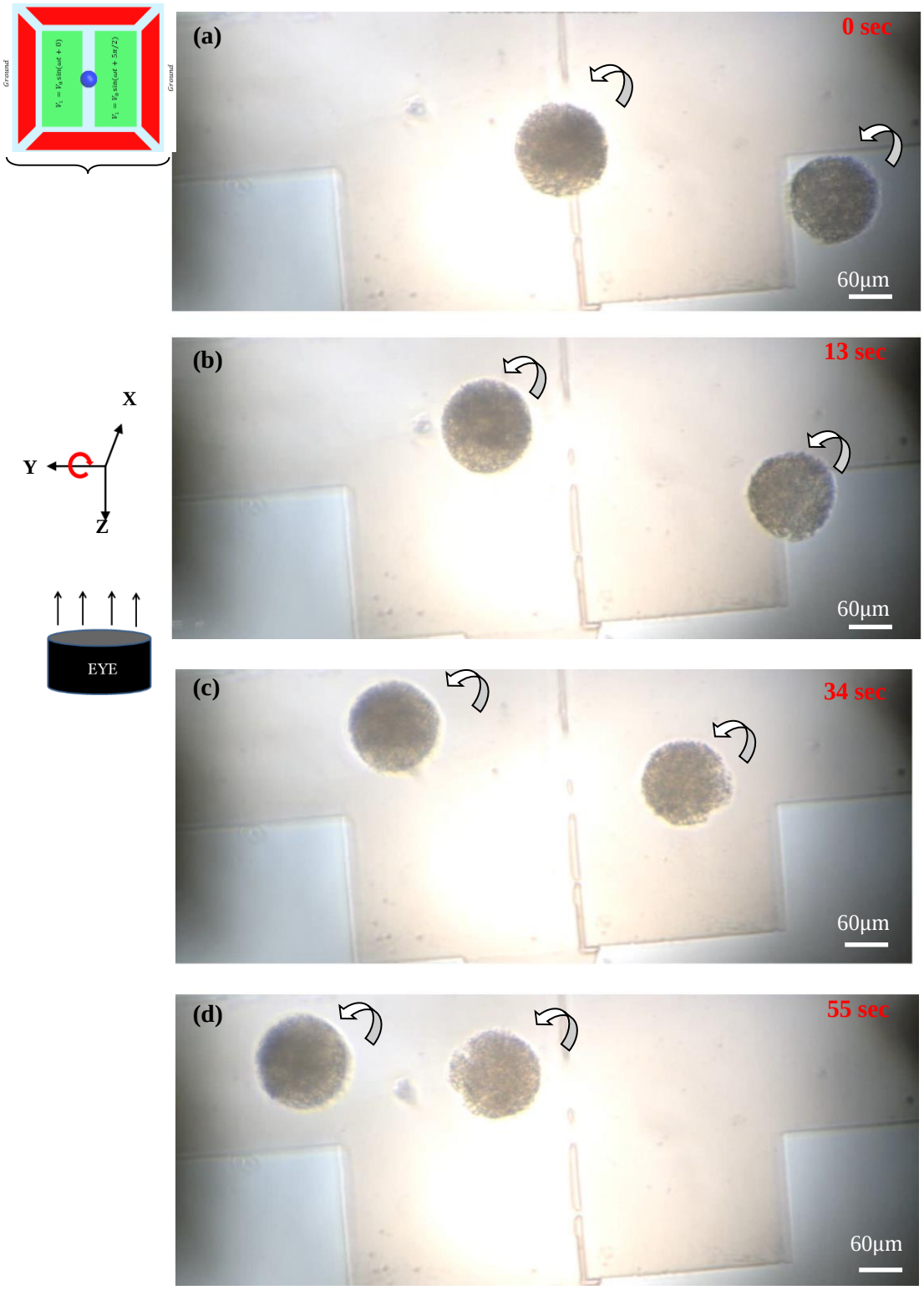


***Figure 7.4:*** *Experimental results. (a-d). Co-ordinate system along with a two oocyte undergoing pitch axis rotation at 10 Vp-p, 80 kHz frequency and 50° phase shift between two bottom electrodes and grounded vertical electrodes. Arrow shows the rotation direction of oocyte rotation. (SI: video 6)*

Clockwise and anticlockwise rotation in pitch is also demonstrated in Figure 7.5, by using concept shown in Figure 7.1c. The oocyte is made to rotate in pitch with AC amplitude of 10 Vp-p and frequency of 40 kHz. From the experiments, it is also worth noticing the behaviour of bovine oocytes shown in Figure 7.6. Whenever the oocyte nears the vertical electrodes, the higher concentration of DEP force near the electrode pulls the oocyte towards the electrode. As the oocyte nears the electrodes, lyses starts and slowly deteriorates the thin membrane. However, as soon as the AC signals are stopped or the phase of the AC input is switched, the oocyte regains its shape. Videos provided as an online appendix to document this behaviour in the supplemental appendix.

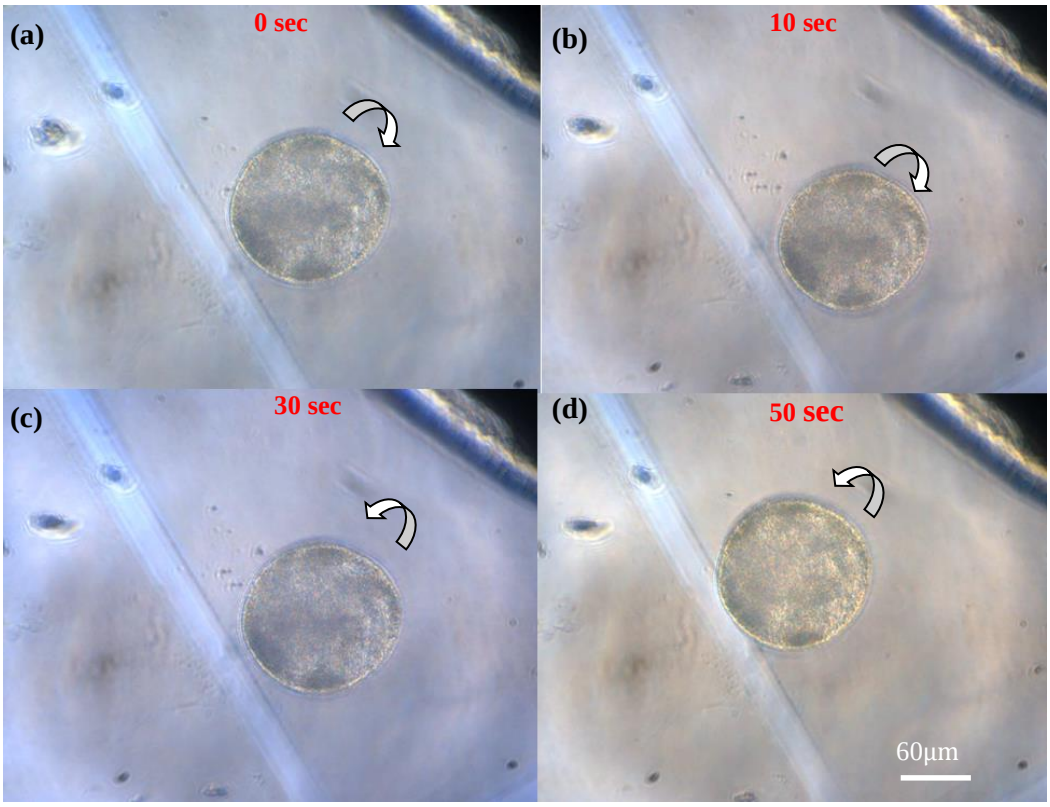


***Figure 7.5:*** *Experimental results. (a-d). Co-ordinate system along with a single oocyte undergoing pitch axis rotation at 10 Vp-p, 80 kHz frequency and 50° phase shift between two vertical electrodes and grounded bottom. Arrow shows the rotation direction of oocyte rotation. (SI: video 7)*

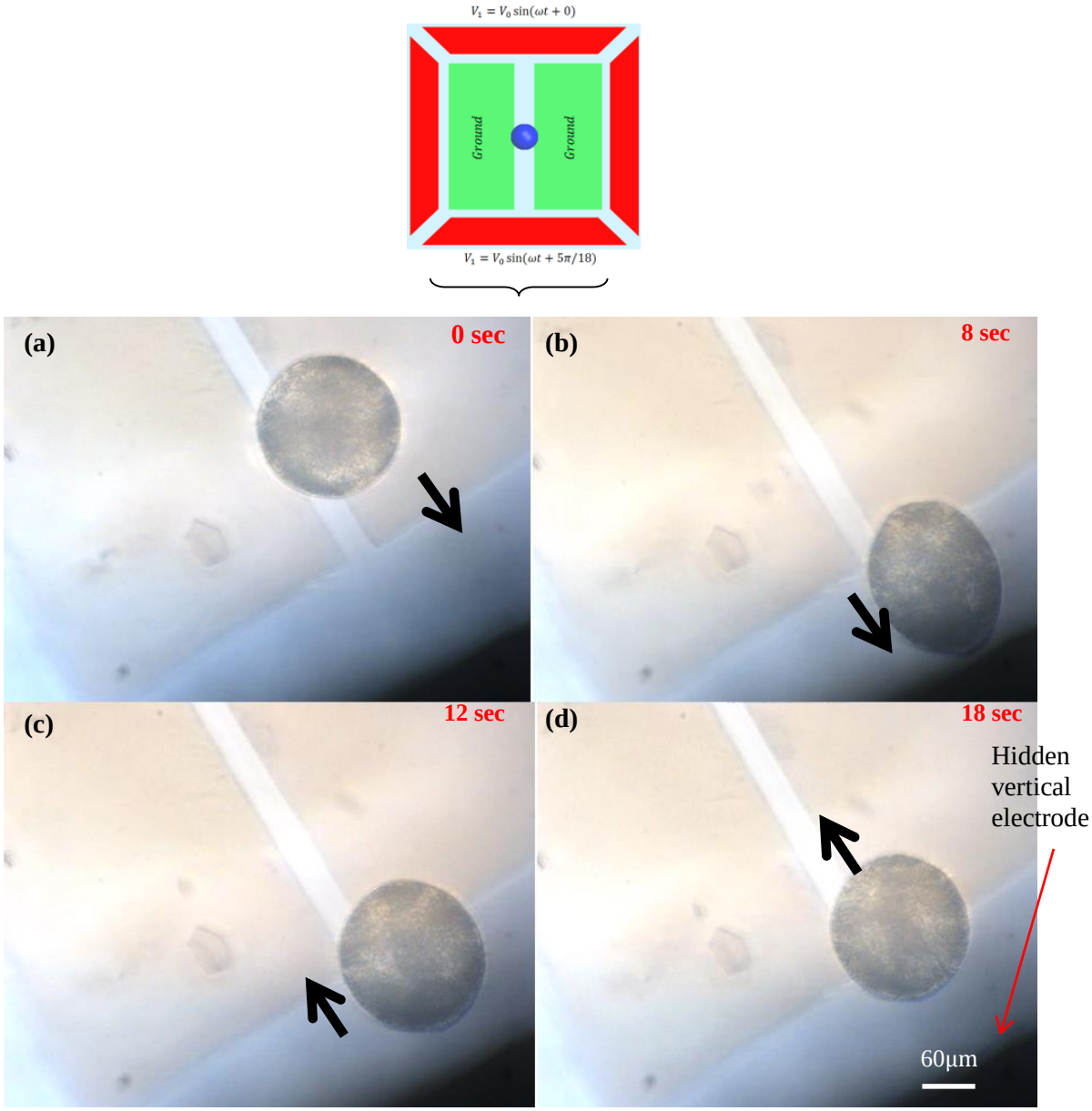


***Figure 7.6:*** *Experimental results. (a-d). Co-ordinate system along with a single oocyte undergoing lysis, when near to the vertical electrode. Arrow shows the direction of oocyte movement. This phenomenon can be used to determine the stress, strain and elastic effect on the oocytes. (SI: video 8)*

### 7.2.1. Pitch axis rotation spectrum of bovine oocytes

Dielectric spectrum plots for pitch axis rotation are shown in Figure 7.7. Compared to the yaw-axis rotation rate, the pitch-axis rotation rate is higher between 40-80 kHz. Rotation rate

increases with the increasing frequency and conductivity of the medium. At frequencies above 100 kHz the rotation rate decreases. Frequencies above 150 kHz resulted in no rotation.

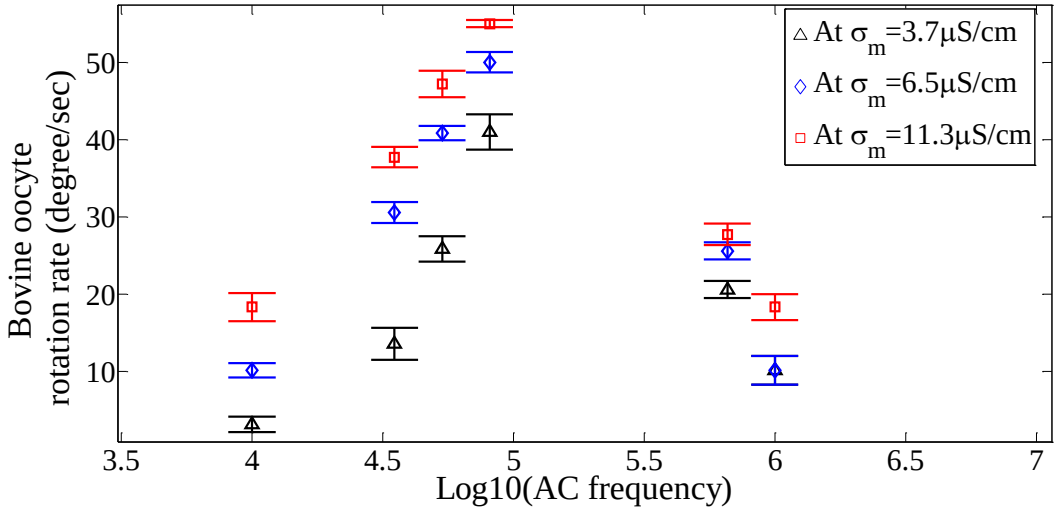


***Figure 7.7:*** *Bovine oocyte rolling rotation rate in relation to the conductivity of buffer medium and the applied frequency in experiment. Here AC amplitude is fixed at 10 Vp-p. Used, 4 oocytes× 3 replicas (n=3, N=4) with n (no of biological or technical replicates) and N (no of samples).*

There was no essential difference observed between pitch-axis rotation and yaw-axis rotation in the AC amplitude effects. In other words, higher input AC amplitude causes faster rotation and cell disintegration at certain frequency (below 10 kHz and above 5 MHz). In particular, higher the conductivity, greater is the rotation rate. The noticeable difference lies in the frequency range in which the rotation occurs, which is attributed to the different local electric field magnitude generated by the two configurations of electrodes for yaw-axis and pitch-axis rotation, respectively.

Overall, a summary of key findings from this pitch-rotation study includes:

- Application of AC fields in the biochip is efficient and flexible. Both bottom ITO electrodes and vertical electrodes can be switched with AC voltage intermittently to obtain the desired particle rotation in both yaw and pitch.
- The pitch-axis rotation spectrum is similar to that for yaw-axis in Chapter 6. However, the maximum rotation is 50-60 degrees/sec, as compared to 160 degrees/sec for yaw-

axis rotation. The range of frequency within which the oocyte rotates in pitch is between 10-100 kHz, whereas, for yaw it is between 100 kHz-10 MHz at the equivalent AC amplitude of 10 Vp-p.

- Higher medium conductivity results in a higher rotation rate, which can be reflected by the data points for 3.7 μS/cm and 11.3 μS/cm, as referenced from Figure 7.2-7.7.

These findings are new to the field of DEP induced particle rotation. They are also valuable for guiding the design of control schemes for cell rotation in a range of potential applications.

## 7.3. Summary

In this chapter, rotation around the pitch-axis of bovine oocytes is demonstrated using the micro-device/biochip fabricated. The oocytes are found to be highly polarizable around the pitch-axis, as for the yaw-axis in Chapter 6. Optimum rotation rates at which one can control the rotation of oocytes for enucleation are empirically found for inputs 10 Vp-p and 10 kHz-100 kHz AC frequency. Dielectric spectrum analysis shows significant similarity to the results for yaw-axis rotation. Characterization of cell rotation also provides vital information about the dielectric properties of bovine oocytes to enable their non-contact manipulation using DEP methods. Finally, the biochip presented is a useful, low-cost tool for rotating cells in a controlled fashion around both the yaw and pitch axes, and could be used to achieve these rotations simultaneously.

# Chapter 8. Experimental Validation – DEP Torque Calculation

In this chapter, experimental DEP torque on the bovine oocyte is validated with numerical computation comparing the resulting angular velocity of the cell in simulation and experimentally. Experimental rotation spectra obtained from the yaw and pitch rotation are used to validate the numerical model derived from a solid shell model [152]. The main goal of this chapter is to verify, whether bovine oocytes can be considered as solid shell or solid spherical object. A validated model also provides a suitable means to better analyse and optimize the biochip design and characterize bovine oocyte dielectric properties for simulation and application.

## 8.1. DEP Torque and dielectric spectrum

The theoretical aspects of DEP torque on a spherical particle are well established. Briefly, an electric field induces image charges at the interfaces between a liquid and a suspended body of different dielectric properties. If the field rotates, these charges travel synchronously, but lag due to charge relaxation in the body and surrounding medium. The permanent angular displacement between the rotating field vector and the image charges leads to a torque on the body that induces rotation. The torque is largest when the angular frequency ($\omega$) is close to the reciprocal of the dominant charge relaxation time ($\tau$). The torque causes the body to rotate, but, due to the viscous drag of the surrounding solution, the rotation speed is much less (typically 10-2 to 10-6) than that of the field.

Cells can be driven either with or against the direction of the field rotation denoted co-field and anti-field rotation [152, 185]. The direction of spin depends upon the polarizability of the cell relative to the surrounding medium. The various components of living cells have different dielectric properties. Several charge relaxation processes are superimposed and each may dominate at a different frequency of the externally applied field.

Cell rotation is more complex than that of homogenous, isotropic, dielectric particles. However, living cells can be characterised by the use of rotating fields. The angular velocity

or dielectric spectrum of the cell is measured at various frequencies of the driving field to yield a rotation spectrum. The complexity of the spectrum increases with the number of the cell components and dielectrically distinct layers. Parameters, such as conductivity and permittivity, can be obtained by modelling experimentally obtained spectra.

During rotation, both the nature of the polarization process and the frequency of the field are significant. The significance of these factors are determined by rotation spectra and are classified into frequency ranges, such as $\alpha, \beta,$ and $\gamma$ as idealised in Figure 8.1 [189, 190]. Polarization in the $\boldsymbol{\alpha}$ range is attributed to displacement of surface charges in low frequency zones. Living cells show two, well separated peaks in the $\beta$ range of their rotation spectra and occur within the kilohertz and megahertz range of frequencies. Finally, the $\gamma$ dispersion range effects occur within the gigahertz range. All three classifications consist of different charge dispersion processes and differ with applications.

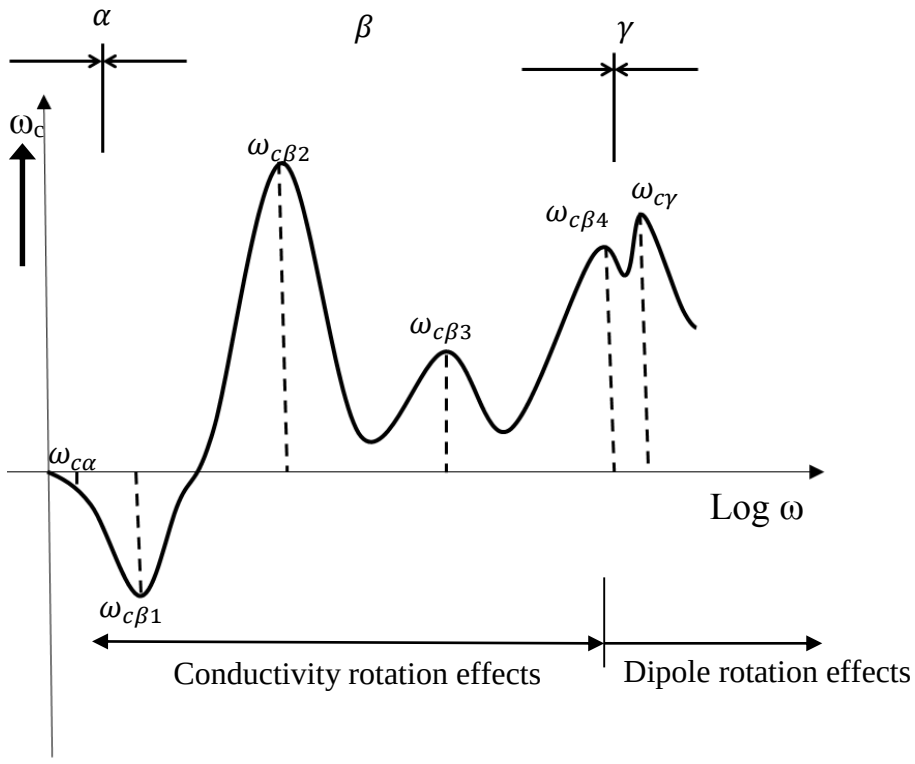


***Figure 8.1:*** *Idealised spectrum of a dielectric particle, demonstrating the frequency dependence and the superposition of rotational effects.* $\omega_c$ *is the angular velocity of the particle* [191]. $\omega_{c\alpha}$ *- angular velocity of particle in lower frequency zone (α) region.* $\omega_{c\beta1}$, $\omega_{c\beta2}$ , $\omega_{c\beta3}$, $\omega_{c\beta4}$ *- angular velocity of particle in kilohertz to megahertz medium frequency zone (β).* $\omega_{c\gamma}$ *- angular velocity of particle in gigahertz frequency zone (γ) region.*

The rotational behaviour of living cells, such as bovine oocytes, must be modelled and calculated if rotation spectra are to be interpreted. Cells are complex structures and broadly consist of a membrane that acts as a dielectric shell enclosing a highly conductive interior. Therefore, the simplest model is a single-shell body.

Additional layers, such as cell wall or other surface structures, necessitate the introduction of one or more extra shells into the model. Multishell bodies are well suited to modelling multilayer cells and are described in detail by Asami et al. [192]. However, cells are also extremely diverse in shape and few can be approximated as spheres. In contrast, analytical solutions to the Laplace-potential equation can only be found for special geometries. Hence, numerical methods are usually required. In this context, bodies with convex/concave surfaces, such as erythrocytes, present particular problems [192]. The range of cell models that have been used for calculating rotating field effects are summarised in Table 8.1.

***Table 8.1:*** *Cell models used for calculation of conductivity Rotation Effects* [191]

| **Cell Models** [190, 192] | **Number of Dielectrics** |
|---|---|
| Isotropic to Multishell sphere | 1….n |
| Isotropic to Multishell cylinder | 1….n |
| Isotropic to Multishell ellipsoid | 1….n |

Since, mammalian eggs, such as bovine oocytes consist of the Zona Pellucida as one external membrane and one internal membrane surrounding cytoplasm, bovine oocytes can be treated as either single layer shell model of solid spherical model. Zona-intact bovine oocytes can be considered as a shell model, and zona-free oocytes can be considered as a solid model.

### 8.1.1. Single Shell model

Electro-kinetic DEP rotation is achieved by applying a suitable torque. The DEP torque equation is well known [149, 184, 190, 191]. To determine the initial DEP torque, the bovine oocytes are considered as a single shell shown in Figure 8.2, yielding:

$$Torque: N = 4\pi\epsilon_o\epsilon_m {R_e}^3 E^2 \,\mathrm{Im[CM]} \tag{8.1}$$

$$\mathrm{Im[CM]} = \left[\left(\frac{C_1}{C_2} - \frac{B_1}{B_2}\right)\left(\frac{\frac{\omega}{\omega_{02}}}{1+\left(\frac{\omega}{\omega_{02}}\right)^2}\right)\right] + \left(\frac{B_1}{B_2} - \frac{A_1}{A_2}\right)\left(\frac{\frac{\omega}{\omega_{01}}}{1+\left(\frac{\omega}{\omega_{01}}\right)^2}\right) \tag{8.2}$$

Where, d is the membrane thickness, $R_e$ is the cell radius, $E$ the external field strength, CM is the Clausius Mossotti [21] factor, $\epsilon_o$ is permittivity of free space, and $\epsilon_m$ is the dielectric constant of the external solution. Table 8.2 contains detailed expressions for A1, A2, B1, B2,$C1, C2, \omega$, $\omega_{01}$, and $\omega_{02}$.

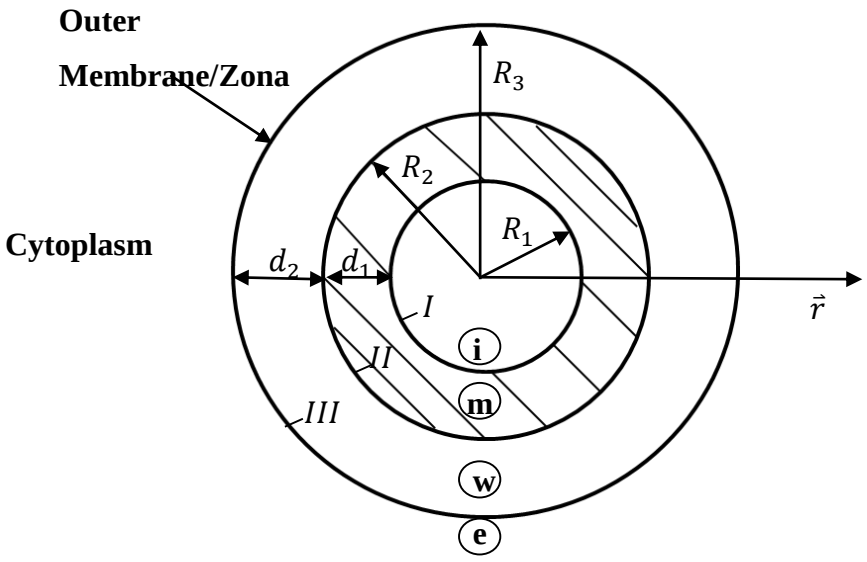


***Figure 8.2:*** *Model of single layer cells; i-inside medium (e.g., cytoplasm) with conductivity ($G_i$) and dielectric constant ($\epsilon_i$); m-membrane system ($G_m, \epsilon_m$); e-external solution ($G_e, \epsilon_e$); $R_e = R_{1,2,3}$- cell radii; $d_1$-membrane thickness; $d_2$-cell wall thickness; and I, II, III-boundary layers [191].*

***Table 8.2:*** *Solid shell model expressions to corresponding symbols [149].*

| Symbol | Expression |
|---|---|
| $A_1$ | $\epsilon_m(\epsilon_e - \epsilon_i) + \frac{d}{R_2}(\epsilon_i - \epsilon_m)(2\epsilon_m - \epsilon_e)$ |
| $A_2$ | $-\epsilon_m(\epsilon_i + 2\epsilon_e) - \frac{2d}{R_2}(\epsilon_i - \epsilon_m)(\epsilon_e - \epsilon_m)$ |
| $B_1$ | $-G_m(\epsilon_e - \epsilon_i) - \epsilon_m(G_e - G_i) - \frac{d}{R_2}\{(G_i - G_m)(2\epsilon_m + \epsilon_e) + (\epsilon_i - \epsilon_m)(2G_m + G_e)\} + \frac{2K_s}{R_2}(\epsilon_m - \frac{d}{R_2}(\epsilon_m - \epsilon_i))$ |
| $B_2$ | $G_m(\epsilon_i + 2\epsilon_e) + (G_i + 2G_e)\epsilon_m + \frac{2d}{R_2}\{(G_i - G_m)(\epsilon_e - \epsilon_m) + (\epsilon_i - \epsilon_m)(G_e - G_m)\} + \frac{2K_s}{R_2}(\epsilon_m - \frac{d}{R_2}(\epsilon_m - \epsilon_i))$ |
| $C_1$ | $-G_m(G_e - G_i) - \frac{d}{R_2}\{(G_i - G_m)(2G_m + G_e)\} + \frac{2K_s}{R_2}(G_m - \frac{d}{R_2}(G_m - G_i))$ |
| $C_2$ | $G_m(G_i + 2G_e) - \frac{2d}{R_2}\{(G_i - G_m)(G_e - G_m)\} + \frac{2K_s}{R_2}(G_m - \frac{d}{R_2}(G_m - G_i))$ |
| $\omega_{01}$ | $2\pi f_{01} = d/\{2\pi\epsilon_o\epsilon_m R_2\left(\frac{1}{G_i} + \frac{1}{2G_e(1 + Rel)}\right)\}$ |
| $\omega_{02}$ | $2\pi f_{02} = \{G_i + \frac{2G_e(1 + Rel)}{2\pi\epsilon_o(\epsilon_i + 2\epsilon_e)}\}$ |

Where,$\epsilon_i$ is cytoplasm permittivity, $\epsilon_e$ is medium permittivity, $G_i$ is cytoplasm conductivity, $G_e$ is medium conductivity, $G_m$ is membrane conductivity, $Rel$ is the surface charge.

### 8.1.2. Solid model

Given the experimental analysis results, in Chapter 6-7, bovine oocytes are known to be highly polarizable and the electrical equivalence of the membrane is equivalent to that of the cytoplasm, oocytes can also be considered a solid spherical object instead of a single shell, yielding:

$$\text{Torque: } N = 4\pi\epsilon_o\epsilon_e {R_2}^3 E^2 \left[\left(\frac{C_1}{C_2} - \frac{B_1}{B_2}\right)\left(\frac{\frac{\omega}{\omega_{02}}}{1+\left(\frac{\omega}{\omega_{02}}\right)^2}\right)\right] \qquad (8.3)$$

Equations (8.2) and (8.3) are analysed in comparison to experimental data to determine which model is best. Note that Equation (8.3) is obtained by ignoring frequency dependent factor $\omega_{02}$, since both membrane and cytoplasm shows electrical equivalency and no rotation is seen in the $\beta$ and $\gamma$ frequency zones.

## 8.2. Numerical computation of rotational torque

The DEP torque is solely dependent upon the electric field strength, conductivity and permittivity of particle, and the surrounding medium. From DEP torque, if the particle remains stationary in a liquid medium, its driving torque is compensated by its frictional moment. Using the Navier-Stokes equation for frictional moment, one can calculate the angular velocity ($\omega$) of the object, given by:

$$\omega = \frac{N}{8\pi\eta R^3} \qquad (8.4)$$

Where, $\eta$ is the viscosity of external medium and N is the DEP torque.

The values in Table 8.3 are employed to numerically plot the real and imaginary parts of CM in Equation (8.1), with the results shown in Figure 8.3. These CM factor values provide useful information regarding calculation and validation of numerical DEP torque.

***Table 8.3:*** *Parameter constant of cells and medium.*

| Item | Relative permittivity ($\epsilon$) | Conductivity ($\sigma$) |
|---|---|---|
| Normal oocyte cytoplasm [193] | 70 | 5 (mS/cm) |
| Polystyrene bead [184] | 2.55 | 1.2 (nS) |
| Buffer medium (DI water) [184] | 78 | 5.5e-6 (S/m) |

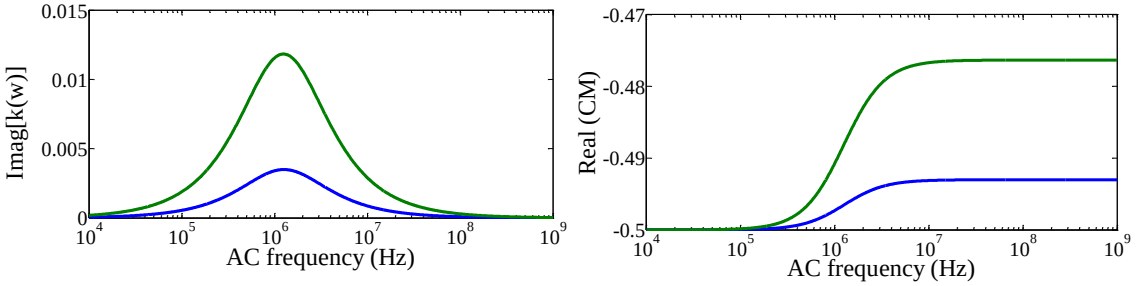


(a) (b)

***Figure 8.3:*** *Frequency dependency of particle rotation on complex conductivity and permittivity factors of spherical particle and the surrounding medium. Table 1 is used as a reference to obtain these plots. (a) Real part of CM factor (b) Imaginary part of CM factor.*

The shell model is considered for initial estimation of the rotational angular velocity of normal oocyte using a polystyrene bead for validation. The oocyte radius R is considered 60μm, and the capacitance and the conductance of the membrane are 1.25μF/cm2 and 400 Ω cm, respectively. Polystyrene beads have a 60μm radius with suitable permittivity and conductivities. These properties are used to numerically analyse angular velocity of rotation for polystyrene beads and bovine oocytes in comparison to experimental data.

## 8.3. Results and Discussion

A square ROT chamber of 750 µm is considered after the initial electric field analysis described in Chapter 4. Alternatively, electric field strength may vary with operable AC amplitude within the analysed ROT chamber. For this reason, the analysis is carried out to determine the field strength at AC amplitude between 5 Vp-p and 20 Vp-p. Figure 8.4, shows the plot of rotating electric field at the centre of ROT chamber with square sides of 750 µm length. Data from the plots shows a suitable operable electric AC amplitude potential necessary to design the micro-device without compromising the oocytes.

Analysis of the electric field strength in the 750 µm square chamber provided useful information as to how much AC amplitude is necessary to obtain the required field strength without compromising the viability of oocytes. Moreover, the experimental results in Chapter 6-7 have shown that 10 Vp-p AC amplitude is suitable for rotating bovine oocytes. Thus, based on these results, a field strength of $2.2 \times 10^4$ V/m is considered for numerical analysis of dielectric spectrum or the angular velocity calculation.

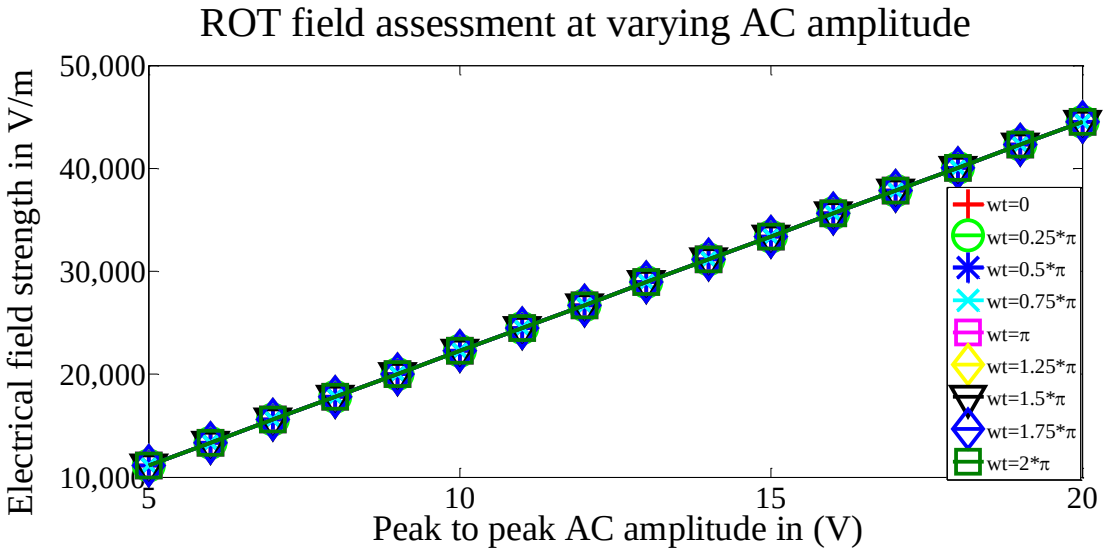


***Figure 8.4:*** *Electric field norm in volts per meter at varying amplitude of applied AC potential. Between 5 to 20 volts to ROT fields are present and between 10 to 20 Vp-p AC amplitude, the electric field strength is sufficient at single period.*

From initial numerical analysis using a shell model along with initial analysis of rotation field strength, two peaks in the numerical rotational spectrum plots are obtained. These peaks, in Figure 8.5, indicate clockwise and anticlockwise rotation of the particle in yaw. The negative peak indicatives a particle that is less polarized than the medium and thus, these particles rotate against the electric field direction vector and strength. In contrast, the positive peak indicates a particle more polarized than the surrounding medium making it to rotate in the direction of the rotational field vector.

At 5.5 kHz AC frequency, Maxwell-Wagner (MW) relaxation is evident from the initial computations. This behaviour occurs at the crossover frequency, indicating particle polarizability equal to the surrounding medium. After this crossover frequency, the particle again becomes more polarizable than the medium, resulting in clockwise rotation. To validate the numerical analysis the experimental results of Chapter 6-7 are used for comparison.

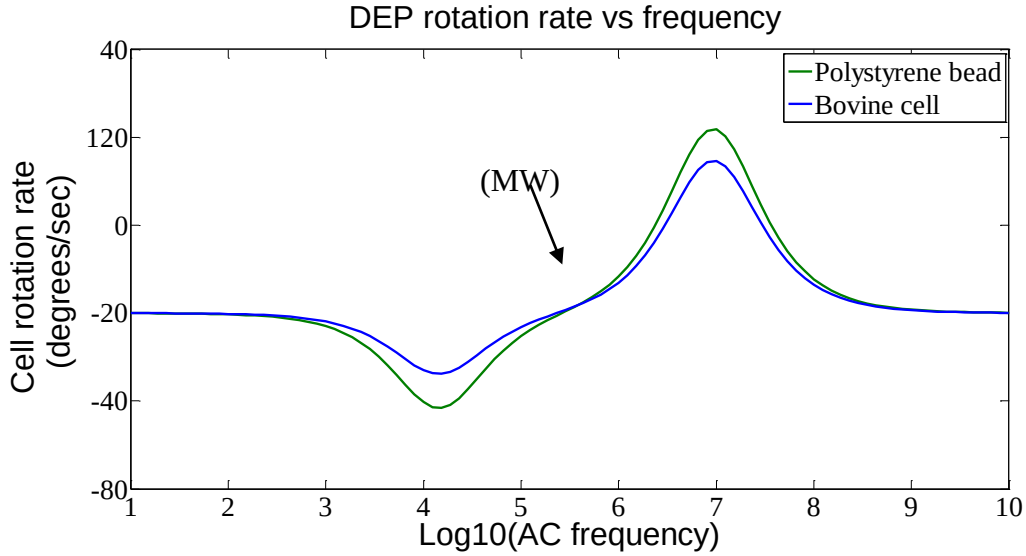


***Figure 8.5:*** *Frequency dependency of particle rotation on complex conductivity and permittivity factors of cell and the surrounding medium. Table 1 is used as a reference to obtain these plots (a). Real part of CM factor (b). Imaginary part shows a positive peak, to indicate particle rotation in clockwise direction. Negative peak indicates particle rotation in anticlockwise direction. (c). Rotation rate of bovine cell and polystyrene bead at $2\times10^4$ V/m field strength.*

### 8.3.1. Experimental model validation

Figure 8.6, shows yaw and pitch axis rotation image sequences. A comparison of the rotation spectrum plots between experimental and simulated results is shown in Figure 8.7. For the simulation, the bovine oocyte was anatomically treated as a spherical shell model. Consistent with the simulation, the yaw axis rotational experimental results had only one peak in a higher frequency region between 500 kHz to 10 MHz, indicating that the bovine oocytes are highly more polarizable than the medium. The deviation in the peak value is attributed to errors in the selection of model parameters, such as oocyte/medium permittivity and conductivity, used in the simulation. Due to the absence of a negative rotation peak in the lower frequency region between 0-500 kHz, the Maxwell Wagner (MW) relaxation at a critical frequency of 500 kHz is eliminated.

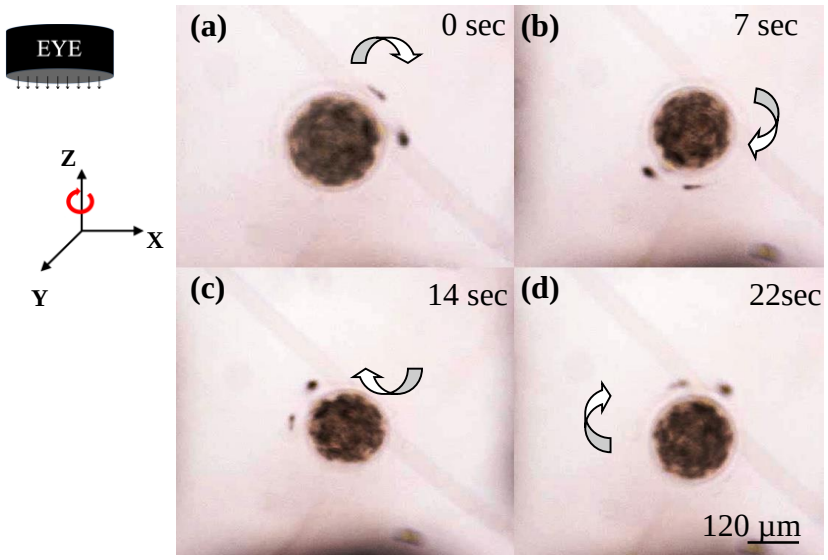


***Figure 8.6:*** *Experimental results. (a-d). Co-ordinate system along with a single bovine oocyte undergoing yaw axis rotation at 10 Vp-p, 500 kHz frequency and 90° phase shift between two pairs of orthogonally arranged vertical electrodes. Arrow shows rotation direction of oocyte.* [41]

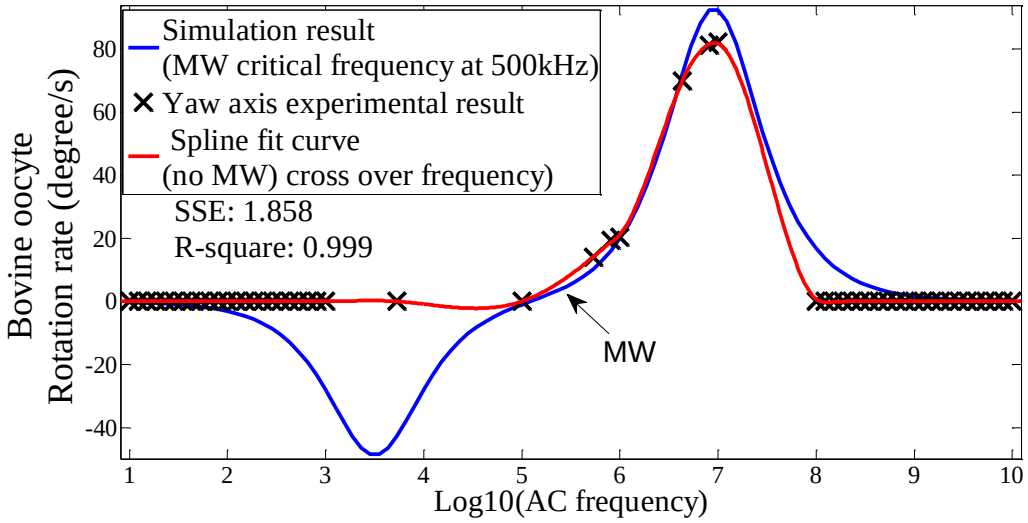


***Figure 8.7:*** *Comparison of simulated and experimental rotation rates of bovine oocyte with respect to z-axis (yaw-axis rotation). Only one peak is evident from experimental results, showing bovine cells are consistently more polarizable than the surrounding medium over the frequency range. Electric field strength is 2×103 V/m at 10Vp-p AC amplitude. Experimental measured medium conductivity=3.5µS/cm and permittivity of medium is 70. Numerical simulation medium conductivity=5.5e-6 S/m. Bovine oocyte cytoplasm conductivity=5mS/cm. Membrane thickness (d) =9nm.*[41]

Compared to yaw axis rotation, the experimental dielectric spectrum during pitch axis rotation (see Figure 8.8) differs from the numerical simulation result in which the rotation peak occurs at 10-100 kHz. Pitch rotation numerical and experimental results are compared in Figure 8.9, where maximum rotation is seen at a lower frequency and rotation rate in the model.

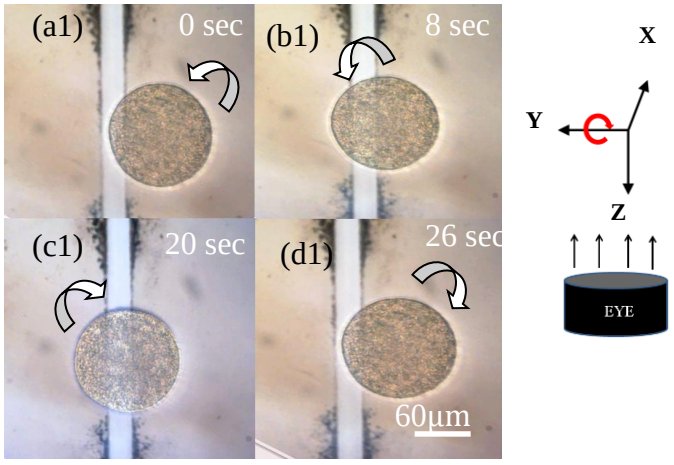


***Figure 8.8:*** *Experimental results. (a1-d1). Co-ordinate system along with a single oocyte undergoing pitch axis rotation at 10 Vp-p, 80 kHz frequency and 50° phase shift between two bottom electrodes and grounded vertical electrodes. Arrow shows the rotation direction of oocyte rotation.*

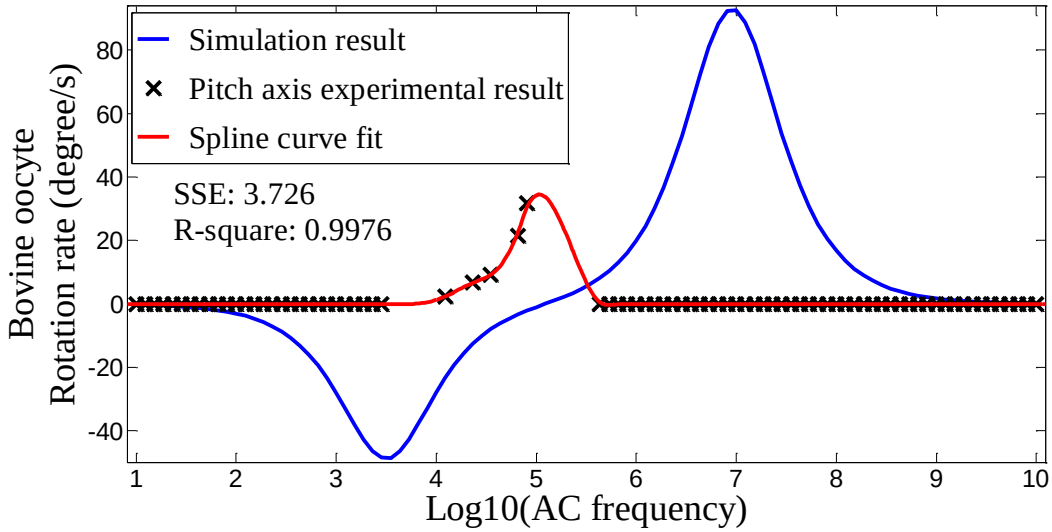


***Figure 8.9:*** *Experimental rotation rate of bovine oocyte with respect to y-axis (pitch). Electric field strength is $2\times10^4$ V/m at 10 Vp-p AC amplitude. Electric field strength is 2×103 V/m at 10 Vp-p amplitude. Experimental measured medium conductivity=3.5μS/cm and permittivity of medium is taken as 70. Numerical simulation medium conductivity=5.5e-6 S/m. Bovine oocyte cytoplasm conductivity=5mS/cm. Membrane thickness (d) =9nm* [41].

Comparison of rotation spectrum of numerical and experimental results are validated and found that bovine oocytes during yaw rotation consist of internal conductivity of 5 mS/cm referring to Table 8.3, where both the numerical and experimental results showed close resemblance. Yaw rotation findings suggest that bovine oocytes are highly polarizable than the surrounding medium and can be treated as solid spherical model. Finally, from the validation of yaw and pitch-axis rotation, it is evident that bovine oocytes rotation well within the classification of $\beta$ frequency zone, but with only one peak.

However, numerical computation of the solid shell model during pitch rotation showed differences in maximum peak values of rotation spectra with respect to the experimental results. This difference in rotation spectra is majorly due to rolling on the oocyte. Rolling phenomenon can be attributed to the unbalanced hydrodynamic force and frictional drag force on the particle; this further validates simulation results shown in Chapter 4. The numerical model presented till date is for yaw axis rotation only. Comparison of experimental results of pitch rotation spectra to the solid shell model in yaw may not be a compatible match.

Certain parameters can be tweaked to get closer to the experiments by optimizing numerical parameters. Some of the parameters are defined below:

- Optimizing the rotating electric field strength in numerical simulation model.
- Optimizing conductivity and permittivity parameters.

Figure 8.10, shows the numerically optimized electric field strength for validation. Positive rotation spectrum peak of numerical result reduced from a maximum of 150 degree per second to 50 degree per second and negative spectrum peak reduced to half of the initial model, resulting in a closer match to the experimental results.

However, compared to only one positive experimental spectrum peak, numerical model during pitch rotation is still cannot be closely comparable. Moreover, the frequency range at which the rotation peaks happen are also different. This asks for further optimizing the numerical simulation model. Hence, the objective at present is to optimize the simulated rotation spectrum peak to shift from 0-100 MHz range to 10 kHz-10 MHz AC applied frequency range within which experimental data can be validated.

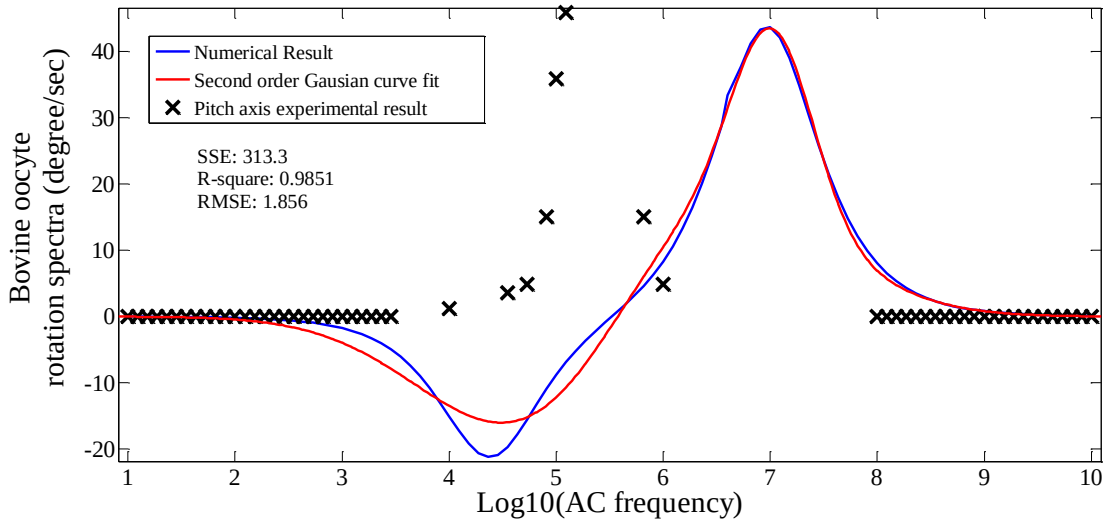


***Figure 8.10:*** *Experimental rotation rate of bovine oocyte with respect to y-axis (pitch). Electric field strength is 1.5×103 V/m at 10 Vp-p AC amplitude. Experimental measured medium conductivity=3.5µS/cm and permittivity of medium is taken as 70. Numerical simulation medium conductivity=5.5e-6 S/m. Bovine oocyte cytoplasm conductivity=5mS/cm. Membrane thickness (d) =9nm.*

A closer comparison can be seen in Figure 8.11, where, numerically simulated aspect of medium and particle properties is being tweaked to get close to the experimental findings. In the plot shown, the buffer medium conductivity is reduced to 5.5e-12 S/m, normal bovine oocyte cytoplasm conductivity is optimized to 3.5e-6 S/cm and Zona Pellucida thickness (d) is removed. Negative peak in the simulation is now being removed due to the removal of Zona from the solid shell model; this validates and proves that the bovine oocytes are solid shell objects instead of multilayer shell. The model closely validates the experimental results with the numerical simulation and is closely matched. Thus validation provides a means to determine the electrical properties of the bovine oocyte. Oocyte (without Zona Pellucida) properties are thus determined to be having cytoplasm and electrically equivalent membrane conductivity of 3.5 µS/cm and permittivity of 70.

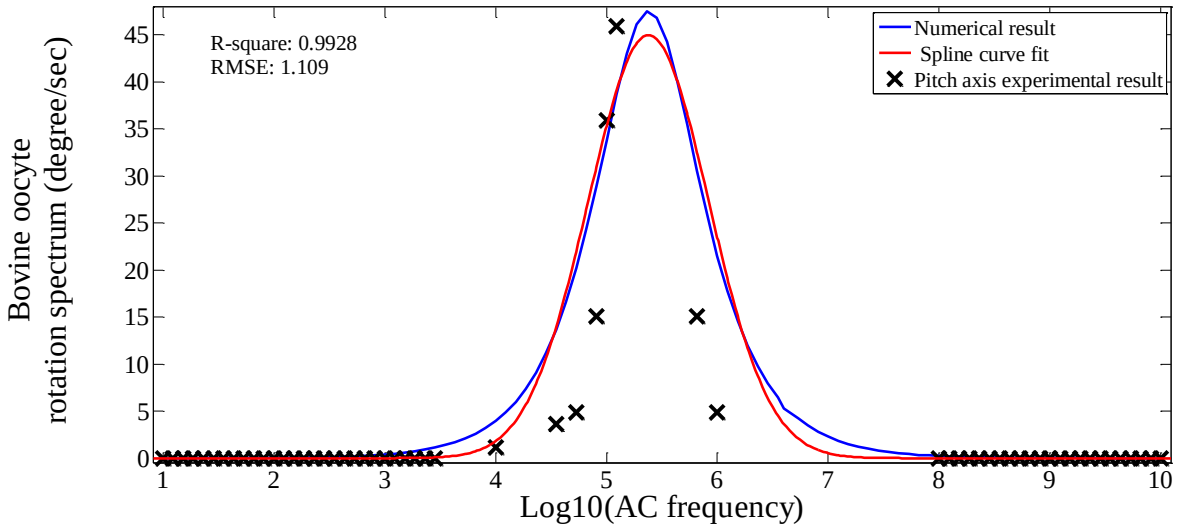


***Figure 8.11:*** *Experimental rotation rate of bovine oocyte with respect to y-axis (pitch). Electric field strength is 1.5×103 V/m at 10 Vp-p AC amplitude. Experimental measured medium conductivity=3.5µS/cm and permittivity of medium is taken as 70. Numerical simulation medium conductivity=5.5e-12 S/m. Bovine oocyte cytoplasm conductivity=3.5S/cm. Membrane thickness (d) =0.*

Even though there is a minor difference, validation provides vital clue in characterising the rotation spectra of bovine oocyte. Moreover, the results showed remarkable promise to optimise the biochip required to rotate bovine oocytes in yaw and pitch-axis. Pitch axis rotation is estimated to be suitable between the AC fields of frequency10 kHz to 100 kHz and the yaw axis rotation between 100 kHz till 10 MHz. Further, the biochip working solely on the DEP

phenomenon to rotate cells in 3D spaces can find immediate applications in automation of enucleation during nuclear transfer cloning.

## 8.4. Summary

Numerical and experimental study required to analyse electro-rotation spectrum is validated in this chapter. Bovine oocytes are thus concluded to be highly polarizable solid spherical. Experimental yaw and pitch axis rotation validation showed closer resemblance to the numerical model. Validation results provide a means to optimize the biochip for rotating mammalian oocytes and different size and type of cells. Existing theoretical background allows the numerical computation and simulation of rotational behaviour of particles, such as cells, with complex structures. Conductivities and permittivity can be determined from the validation results. Hence, without any doubt, the electro-rotation in the biochip provides promising addition to active and passive electrical measuring techniques at low cost.

# Chapter 9. Experimental Validation – 3D Motion

Scientists are very often confronted by unexpected findings that demand new approaches, and they discover that yesterday's "sophisticated tools" are today's "blunt instruments" [181, 191]. One such discovery is particle rotation for which numerous micro-devices and state-of-the-art techniques, such as phase varying DEP (electro-rotation), optics and acoustic particle manipulation, have come into existence. Nonetheless, each of these techniques has its advantages and disadvantages. Current particle manipulation demands sophisticated micro-devices to manage and control particles in 3D spaces. The flexible and low cost biochip presented in this research provides such a sophisticated tool to analyse and characterise particles in 3D spaces, providing a significant advantage in the state-of-the-art. Rotation of spherical particles in 3D spaces plays a vital role in the analysis of bovine egg cell morphology, and in current and future biotechnology applications. Previous chapters have already shown that the biochip can successfully rotate bovine oocytes around the yaw and pitch axes. In comparison to previous chapters, this chapter will provide validation for a single bovine oocyte rotation simultaneously in both yaw and pitch. Simultaneous rotation in yaw and pitch validates the overall ability to provide rotation in 3D spaces.

## 9.1. Experimental validation for 3D rotation

The Euclidean space to rotate a spherical particle generally consists of three major axes: yaw (rotation about Z co-ordinate), pitch (rotation about X/Y co-ordinate) and roll (rotation about Z co-ordinate) [194, 195]. Euler angles are commonly used to explain 3D rotation of objects in Euclidean space. The representation of any 3D rotation can be decomposed into three separate angles and can be classified in four types of rotation nomenclatures:

- Order of combining angles.
- Relative to rotating object or absolute coordinates.
- Left or right hand rotation.
- Notation for angles.

In this research, the relative to rotating object or absolute coordinates are considered, as rotation of bovine oocytes is performed with respect to the X, Y and Z coordinates. One can rotate an object either about the X, Y or Z axis, as shown in Figure 9.1. There are three resulting angles of rotation defined:

- φ: heading = rotation about Y.
- θ: attitude = angle about Z.
- ψ: bank= angle about X.

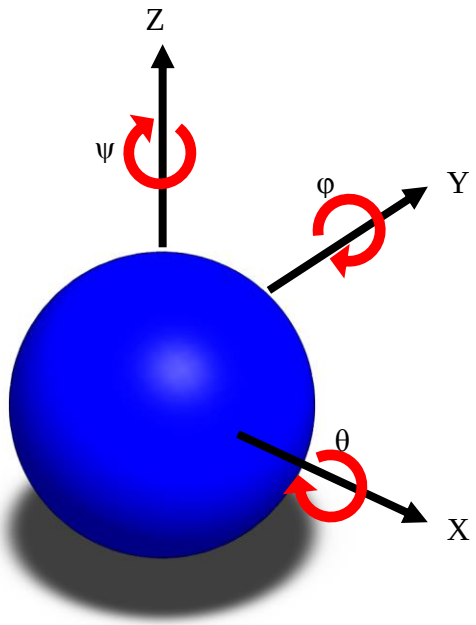


***Figure 9.1:*** *Illustration of rotation axes in 3D spaces. A homogenous spherical particle can undergo rotation in any three major axes of space. Totally three degrees of freedom is available for spherical particle in Euclidian space.*

Rotation around the X,Y and Z axes can be combined to show that only two axes of rotation of a spherical object will provide rotation in the third dimension. Thus rotation about the Z-axis and rotation about the Y-axis, as shown in Figure 9.2, can also produce a net rotation about X-axis. This aspect is mathematically shown:

$$[R1] = \begin{bmatrix} \cos(\varphi) & -\sin(\varphi) & 0 \\ \sin(\varphi) & \cos(\varphi) & 0 \\ 0 & 0 & 1 \end{bmatrix} \quad (9.1)$$

$$[R2] = \begin{bmatrix} \cos(\theta) & 0 & -\sin(\theta) \\ 0 & 1 & 0 \\ \sin(\theta) & 0 & \cos(\theta) \end{bmatrix} \quad (9.2)$$

$$[R3] = \begin{bmatrix} \cos(\psi) & -\sin(\psi) & 0 \\ \sin(\psi) & \cos(\psi) & 0 \\ 0 & 0 & 1 \end{bmatrix} \quad (9.3)$$

The combined transformation matrix is defined:

$$[R] = [R3][R2][R1] \quad (9.4)$$

Solving for $[R]$ gives (For simplicity; cos =c, sin=s):

$$[R] = \begin{bmatrix} c\,\psi * c\,\theta * c\,\varphi - s\,\psi * s\varphi & -c\,\psi * c\,\theta * s\,\varphi - s\,\psi * c\varphi & c\,\psi * s\,\theta \\ s\psi * c\,\theta * c\,\varphi + c\psi * s\varphi & -s\psi * c\,\theta * s\,\varphi + c\psi * c\varphi & s\psi * s\,\theta \\ -s\,\theta * c\,\varphi & s\,\theta * s\,\varphi & c\,\theta \end{bmatrix} \quad (9.5)$$

According to the rotational transformation matrix in Equation (9.5), rotation of any point on the sphere with respect to two axes of rotation (about Z and about Y) will yield a defined rotation around the third (X-axis). Hence, if the biochip can rotate spherical bovine oocytes simultaneously in yaw and pitch or pitch, and roll or yaw and roll, it is sufficient to obtain a defined 3D rotation of the oocyte.

Figure 9.2, shows the rotation of a bovine oocyte in the biochip simultaneously rotating around the yaw and pitch axes. Video files are attached as a supplementary file to support this case. Bovine oocytes are rotated around the pitch axis using an AC applied frequency of 40 kHz with 10 Vp-p. Pitch rotation is witnessed at 50° phase shift. However, due to the contact of the oocyte with the bottom ITO electrodes of the biochip, a small amount of cell lyses resulted. Simultaneously, rotation in yaw is obtained using 10 Vp-p applied at 500 kHz.

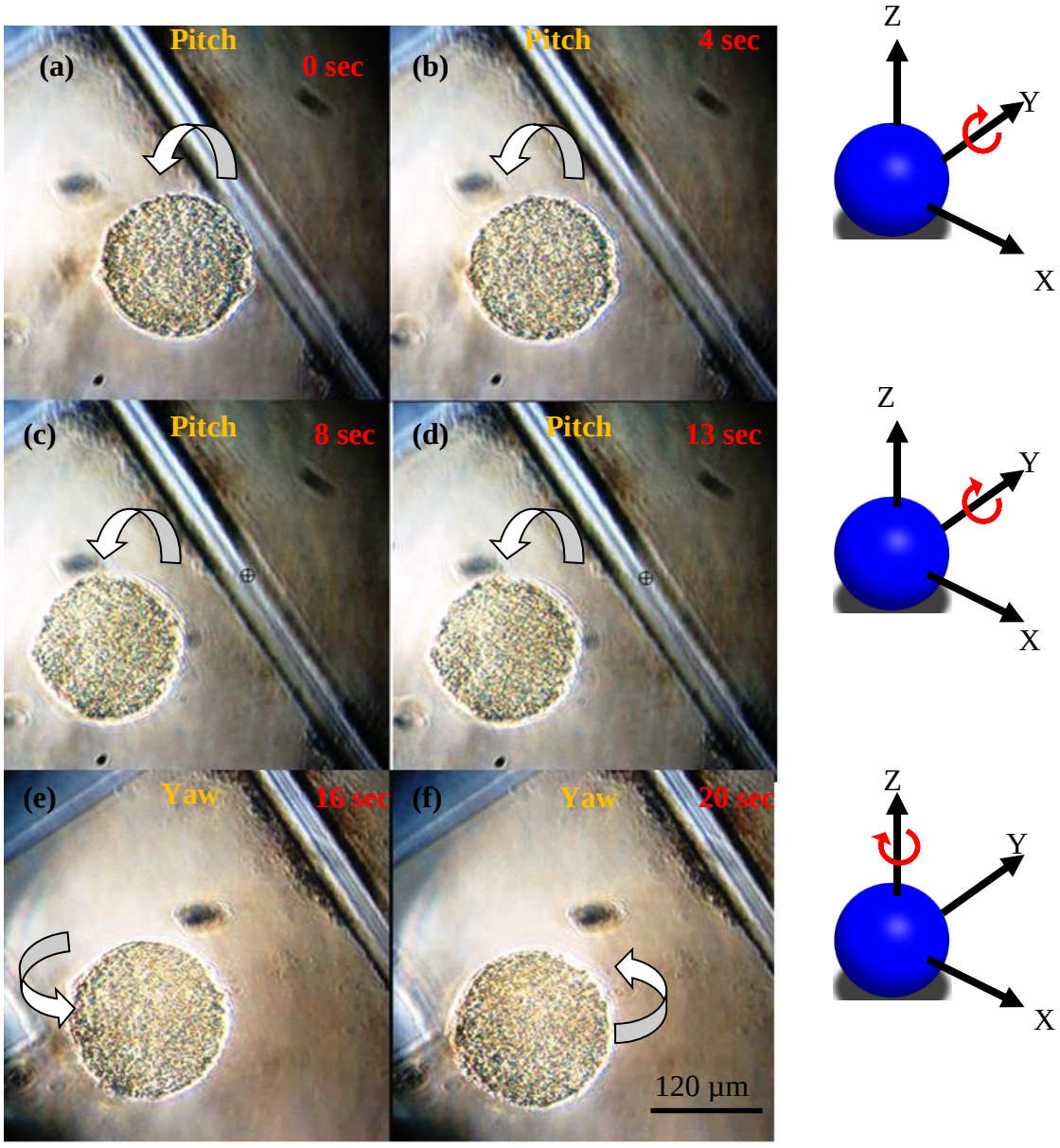


***Figure 9.2:*** *Experimental rotation rate of bovine oocyte with respect to x and y-axis (pitch). Electric field strength is $2\times10^4$ V/m at 10 Vp-p. ((SI: video 9).*

Cell disintegration or lyses is nontrivial in practice. Two potential causes are the electric field magnitude and the physical properties of plasma under high frequency excitation. Simulation in COMSOL showed that the peak magnitude (data not shown here) occurs in the center region of the biochip chamber for in-plane rotation and in the region above the bottom electrode gap for rolling rotation, with a value of $3\times10^4$ V/m, and $1.6\times10^4$ V/m, respectively, for an AC amplitude 10 Vp-p. Previously reported DEP-based cell fusion [196] and electroporation [197] offers clues that this continuously-applied field is strong enough to make pores on the cell circumference. The result is that the oocyte lyses is very hard to avoid unless controlled with lower field strength generation.

The second possible reason is related to the physical property of the plasma under high frequency excitation. In a recent tutorial paper [198], it was mentioned that a rotating cell sample lyses in ultrasonic standing-wave fields. Likewise, under a high frequency AC field, it is not surprising for oocytes to have undergone a process of breaking up into fragments as observed experimentally, especially those cells that are simultaneously subject to DEP-induced rotation.

Therefore, to minimize cell disintegration in practice, a logical solution includes a proper combination of the applied amplitude and frequency. For example, two combinations (10 Vp-p and 500 kHz for yaw, and 10 Vp-p and 40 kHz for pitch rotation) could be recommended for rotating bovine oocytes based on the experiment results in Chapter 7 and Chapter 8.

DEP is known to generate heating [199], which is a factor that can affect the cell and its viability. In experiments, the temperature change in the medium was not measured, because the main purpose was to demonstrate cell rotation. Furthermore, at low AC frequencies less than 10 kHz, the electrodes started to corrode and the electrochemical reactions generated air bubbles, which should be avoided. Another general observation was that during rolling rotation oocytes tended to simultaneously sink to the bottom electrodes. Notably, this behaviour did not occur for in-plane rotation. A COMSOL simulation described in Chapter 3 found that there is a DEP drag force pulling the oocyte down to the bottom for roll (y-axis) rotation, but not for in-plane (z-axis) rotation. To counter this drag force, extra care should be taken to optimize the geometry and design of the bottom electrodes.

Oocyte lyses or disintegration can be directly linked to the contact with the ITO electrode during rolling or due to the amount of heat generated in the oocyte. During this time, the oocyte internal structure starts to deteriorate and continuous application of the field may result in cell death. This outcome can be avoided by properly suspending the oocyte, as shown in Figure 9.3. Suspending the oocyte avoids oocyte contact with the bottom ITO substrate and provides rotation of viable oocytes. Even though suspension of the oocyte is achieved, as portrayed in Figure 9.3, rotation speed is hindered to certain extent, largely due to the more viscous solution mixture required to suspend the cell.

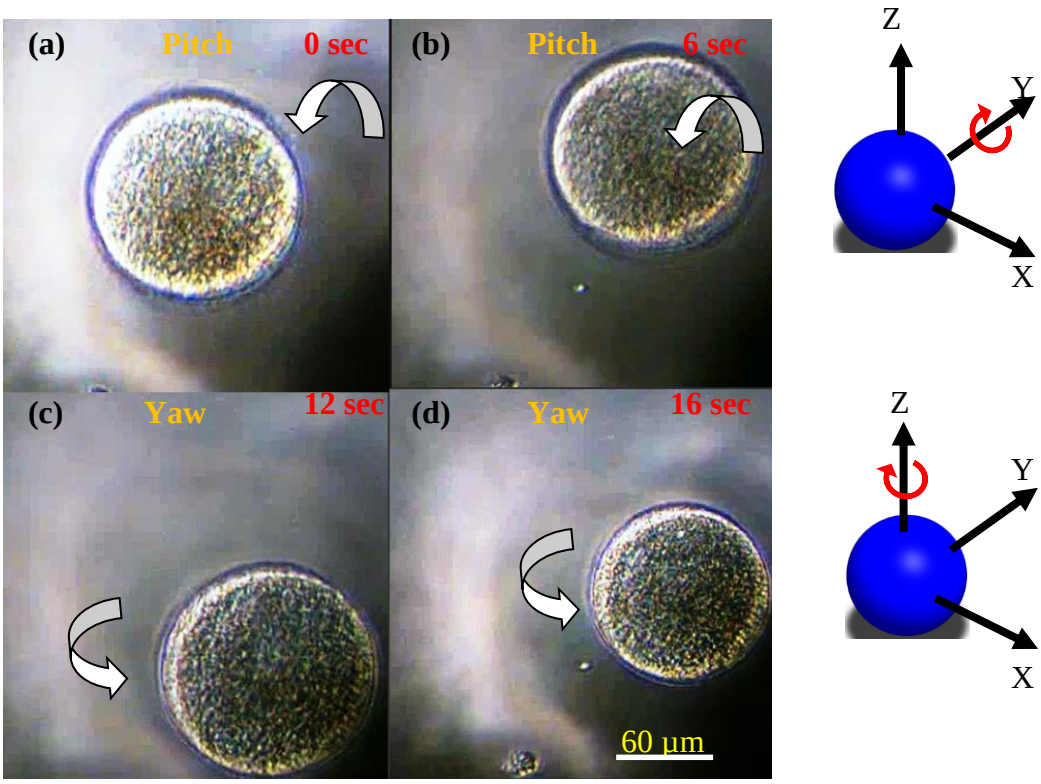


***Figure 9.3:*** *Experimental rotation rate of bovine oocyte with respect to x and y-axis (pitch). Electric field strength is $2\times10^4$ V/m at 10 Vp-p. (SI: video 10).*

Finally, the rotation spectrum for 3D rotation of the bovine oocyte is shown in Figure 9.4. The plot is obtained by considering the oocyte under simultaneous rotation around both yaw and pitch (in-plane or out of plane) axes. Error bars are obtained by calculating the percent standard deviation observed between three to four oocytes. Less than 0.5% error is seen in the yaw

rotation calculation and during pitch rotation less than 1% standard deviation error is seen. Rotation from Figure 9.3 is considered for analysis. Finally, the spectrum plot shows two peaks, one for yaw axis rotation and other for pitch axis rotation. Both of these rotation spectra are well within the $\beta$ or $\gamma$ frequency range referred to in Chapter 8.

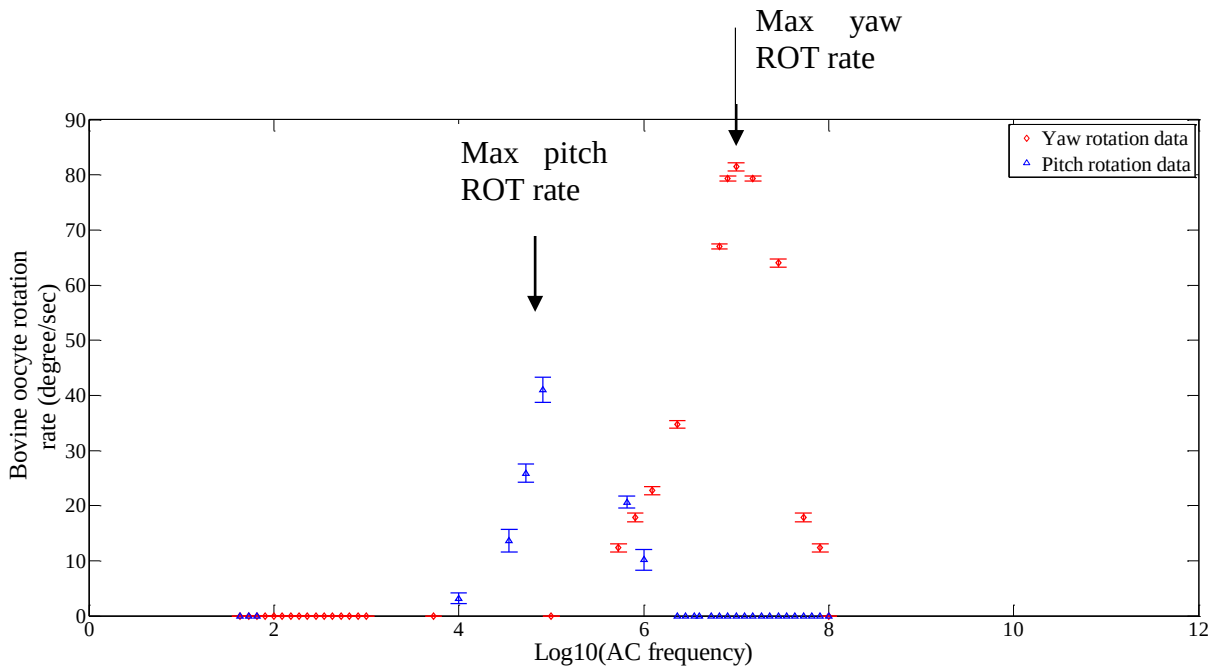


***Figure 9.4:*** *Experimental rotation rate of bovine oocyte with respect to x-axis (yaw) and y-axis (pitch). Electric field strength is 1.5×103 V/m at 10 Vp-p peak-to peak potential. Experimental measured medium conductivity=3.5μS/cm and permittivity of medium is taken as 70. Bovine oocyte cytoplasm conductivity=3.5S/cm. Membrane thickness (d) =0.*

## 9.2. Summary

In this chapter, validation of 3D rotation is presented based on simultaneous rotation around both yaw (in-plane) and pitch (out-of-plane) axes. From the experiments, it is shown to be essential to suspend the oocyte in a perfect conductive and efficient viscous medium. If cells are not suspended, lyses or cell disintegration occurs, resulting in cell death. Nonetheless, the micro-device is capable of rotating a spherical polarizable particle in 3D spaces through electro-rotation or DEP based rotation. A spectrum plot for simultaneous rotation of bovine oocytes around both the yaw and pitch axes are presented, which occurs well within the expected $\beta$ or $\gamma$ frequency range and fully validate this aspect of the biochips performance.

# Chapter 10. Conclusions

Study of an open-top, non-contact and precision controlled DEP-based particle rotation in 3D spaces can significantly aid the development of lab-on-chip devices for enucleation, cell characterisation, and determining 3D cell surface imprints, and many other possible application. Several relevant micro-devices have rotated cells, around a single axis, such as by Becker et al., [163], where human Leukocyte subpopulations were subjected to DEP and electrorotation using a closed top micro-device in one single axis and required complicated, and costly micro fabrication procedures. A 3D eight-electrode structure was recently designed by Han et al., [52] to determine the electrorotation dielectric spectra of human leukocyte subpopulations (T and B lymphocytes, granulocytes, and monocytes) and metastatic human breast (SkBr3) and lung (A549) cancer cell lines. However, the eight-electrode system utilised was closed-top, which makes it impossible to further process rotated cells. There were other significant disadvantages, as well, creating a significant need for a low cost, simple method of controlled 3D rotation that enabled further cell or particle manipulation after rotation.

This research project was aimed at rotating a spherical dielectric particles and bovine oocyte in particular, in 3D spaces. Major goals achieved in this research, include:

- A low-cost micro-device manufacturing process was developed and a device was fabricated to rotate particles in 3D spaces through the combination of micro-milled vertical walls and the RF sputtered bottom ITO electrode patterns.
- The biochip and electric rotational fields were modelled, optimised and fully characterised using multi-physics FEA.
- Experimental rotation and dielectric rotation spectrum results were determined in the yaw (in-plane) and pitch (out-of-plane) axes rotation, demonstrating precision control.
- The experimental results were validated using the numerical computations, and, as a result, the bovine oocyte electrical properties were defined.
- Simultaneous dual-axis, 3D rotation of the bovine oocytes in 3D spaces were demonstrated to conclusively validate the research.

Initially, Chapter 1 defined the problems involved in enucleation processes during nuclear transfer. Research background and the necessity for the automation of high throughput enucleation were discussed. As a result, particle rotation in 3D spaces using a non-contact DEP-based electro-rotation was determined to be essential to achieve efficient high throughput and repeatability. Problems involved during DEP-based rotation were addressed and parameters necessary to achieve a successful rotation in 3D spaces were defined. A principle of rotation using vertical and bottom electrodes were proposed and were implemented to validate the biochip functionality.

After defining the rotation device principle, an unique fabrication process was developed to manufacture the biochip. The biochip was successfully fabricated through the fusion of micro-milling and photolithography technique considering the bovine oocyte size of 120 μm. The micro-milling was found to be suitable to fabricate the rotation chamber width and height, aligned manually on top of the ITO electrode patterns. This mode of fabrication is very cost effective and simple compared to electroplating and current micro-fabrication techniques, creating a low-cost solution.

The overall biochip system functionality was analysed using electric field simulations in Chapter 4. From the simulation and numerical analyses, the phase varying rotational electric field strength in magnitude remains constant at the center of the rotation chamber enabling rotation without translation around same axes, as well as more precise control. Analysis of out-of-plane actuation due to rotational fields generated by the vertical and bottom electrodes show that the combination of AC potentials yields equivalent rotational field strength to rotate particles in and out-of-plane, making the biochip versatile for full 3D rotation. Further, simulations were successful in explaining a resulting cell rolling phenomenon, where during out-of-plane actuation, the DEP field strength is shown to be uneven along the circumference of the spherical particle, causing rolling unless the particles are suspended within a perfect suspension medium. Hence, the importance of viscosity and the dielectric properties of the surrounding medium were highlighted and characterised as playing a vital role in influencing rotation. From this basic understanding, an initial biochip design was optimized.

The results of the experiments were successfully validated with numerical and theoretical analysis, and the dielectric properties of the bovine oocytes were quantified for the first time. The experimental results clearly demonstrated the efficacy of the system leading to preliminary, but interesting, findings related to the rotation of bovine oocytes specifically:

- The rotation rate or angular velocity of the bovine oocyte depends on the applied AC frequency along with the dielectric properties of the oocyte and its surrounding medium.
- With increased medium conductivity the rotation rate increased.
- Zona-intact and zona-free oocytes were electrically equivalent, meaning oocyte cytoplasm and the surrounding zona membrane consist of equivalent dielectric properties. This outcome will further aid enucleation and adds versatility to the biochip's capabilities.
- The biochip can deliver controlled DEP-based rotation of the bovine oocyte in 3D spaces.
- In-plane rotation rates are higher than out-of-plane rotation rate with the increasing applied AC frequency, which is indirectly attributed to the rolling phenomenon during out-of-plane actuation. This rolling phenomenon was fully quantified and characterised.
- Experimental validation in Chapter 8 highlighted that the bovine oocytes are solid spherical objects and are highly polarizable than the surrounding medium.

Finally, in Chapter 9, bovine oocytes were simultaneously rotated around in-plane and out-of-plane axes. The results showed the ability to fully control rotation in 3D spaces to within 5-10 degrees in full multi-axis rotation. The biochip can also be used to determine the rotation rate of the bovine oocyte and thus quantify electro-kinetic properties of cells as well as to compare forces associated with different dielectric particles.

Finally, this biochip can be mass produced in arrays of cost effective and flexible open-top systems to quantify the DEP-based phase varying torque and qualitatively analyse a rotating bovine oocyte or any dielectric particle in 3D spaces. Equally, such arrays can have commercial potential. These outcomes are a significant step forward as they enable researchers to explicitly

quantify and understand the relative difference in DEP-torques exerted on the oocyte during rotation, as well as enabling significantly improved cell manipulation.

In summary, a DEP-based biochip platform was constructed by a mixture of fabrication methods including standard photolithography and micro-milling processes. Within the sub-mm square chamber of the biochip, simultaneous controlled rotation about two orthogonal axes of bovine oocyte was demonstrated. The rotation direction and rate are controlled via a set of options by changing the AC power amplitude, frequency, phase shift, and cell medium conductivity. Through the rotation rate spectrums obtained, it is found that bovine oocytes can be treated as solid spheres and there seems no noticeable difference for zona-intact and zona-free oocytes, demonstrating the capability of using this biochip platform to characterize cell dielectric properties. Once closed-loop controlled by a computer, the biochip platform can be more powerful coupled with extra function modules due to the simple, transparent, and low-cost open-top design.

In a nutshell following key points highlight the novelty, which support the statements made in the abstract section of this thesis.

- Rotation of suspended spherical oocytes in multiple axes (3D rotation) was obtained by AC induced electric fields in a single micro-device (biochip).
- An open top biochip was successfully fabricated to enable further processing of the rotated cell in 3D spaces.
- Bovine oocyte dielectric spectra were analysed in both in-plane and out-of-plane axes for the first time.
- Bovine oocytes were determined to behave as solid spherical spheres, rather than single shell spherical shells.
- The dielectric spectrum plot in out-of-plane was demonstrated for the first time and is novel.

# Chapter 11. Future work

The fabrication of micro-device to precisely control the 3D particle rotation solely working on DEP is still a challenge. Because, typically a micro-device requires four vertical electrodes of at least 500µm in height and two bottom electrodes to attain DEP-based 3D rotation phenomenon as discussed in Chapter 3. Electroplating require immense amount of resources and time to plate 500µm vertical electrodes. Remaining metal deposition techniques such as RF sputtering, dry and wet etching can only deposit metallic material of the order of few microns. Hence, fabricating a micro-device for this 3D rotation is difficult and requires deep thinking. Currently, new age technologies such as 3D printing and laser cutting are able to facilitate the requirement of producing a suitable micro-device, but it will take some time in near future. Nonetheless, the fabrication of a micro-device apart from the biochip reported in this research to rate dielectric particles in 3D spaces with precision control still remains a quandary.

Another possibility of future work is to study the simulation of DEP-based electro-rotation phenomenon to optimize compact and precise rotation control device. Since, through simulation studies, one can further optimize and characterize the rotational fields which can be produced by upcoming new technologies in photolithography, electroplating and 3D metallic printing. The current work presented here is not able to have only one fabrication method instead used fusion of micro-milling and photolithography techniques. It would be easier if one can optimize the rotational fields to suit 3D rotation of particles in just one single fabrication technique. This could avoid manually aligning vertical electrodes on top of bottom ITO, making the device even simpler.

Current simulation results shown in Chapter 4 are for stationary solvers with certain characterized parameters such as medium dielectric properties and electrode material characteristics. Simulating a real world environment of oocyte rotating with time varying parameters are highly challenging. On the contrary time-harmonic dependent rotational field simulations results into singularity. Because, at the center of the chamber (without the particle) the rotational field strength remains constant but varying with frequency. This means, at a certain continuously applied AC frequency, time heads to a constant value and entire rotational

phenomenon depends solely on the varying angular frequency. Currently, none of the tools have been built to address the issue of determining dielectric spectrum using a real time simulated rotational fields on the particle. Further, currently available FEA simulation software's such as COMSOL, and ANSYS, fail to provide suitable solution to DEP-based rotation phenomenon. Solving independent partial differential equation solver in FEA software is another way out, but again rotational field vectors are tensors, and require one to investigate 3D fields in order to simulate electro-rotational phenomenon. Numerical analysis is other possibility, but it lacks flexibility in calibrating electrode shapes and hence fails to optimize a device for suitable rotation. From the future point of view, suitable software needs to be designed to simulate real world dielectric particle rotation and provide dielectric rotation spectrum of the particles in the optimized rotational fields.

Apart from simulation and device fabrication, calculation of rotation rate of rotating oocyte through visually automated means is another challenge. As discussed in Chapter 5, rotation measurements are carried our using manual tracking in ImageJ software. This may induce manual errors while calculating the rotation rate of oocytes. Further, oocytes rotate by shifting the centre axis on some occasions and consist of near transparent uniform surface, making it difficult to track rotation. Currently, researchers have used image processing based rotation algorithms to determine the rotation rate [190], but it is not commercially available. For this reason, one can work on a new PhD project concentrated entirely on computer vision or developing image processing algorithm to automatically determine the rotation rate of the oocytes.

Finally, this research project provides a biochip to suitably rotate bovine oocyte in 3D spaces and supports the experimental findings with the numerical validations. The integration of the biochip with a closed loop control system to simultaneously apply AC sinusoidal potential along with an automated vision based rotation tracking algorithm would provide a complete lab-on-chip platform for biologists to carry out cell rotation and automated enucleation with high throughput. The automation of this can further facilitate high-throughput screening of cell handling and characterization.

# Chapter 12. References


1. N. Aubry and P. Singh, *Control of electrostatic particle-particle interactions in dielectrophoresis.* EPL (Europhysics Letters), 2006. **74**(4): p. 623.

2. N. Aubry and P. Singh, *Influence of particle-particle interactions and particles rotational motion in traveling wave dielectrophoresis.* Electrophoresis, 2006. **27**(3): p. 703-15.

3. J. Kadaksham, P. Singh, and N. Aubry, *Dielectrophoresis induced clustering regimes of viable yeast cells.* Electrophoresis, 2005. **26**(19): p. 3738-44.

4. J. Muthuswamy, et al., *Electrostatic microactuators for precise positioning of neural microelectrodes.* IEEE Trans Biomed Eng, 2005. **52**(10): p. 1748-55.

5. S. Nudurupati, N. Aubry, and P. Singh, *Electrohydrodynamics of yeast cells in microchannels subjected to travelling electric fields.* Journal of Physics D: Applied Physics, 2006. **39**(15): p. 3425.

6. M. X. Jiang, et al., *The effects of chemical enucleation combined with whole cell intracytoplasmic injection on panda-rabbit interspecies nuclear transfer.* Zygote, 2004. **12**(4): p. 315-20.

7. U. Zimmermann, et al., *Electromanipulation of mammalian cells: fundamentals and application.* IEEE Transactions on Plasma Science, 2000. **28**(1): p. 72-82.

8. B. Oback and D. N. Wells, *Cloning cattle: the methods in the madness.* Adv Exp Med Biol, 2007. **591**: p. 30-57.

9. B. Oback and D. N. Wells, *Cloning cattle.* Cloning stem cells, 2003. **5**(4): p. 243-56.

10. A. Schurmann, D. N. Wells, and B. Oback, *Early zygotes are suitable recipients for bovine somatic nuclear transfer and result in cloned offspring.* Reproduction, 2006. **132**(6): p. 839-48.

11. P. J. Booth, et al., *Simplification of bovine somatic cell nuclear transfer by application of a zona-free manipulation technique.* Cloning stem cells, 2001. **3**(3): p. 139-50.

12. M. P. Bayona-Bafaluy, G. Manfredi, and C. T. Moraes, *A chemical enucleation method for the transfer of mitochondrial DNA to rho(o) cells.* Nucleic Acids Res, 2003. **31**(16): p. e98.

13. S. L. McElroy and R. A. Reijo Pera, *Noninvasive human nuclear transfer with embryonic stem cells.* CSH Protoc, 2008. **2008**(9): p. pdb prot5040.

14. R. S. Prather, M. M. Sims, and N. L. First, *Nuclear transplantation in early pig embryos.* Biol Reprod, 1989. **41**(3): p. 414-8.

15. P. J. Ross and J. B. Cibelli, *Bovine somatic cell nuclear transfer.* Methods Mol Biol, 2010. **636**: p. 155-77.

16. S. M. Hosseini, et al., *Cloned sheep blastocysts derived from oocytes enucleated manually using a pulled pasteur pipette.* Cell Reprogram, 2013. **15**(1): p. 15-23.

17. L.-H. Chau, et al., *Self-rotation of cells in an irrotational AC E-field in an opto-electrokinetics chip.* PLoS ONE, 2013. **8**(1): p. e51577.

18. M. P. Hughes, *AC electrokinetics: applications for nanotechnology.* Nanotechnology, 2000. **11**(2): p. 124.

19. G. Carmon and M. Feingold, *Rotation of single bacterial cells relative to the optical axis using optical tweezers.* Opt Lett, 2011. **36**(1): p. 40-2.

20. T. Arakawa, et al., *High-throughput single-cell manipulation system for a large number of target cells.* Biomicrofluidics, 2011. **5**(1): p. 14114.

21. P. W. Cooley, D. B. Wallace, and B. V. Antohe. *Applications of ink-jet printing technology to BioMEMS and microfluidic systems*. 2001.

22. H. Lee, et al., *Integrated cell manipulation system-CMOS/microfluidic hybrid.* Lab on a Chip, 2007. **7**(3): p. 331-337.

23. F. Arai, T. Kasugai, and T. Fukuda. *3D position and orientation control method of micro object by dielectrophoresis*. in *proceedings of the International Symposium on Micromechatronics and Human Science, 1998.* . 1998.

24. D. J. Bakewell, Morgan, H., *Dielectrophoresis of DNA: time- and frequency-dependent collections on microelectrodes.* IEEE Transactions on Nanobioscience, 2006. **5**(2): p. 139.

25. A. Castellanos, et al., *Electrohydrodynamics and dielectrophoresis in microsystems: scaling laws.* Journal of Physics D: Applied Physics, 2003. **36**(20): p. 2584.

26. Y. H. Lin, et al., *The application of an optically switched dielectrophoretic (ODEP) force for the manipulation and assembly of cell-encapsulating alginate microbeads in a microfluidic perfusion cell culture system for bottom-up tissue engineering.* Lab Chip, 2012. **12**(6): p. 1164-73.

27. J. Cemazar and T. Kotnik, *Dielectrophoretic field-flow fractionation of electroporated cells.* Electrophoresis, 2012. **33**(18): p. 2867-74.

28. T. Heida, W. L. C. Rutten, and E. Marani, *Understanding dielectrophoretic trapping of neuronal cells: modelling electric field, electrode-liquid interface and fluid flow.* Journal of Physics D: Applied Physics, 2002. **35**(13): p. 1592.

29. M. P. Hughes, R. Pethig, and X.-B. Wang, *Dielectrophoretic forces on particles in travelling electric fields.* Journal of Physics D: Applied Physics, 1996. **29**(2): p. 474.

30. T. P. Hunt and R. M. Westervelt, *Dielectrophoresis tweezers for single cell manipulation.* Biomed Microdevices, 2006. **8**(3): p. 227-30.

31. R. Pethig, *Dielectrophoresis: using inhomogeneous AC electrical fields to separate and manipulate cells.* Critical Reviews in Biotechnology, 1996. **16**(4): p. 331.

32. R. Pethig, et al., *Dielectrophoretic studies of the activation of human T lymphocytes using a newly developed cell profiling system.* Electrophoresis, 2002. **23**(13): p. 2057-63.

33. R. Pethig, et al., *Electrokinetic measurements of membrane capacitance and conductance for pancreatic beta-cells.* IEE proceedings. Nanobiotechnology, 2005. **152**(6): p. 189-193.

34. M. Sancho, et al., *Interaction between cells in dielectrophoresis and electrorotation experiments.* Biomicrofluidics, 2010. **4**(2): p. 022802.

35. M. S. Talary, et al., *Electromanipulation and separation of cells using travelling electric fields.* Journal of Physics D: Applied Physics, 1996. **29**(8): p. 2198.

36. M. K. Kreysing, et al., *The optical cell rotator.* Opt Express, 2008. **16**(21): p. 16984-92.

37. M. B. Rasmussen, L. B. Oddershede, and H. Siegumfeldt, *Optical tweezers cause physiological damage to escherichia coli and Listeria bacteria.* Appl Environ Microbiol, 2008. **74**(8): p. 2441-6.

38. V. N. Binhi, Y. D. Alipov, and I. Y. Belyaev, *Effect of static magnetic field on E. coli cells and individual rotations of ion-protein complexes.* Bioelectromagnetics, 2001. **22**(2): p. 79-86.

39. J. Zlatanova and S. H. Leuba, *Magnetic tweezers: a sensitive tool to study DNA and chromatin at the single-molecule level.* Biochem Cell Biol, 2003. **81**(3): p. 151-9.

40. H. Yun, K. Kim, and W. G. Lee, *Cell manipulation in microfluidics.* Biofabrication, 2013. **5**(2): p. 022001.

41. P. G. P. Benhal, J. G. Chase, B. Oback, W. H. Wang, *Dielectrophoresis-based 3D cell rotation through integration of bottom and vertical electrodes.* Proceedings of MicroTAS-2013 conference, 2013: p. 970-972.

42. K. H. Campbell, et al., *Sheep cloned by nuclear transfer from a cultured cell line.* Nature, 1996. **380**(6569): p. 64-6.

43. R. Jaenisch, et al., *Nuclear cloning, epigenetic reprogramming, and cellular differentiation.* Cold Spring Harb Symp Quant Biol, 2004. **69**: p. 19-27.

44. A. McLaren, *Cloning: pathways to a pluripotent future.* Science, 2000. **288**(5472): p. 1775-1780.

45. R. Jeanisch, et al., *Nuclear cloning, stem cells, and genomic reprogramming.* Cloning Stem Cells, 2002. **4**(4): p. 389-96.

46. A. Jouneau, et al., *Developmental abnormalities of NT mouse embryos appear early after implantation.* Development, 2006. **133**(8): p. 1597-607.

47. W. M. Rideout, 3rd, K. Eggan, and R. Jaenisch, *Nuclear cloning and epigenetic reprogramming of the genome.* Science, 2001. **293**(5532): p. 1093-8.

48. S. T. Sweeney, et al., *Setup for functional cell ablation with lasers: coupling of a laser to a microscope.* Cold Spring Harb Protoc, 2012. **2012**(6): p. 726-32.

49. C.-H. Chuang, Y.-M. Hsu, and C.-C. Yeh, *The effects of nanoparticles uptaken by cells on electrorotation.* Electrophoresis, 2009. **30**(9): p. 1449-1456.

50. M. Ouyang, et al., *Inducing self-rotation of cells with natural and artificial melanin in a linearly polarized alternating current electric field.* Biomicrofluidics, 2013. **7**(5): p. 054112.

51. O. D. Velev, S. Gangwal, and D. N. Petsev, *Particle-localized AC and DC manipulation and electrokinetics.* Annual Reports Section "C" (Physical Chemistry), 2009. **105**(0): p. 213.

52. S. I. Han, Y. D. Joo, and K. H. Han, *An electrorotation technique for measuring the dielectric properties of cells with simultaneous use of negative quadrupolar dielectrophoresis and electrorotation.* Analyst, 2013. **138**(5): p. 1529-37.

53. S. Lucyszyn, *Review of radio frequency microelectromechanical systems technology.* Science, Measurement and Technology, IEE Proceedings -, 2004. **151**(2): p. 93-103.

54. G. M. Dittami, et al., *A multilayer MEMS platform for single-cell electric impedance spectroscopy and electrochemical Analysis.* J Microelectromech Syst, 2008. **17**(4): p. 850-862.

55. I. Giouroudi, J. Kosel, and C. Scheffer, *BioMEMS in Diagnostics: A Review and Recent Developments.* Recent Patents on Engineering, 2008. **2**(2): p. 114-121.

56. D. Stoll, et al., *Protein microarrays: technologies and applications*, in *BioMEMS*, G. Urban, Editor. 2006, Springer US. p. 245-267.

57. C. Lei-Guang, W. Dong-Yi, and M. S. C. Lu. *An integrated micromanipulation and biosensing platform built in glass-based LTPS TFT technology*. in *IEEE Sensors*. 2012.

58. J. Zhu, et al., *Continuous-flow particle and cell separations in a serpentine microchannel via curvature-induced dielectrophoresis.* Microfluidics and Nanofluidics, 2011. **11**(6): p. 743-752.

59. U. M. a. E. Smela, *The design of dielectrophoretic flow-through sorters using a figure of merit.* Journal of Micromechanics and Microengineering, 2008. **18**(1): p. 015001.

60. M. Gianni, *Lab on a chip for live-cell manipulation*, G. Roberto, et al., Editors. 2007. p. 26-36.

61. M. Sawan, M. A. Miled, and E. Ghafar-Zadeh, *CMOS/microfluidic lab-on-chip for cells-based diagnostic tools.* Conf Proc IEEE Eng Med Biol Soc, 2010. **2010**: p. 5334-7.

62. X. Ding, et al., *On-chip manipulation of single microparticles, cells, and organisms using surface acoustic waves.* Proc Natl Acad Sci U S A, 2012. **109**(28): p. 11105-9.

63. H. Ota, et al., *Three-dimensional spheroid-forming lab-on-a-chip using micro-rotational flow.* Sensors and Actuators B: Chemical, 2010. **147**(1): p. 359-365.

64. R. Gambari, et al., *lab-on-a-chip devices for cellular arrays based on dielectrophoresis*, in *Bioarrays*, K. Appasani and E. Southern, Editors. 2007, Humana Press. p. 231-243.

65. L. Paterson, et al., *Controlled rotation of optically trapped microscopic particles.* Science, 2001. **292**(5518): p. 912-914.

66. M. P. MacDonald, et al., *Creation and manipulation of three-dimensional optically trapped structures.* Science, 2002. **296**(5570): p. 1101-1103.

67. J. Gimsa, et al., *Dielectrophoresis and electrorotation of neurospora slime and murine myeloma cells.* Biophysical journal, 1991. **60**(4): p. 749-760.

68. D. Solter, *Mammalian cloning: advances and limitations.* Nat Rev Genet, 2000. **1**(3): p. 199-207.

69. I. Wilmut, et al., *Viable offspring derived from fetal and adult mammalian cells.* Nature, 1997. **385**(6619): p. 810-3.

70. W. S. Hwang, et al., *Patient-specific embryonic stem cells derived from human SCNT blastocysts.* Science, 2005. **308**(5729): p. 1777-1783.

71. J. W. McAvoy and K. E. Dixon, *Nuclear transplantation from specialized and unspecialized gut epithelial cells of adult Xenopus laevis.* Journal of Experimental Zoology, 1974. **189**(2): p. 243-248.

72. M. Pavlin and D. Miklav i, *Effective conductivity of a suspension of permeabilized cells: a theoretical analysis.* Biophysical journal, 2003. **85**(2): p. 719-729.

73. L. L. Sohn, et al., *Capacitance cytometry: measuring biological cells one by one.* Proceedings of the National Academy of Sciences, 2000. **97**(20): p. 10687-10690.

74. I. Ermolina, Y. Polevaya, and Y. Feldman, *Analysis of dielectric spectra of eukaryotic cells by computer modeling.* European Biophysics Journal, 2000. **29**(2): p. 141-145.

75. K. J. Betteridge, *An historical look at embryo transfer.* Journal of Reproduction and Fertility, 1981. **62**(1): p. 1-13.

76. S. Q. Schneider and B. Bowerman, *Cell polarity and the cytoskeleton in the caenorhabditis elegans zygote.* Annu Rev Genet, 2003. **37**: p. 221-49.

77. T. Yasukawa, et al., *Electrophoretic cell manipulation and electrochemical gene-function analysis based on a yeast two-hybrid system in a microfluidic device.* Anal Chem, 2008. **80**(10): p. 3722-7.

78. Z. R. Gagnon, *Cellular dielectrophoresis: applications to the characterization, manipulation, separation and patterning of cells.* Electrophoresis, 2011. **32**(18): p. 2466-87.

79. J. Voldman, *Electrical forces for microscale cell manipulation.* Annu Rev Biomed Eng, 2006. **8**: p. 425-54.

80. R. Pethig, *Review article-dielectrophoresis: status of the theory, technology, and applications.* Biomicrofluidics, 2010. **4**(2): p. 039901.

81. X. Mu, et al., *Microfluidics for manipulating cells.* Small, 2013. **9**(1): p. 9-21.

82. H. C. Zeringue, M. B. Wheeler, and D. J. Beebe, *A microfluidic method for removal of the zona pellucida from mammalian embryos.* Lab on a Chip, 2005. **5**(1): p. 108-110.

83. T. K. T. I. Yoko Yamanishi, T.M. Masaya Hagiwara, Naoki Inomata, and A.F.A. Shogo Kudo, *2DOF magnetically driven microtool for soft peeling of zona pellucida* Journal of Robotics and Mechatronics, 2010. **22**(5): p. 623-630.

84. J. Fulka, Jr., et al., *Somatic and embryonic cell nucleus transfer into intact and enucleated immature mouse oocytes.* Hum Reprod, 2002. **17**(8): p. 2160-4.

85. E. Ibanez, D. F. Albertini, and E. W. Overstrom, *Demecolcine-induced oocyte enucleation for somatic cell cloning: coordination between cell-cycle egress, kinetics of cortical cytoskeletal interactions, and second polar body extrusion.* Biol Reprod, 2003. **68**(4): p. 1249-58.

86. Y. Tsunoda, et al., *Differential sensitivity of mouse pronuclei and zygote cytoplasm to Hoechst staining and ultraviolet irradiation.* J Reprod Fertil, 1988. **82**(1): p. 173-8.

87. J. Bradshaw, et al., *UV irradiation of chromosomal DNA and its effect upon MPF and meiosis in mammalian oocytes.* Mol Reprod Dev, 1995. **41**(4): p. 503-12.

88. L. C. Smith, *Membrane and intracellular effects of ultraviolet irradiation with Hoechst 33342 on bovine secondary oocytes matured in vitro.* J Reprod Fertil, 1993. **99**(1): p. 39-44.

89. G. P. Li, K. L. White, and T. D. Bunch, *Review of enucleation methods and procedures used in animal cloning: state of the art.* Cloning and stem cells, 2004. **6**(1): p. 5-13.

90. N. Z. Saraiva, et al., *Chemically assisted enucleation results in higher G6PD expression in early bovine female embryos obtained by somatic cell nuclear transfer.* Cell Reprogram, 2012. **14**(5): p. 425-35.

91. M. E. Westhusin, et al., *Viable embryos and normal calves after nuclear transfer into Hoechst stained enucleated demi-oocytes of cows.* J Reprod Fertil, 1992. **95**(2): p. 475-80.

92. M. Hagiwara, et al., *Precise control of magnetically driven microtools for enucleation of oocytes in a microfluidic chip.* Advanced Robotics, 2011. **25**(8): p. 991-1005.

93. T. T. Akihiko Ichikawa, Satoshi Akagi, and a. K. Ohba, *Automatic cell cutting by high-precision microfluidic control* Robotics and Mechatronics, 2010. **23**(1): p. 13-18.

94. R. Steinborn, et al., *Mitochondrial DNA heteroplasmy in cloned cattle produced by fetal and adult cell cloning.* Nat Genet, 2000. **25**(3): p. 255-7.

95. T. Tani, et al., *Demecolcine-assisted enucleation for bovine cloning.* Cloning Stem Cells, 2006. **8**(1): p. 61-6.

96. U. Eichenlaub-Ritter, et al., *2-Methoxyestradiol induces spindle aberrations, chromosome congression failure, and nondisjunction in mouse oocytes.* Biology of Reproduction, 2007. **76**(5): p. 784-793.

97. Y. Shen, et al., *Non-invasive method to assess genotoxicity of nocodazole interfering with spindle formation in mammalian oocytes.* Reproductive Toxicology, 2005. **19**(4): p. 459-471.

98. O. D. Velev and K. H. Bhatt, *On-chip micromanipulation and assembly of colloidal particles by electric fields.* Soft Matter, 2006. **2**(9): p. 738-750.

99. M. L. Sin, et al., *Electrothermal fluid manipulation of high-conductivity samples for laboratory automation applications.* JALA Charlottesv Va, 2010. **15**(6): p. 426-432.

100. J. Voldman, *Electrical forces for microscale cell manipulation.* Annual review of biomedical engineering, 2006. **8**: p. 425-454.

101. S. Kuo and M. Sheetz, *Force of single kinesin molecules measured with optical tweezers.* Science, 1993. **260**(5105): p. 232-234.

102. A. Alwan and N. R. Aluru, *Analysis of hybrid electrothermomechanical microactuators with integrated electrothermal and electrostatic actuation.* Microelectromechanical Systems, Journal of, 2009. **18**(5): p. 1126-1136.

103. E. A. Vitol, V. Novosad, and E. A. Rozhkova, *Microfabricated magnetic structures for future medicine: from sensors to cell actuators.* Nanomedicine (Lond), 2012. **7**(10): p. 1611-24.

104. H. A. Pohl, *Some effects of nonuniform fields on dielectrics.* Applied Physics, 1958. **29**(8): p. 1182-1188.

105. H. A. Pohl, *The motion and precipitation of suspensoids in divergent electric fields.* Applied Physics, 1951. **22**(7): p. 869-871.

106. R. Pethig, *Review article-dielectrophoresis: status of the theory, technology, and applications.* Biomicrofluidics, 2010. **4**(2): p. 022811.

107. D. R. Anas Alazzam, Vahé Nerguizian, Ion Stiharu, Rama Bhat, *Analytical formulation of electric field and dielectrophoretic force for moving dielectrophoresis using Fourier series.* Microfluidics and Nanofluidics, 2010.

108. C. Y. Yang, *Quasistatic force and torque on ellipsoidal particles under generalized dielectrophoresis.* Journal of Applied Physics, 2007. **102**(9): p. 094702.

109. X. Wang, et al., *A theoretical method of electrical field analysis for dielectrophoretic electrode arrays using Green's theorem.* Journal of Physics D: Applied Physics, 1996. **29**(6): p. 1649.

110. R. Renaudot, et al., *Optimization of liquid Dielectrophoresis (LDEP) digital microfluidic transduction for biomedical applications.* Micromachines, 2011. **2**(2): p. 258-273.

111. K. V. Kaler, R. Prakash, and D. Chugh, *Liquid dielectrophoresis and surface microfluidics.* Biomicrofluidics, 2010. **4**(2): p. 022805.

112. Y. Demircan, E. Özgür, and H. Külah, *Dielectrophoresis: applications and future outlook in point of care.* Electrophoresis, 2013. **34**(7): p. 1008-1027.

113. H. M. Tao Sun, and Nicolas G. Green, *Analytical solutions of ac electrokinetics in interdigitated electrode arrays: Electric field, dielectrophoretic and traveling-wave dielectrophoretic forces.* Physical Review E, 2007. **76**(4): p. 046610.

114. P. T. W. A. Germishuizen, A. P. J. Middelberg, C. Walti, A.G. Davies, R. Wirtz, M. Pepper, *Influence of alternating current electrokinetic forces and torque on the elongation of immobilized DNA.* Journal of Applied Physics, 2005. **97**(1): p. 014702.

115. N. G. Green, A. Ramos, and H. Morgan, *Ac electrokinetics: a survey of sub-micrometre particle dynamics.* Journal of Physics D: Applied Physics, 2000. **33**(6): p. 632.

116. T. Muller, et al., *The potential of dielectrophoresis for single-cell experiments.* IEEE Eng Med Biol Mag, 2003. **22**(6): p. 51-61.

117. S. W. Lee, Bashir, R., *Dielectrophoresis and electrohydrodynamics-mediated fluidic assembly of silicon resistors.* Applied Physics Letters, 2003. **83**(18): p. 3833.

118. C. K. M. Fung, *Dielectrophoretic batch fabrication of bundled carbon nanotube thermal sensors.* IEEE Transactions On Nanotechnology, 2004. **3**(3): p. 395.

119. J. Korlach, et al., *Trapping, deformation, and rotation of giant unilamellar vesicles in octode dielectrophoretic field cages.* Biophys J, 2005. **89**(1): p. 554-62.

120. R. Holzel, et al., *Trapping single molecules by dielectrophoresis.* Phys Rev Lett, 2005. **95**(12): p. 128102.

121. N. A. Mortensen, et al., *Electrohydrodynamics of binary electrolytes driven by modulated surface potentials.* Phys Rev E Stat Nonlin Soft Matter Phys, 2005. **71**(5 Pt 2): p. 056306.

122. C. D. M. M. R. Bown, *AC electroosmotic flow in a DNA concentrator.* Microfluidics and Nanofluidics, 2006.

123. D. V. Le, et al., *Numerical design of electrical-mechanical traps.* Lab Chip, 2008. **8**(5): p. 755-63.

124. M. R. Willis, *Dielectric and electronic properties of biological materials.* Biochemical Education, 1980. **8**(1): p. 31.

125. J. Gimsa and D. Wachner, *A polarization model overcoming the geometric restrictions of the laplace solution for spheroidal cells: obtaining new equations for field-induced forces and transmembrane potential.* Biophys J, 1999. **77**(3): p. 1316-26.

126. Y. J. Lo and U. Lei, *Quasistatic force and torque on a spherical particle under generalized dielectrophoresis in the vicinity of walls.* Applied Physics Letters, 2009. **95**(25): p. 253701.

127. C. Y. Yang and U. Lei, *Dielectrophoretic force and torque on a sphere in an arbitrary time varying electric field.* Applied Physics Letters, 2006. **89**(16): p. 163902.

128. S. H. Ling, Y. C. Lam, and K. S. Chian, *Continuous cell separation using dielectrophoresis through asymmetric and periodic microelectrode array.* Analytical Chemistry, 2012. **84**(15): p. 6463-6470.

129. B. Yafouz, N. Kadri, and F. Ibrahim, *Microarray dot electrodes utilizing dielectrophoresis for cell characterization.* Sensors, 2013. **13**(7): p. 9029-9046.

130. R. Pethig, et al., *Positive and negative dielectrophoretic collection of colloidal particles using interdigitated castellated microelectrodes.* Journal of Physics D: Applied Physics, 1992. **25**(5): p. 881.

131. M. Washizu and T. B. Jones, *Generalized multipolar dielectrophoretic force and electrorotational torque calculation.* Journal of Electrostatics, 1996. **38**(3): p. 199-211.

132. M. Lombardini, et al., *Horizontal nDEP cages within open microwell arrays for precise positioning of cells and particles.* Lab Chip, 2010. **10**(9): p. 1204-7.

133. K. D. Wulff, D. G. Cole, and R. L. Clark, *Controlled rotation of birefringent particles in an optical trap.* Applied Optics, 2008. **47**(34): p. 6428-6433.

134. M. C. Zhong, et al., *Trapping red blood cells in living animals using optical tweezers.* Nat Commun, 2013. **4**: p. 1768.

135. S. K. Mohanty, K. S. Mohanty, and M. W. Berns, *Manipulation of mammalian cells using a single-fiber optical microbeam.* J Biomed Opt, 2008. **13**(5): p. 054049.

136. D. G. Grier, *A revolution in optical manipulation.* Nat Photon, 2003. **424**(6950): p. 810-816.

137. Y. L. Liang, et al., *Cell rotation using optoelectronic tweezers.* Biomicrofluidics, 2010. **4**(4): p. 43003.

138. J. Cheng, et al., *Preparation and hybridization analysis of DNA/RNA from E. coli on microfabricated bioelectronic chips.* Nat Biotech, 1998. **16**(6): p. 541-546.

139. H. Morgan, M. P. Hughes, and N. G. Green, *Separation of submicron bioparticles by dielectrophoresis.* Biophysical Journal, 1999. **77**(1): p. 516-525.

140. N. G. Green, H. Morgan, and J. J. Milner, *Manipulation and trapping of sub-micron bioparticles using dielectrophoresis.* Journal of Biochemical and Biophysical Methods, 1997. **35**(2): p. 89-102.

141. A. Menachery, et al., *Counterflow dielectrophoresis for trypanosome enrichment and detection in blood.* Sci Rep, 2012. **2**: p. 775.

142. P. R. Roy, M. R. Tomkins, and A. Docoslis, *Enhancing the performance of surface-based biosensors by AC electrokinetic effects*. Biosensors - Emerging Materials and Applications. 2011.

143. K. C. Cheung and P. Renaud, *BioMEMS for medicine: On-chip cell characterization and implantable microelectrodes.* Solid-State Electronics, 2006. **50**(4): p. 551-557.

144. K. Morishima, et al. *Noncontact transportation of DNA molecule by dielectrophoretic force for micro DNA flow system*. in *Robotics and Automation*. 1996.

145. T. Müller, et al., *A 3-D microelectrode system for handling and caging single cells and particles.* Biosensors and Bioelectronics, 1999. **14**(3): p. 247-256.

146. H. Maier, *Electrorotation of colloidal particles and cells depends on surface charge.* Biophysical Journal, 1997. **73**(3): p. 1617-1626.

147. C. Dalton, et al., *Analysis of parasites by electrorotation.* Journal of Applied Microbiology, 2004. **96**(1): p. 24-32.

148. R. Paul and M. Otwinowski, *The theory of the frequency response of ellipsoidal biological cells in rotating electrical fields.* J Theor Biol, 1991. **148**(4): p. 495-519.

149. W. M. Arnold, et al., *Electro-rotation of mouse oocytes: single-cell measurements of zona-intact and zona-free cells and of the isolated zona pellucida.* Biochim Biophys Acta, 1987. **905**(2): p. 454-64.

150. W. M. Arnold and U. Zimmermann, *Electro-rotation: development of a technique for dielectric measurements on individual cells and particles.* Journal of Electrostatics, 1988. **21**(2-3): p. 151-191.

151. W. M. Arnold, et al., *Electro-rotation of mouse oocytes: single-cell measurements of zona-intact and zona-free cells and of the isolated zona pellucida.* Biochimica et Biophysica Acta (BBA) - Biomembranes, 1987. **905**(2): p. 454-464.

152. I. Turcu and C. M. Lucaciu, *Electrorotation: a spherical shell model.* Journal of Physics A: Mathematical and General, 1989. **22**(8): p. 995.

153. M. Zrinyi, M. Nakano, and T. Tsujita, *Electrorotation of novel electroactive polymer composites in uniform DC and AC electric fields.* Smart Materials and Structures, 2012. **21**(6): p. 065022.

154. D. Mietchen, et al., *Automated dielectric single cell spectroscopy - temperature dependence of electrorotation.* Journal of Physics D: Applied Physics, 2002. **35**(11): p. 1258.

155. D. Wicher and J. Gündel, *Electrorotation of multi- and oligolamellar liposomes.* Bioelectrochemistry and Bioenergetics, 1989. **21**(3): p. 279-288.

156. C. Dalton, A. D. Goater, and H. V. Smith, *Fertilization state of Ascaris suum determined by electrorotation.* J Helminthol, 2006. **80**(1): p. 25-31.

157. H. Y. Wang XB, Gascoyne PR, Becker FF, Hölzel R, Pethig R., *Changes in Friend murine erythroleukaemia cell membranes during induced differentiation determined by electrorotation.* Biochim Biophys Acta., 1994. **1193**(2): p. 330-44.

158. C. Reichle, et al., *A new microsystem for automated electrorotation measurements using laser tweezers.* Biochimica et biophysica acta, 2000. **1459**(1): p. 218-229.

159. J. Gimsa, *A comprehensive approach to electro-orientation, electrodeformation, dielectrophoresis, and electrorotation of ellipsoidal particles and biological cells.* Bioelectrochemistry, 2001. **54**(1): p. 23-31.

160. M. H. a. J. G. Kanokkan Maswiwat, *Optimizing the electrode shape for four-electrode electrorotation chips.* ScienceAsia 2006. **33**(2007): p. 061-067.

161. U. Lei, P. H. Sun, and R. Pethig, *Refinement of the theory for extracting cell dielectric properties from dielectrophoresis and electrorotation experiments.* Biomicrofluidics, 2011. **5**(4): p. 44109-4410916.

162. A. A. R. Shirsavar, M. R. Ejtehadi, M. R. Mozaffari, M. S. Feiz, *Rotational regimes of freely suspended liquid crystal films under electric current in presence of an external electric field.* Microfluidics and Nanofluidics, 2012. **13**(1): p. 83-89.

163. Y. H. J Yang, X Wang, X B Wang, F F Becker, and P R Gascoyne, *Dielectric properties of human leukocyte subpopulations determined by electrorotation as a cell separation criterion.* Biophysical Journal, 1999. **76**(6): p. 3307.

164. S. Comlekci, *Electrostatic field considerations related force effect on electrospinning.* Journal of Electrostatics, 2012. **70**(1): p. 149-151.

165. K. Kolikov, et al., *Electrostatic interaction between two conducting spheres.* Journal of Electrostatics, 2012. **70**(1): p. 91-96.

166. D. Seyfried, D. Menschikow, and J. Schoebel, *Free space permittivity determination technique.* Microwave and Optical Technology Letters, 2013. **55**(12): p. 2888-2892.

167. S. O. Nelson, *Fundamentals of dielectric properties measurements and agricultural applications.* J Microw Power Electromagn Energy, 2010. **44**(2): p. 98-113.

168. D. T. Lopes and C. C. Motta, *Electrostatic force between rings and discs of charge inside a grounded metallic pipe using the Green's function technique.* Journal of Electrostatics, 2012. **70**(1): p. 166-173.

169. S. L. Meredith, S. K. Earles, and C. E. Otero, *Electric fields induced by a modified double exponential current waveform.* Journal of Electrostatics, 2012. **70**(1): p. 152-156.

170. X.-B. Wang, et al., *A unified theory of dielectrophoresis and travelling wave dielectrophoresis.* Journal of Physics D: Applied Physics, 1994. **27**(7): p. 1571.

171. S. P. Kadaksham AT, Aubry N., *Dielectrophoresis of nanoparticles.* Electrophoresis, 2004. **25**(21-22): p. 3625.

172. X. B. Wang, et al., *Theoretical and experimental investigations of the interdependence of the dielectric, dielectrophoretic and electrorotational behaviour of colloidal particles.* Journal of Physics D: Applied Physics, 1993. **26**(2): p. 312.

173. X. Wang, R. Pethig, and T. B. Jones, *Relationship of dielectrophoretic and electrorotational behaviour exhibited by polarized particles.* Journal of Physics D: Applied Physics, 1992. **25**(6): p. 905.

174. S. Couderc, V. Blech, and B. Kim, *New surface treatment and microscale/nanoscale surface patterning using electrostatically clamped stencil mask.* Japanese Journal of Applied Physics, 2009. **48**(9R): p. 095007.

175. C. W. Park, O. V. Mena, and J. Brugger, *Patterning of parallel nanobridge structures by reverse nanostencil lithography using an edge-patterned stencil.* Nanotechnology, 2007. **18**(4): p. 044002.

176. R. P. Rocha, et al., *Microlenses array made with AZ4562 photoresist for stereoscopic acquisition.* Procedia Engineering, 2012. **47**(0): p. 619-622.

177. X. Q. Bao, T. Dargent, and E. Cattan, *Micromachining SU-8 pivot structures using AZ photoresist as direct sacrificial layers for a large wing displacement.* Journal of Micromechanics and Microengineering, 2010. **20**(2): p. 025005.

178. J. Olesik, *ITO coating by reactive magnetron sputtering-comparison of properties from DC and MF processing.* Thin Solid Films, 1999. **351**(1-2): p. 48.

179. J. Olesik, *Transparent and conducting ITO films: new developments and applications.* Thin Solid Films, 2002. **411**(1): p. 1.

180. K. A. DeBruin and W. Krassowska, *Modeling electroporation in a single cell. I. effects of field strength and rest potential.* Biophysical Journal, 1999. **77**(3): p. 1213-1224.

181. T. B. Jones, *Electromechanics of particles.* Cambridge , New York, Cambridge University Press, 1942-1995.

182. T. B. Jones, *Basic theory of dielectrophoresis and electrorotation.* IEEE Eng Med Biol Mag, 2003. **22**(6): p. 33-42.

183. A. Zehe, A. Ramírez, and O. Starostenko, *Mathematical modeling of electro-rotation spectra of small particles in liquid solutions: Application to human erythrocyte aggregates.* Brazilian Journal of Medical and Biological Research, 2004. **37**: p. 173-183.

184. J. Wang, et al., *Electrorotational spectra of protoplasts generated from the giant marine algaValonia utricularis.* Protoplasma, 1997. **196**(3-4): p. 123-134.

185. S. Park, et al., *Continuous dielectrophoretic bacterial separation and concentration from physiological media of high conductivity.* Lab Chip, 2011. **11**(17): p. 2893-900.

186. P. Gaynor, D. N. Wells, and B. Oback, *Couplet alignment and improved electrofusion by dielectrophoresis for a zona-free high-throughput cloned embryo production system.* Med Biol Eng Comput, 2005. **43**(1): p. 150-4.

187. G. D. Gasperis, et al., *Automated electrorotation: dielectric characterization of living cells by real-time motion estimation.* Measurement Science and Technology, 1998. **9**(3): p. 518.

188. *Quantitative measurements of absolute dielectrophoretic forces using optical tweezers.* Optics Letters, 2010. **35**(14): p. 2493.

189. G. G. Fuhr, Glaser, R. , *Electrorotation: A new method of dielectric spectroscopy.* Stud. Biophys., 1988. **127**: p. 11-18.

190. G. Fuhr and P. I. Kuzmin, *Behavior of cells in rotating electric fields with account to surface charges and cell structures.* Biophysical journal, 1986. **50**(5): p. 789-795.

191. G. Fuhr and R. Hagedorn, *Cell electrorotation*, in *Electrical Manipulation of Cells*, P. Lynch and M. Davey, Editors. 1996, Springer US. p. 37-70.

192. K. Asami and A. Irimajiri, *Dielectric analysis of mitochondria isolated from rat liver. II. Intact mitochondria as simulated by a double-shell model.* Biochim Biophys Acta, 1984. **778**(3): p. 570-8.

193. G. Fuhr, et al., *Differences in the rotation spectra of mouse oocytes and zygotes.* Biochim Biophys Acta, 1987. **930**(1): p. 65-71.

194. I. Y. Bar-Itzhack, *New method for extracting the quaternion from a rotation matrix.* Journal of Guidance, Control, and Dynamics, 2000. **23**(6): p. 1085-1087.

195. K. McFarlane, N. C. McGill, and I. H. McKenna, *Space-time and spatial geodesies on a rotating sphere.* International Journal of Theoretical Physics, 1980. **19**(5): p. 347-368.

196. U. Zimmermann and P. Scheurich, *High frequency fusion of plant protoplasts by electric fields.* Planta, 1981. **151**(1): p. 26-32.

197. T. Y. Tsong, *Electroporation of cell membranes.* Biophys J, 1991. **60**(2): p. 297-306.

198. M. Wiklund, *Acoustofluidics 12: Biocompatibility and cell viability in microfluidic acoustic resonators.* Lab Chip, 2012. **12**(11): p. 2018-2028.

199. S. Sridharan, et al., *Joule heating effects on electroosmotic flow in insulator-based dielectrophoresis.* Electrophoresis, 2011. **32**(17): p. 2274-2281.